UC Santa Cruz
UC Santa Cruz Electronic Theses and Dissertations

Title
Design, Simulation, Fabrication, and Characterization of MEMS-based, Tunable FABRY-PEROT Interferometer Filter in the Long Wavelength Infrared Region

Permalink
https://escholarship.org/uc/item/4sp195s1

Author
Kim, Tae Sung

Publication Date
2019

Peer reviewed|Thesis/dissertation

eScholarship.org Powered by the California Digital Library
University of California

UNIVERSITY OF CALIFORNIA
SANTA CRUZ

DESIGN, SIMULATION, FABRICATION, AND CHARACTERIZATION OF MEMS-BASED, TUNABLE FABRY-PEROT INTERFEROMETER FILTER IN THE LONG WAVELENGTH INFRARED REGION

A dissertation submitted in partial
satisfaction of the requirements for the
degree of

DOCTOR OF PHILOSOPHY

in

ELECTRICAL ENGINEERING

by

Tae Sung Kim

December 2019

The Dissertation of Tae Sung Kim is approved:

Professor Marco Rolandi, chair

Professor Holger Schmidt

Professor Bruce Schumm

Quentin Williams
Acting Vice Provost and Dean of Graduate Studies

Table of Contents

List of Figures vi

List of Tables ix

ABSTRACT x

Chapter 1. Introduction 1

Chapter 2. Theoretical Background for the Design of the FPI Filter 9

  2.1 Fabry-Perot interferometer 9

  2.2 The Distributed Bragg Reflector 18

  2.3 An electrostatic actuator 32

  Mathematical Derivation I: Derivation of $h = 2n1dcos\theta iII2$ 39

  Mathematical Derivation II: Derivation of the characteristic matrix for TM wave 41

Chapter 3. Implementation of the FPI Filter 44

  3.1 The Design of the FPI Structure 45

  3.2 The Design of the DBR mirror 52

Chapter 4. The Simulation of the FPI Filter 61

  4.1 The Reflectance of the DBR Mirror 61

  4.2 Electrostatic Actuation of the FPI with an X-beam Structure 68

    4.2.1 The Analytic Solution of the FPI Actuation 69

    4.2.2 The Numerical Solution of the FPI Actuation 73

4.3 The filtering performance of the FPI in λ = 8-11 μm 79

Chapter 5. The Fabrication of the FPI Filter... 84

5.1. The Fabrication Equipment in the SNF.. 84

5.1.1 The Optical Photolithography Tools 84

5.1.2 The Deposition Tools 92

5.1.3 The Etch Tools.. 96

5.2. The Fabrication of top and bottom membranes 99

5.2.1. The fabrication of the top membrane 101

5.2.2. The fabrication of the bottom membrane 108

5.3. The Deposition of the DBR mirror 113

5.4. The assembly of the FPI.. 115

Chapter 6. Characterization of the FPI Filter.. 119

6.1 Measurement Equipment used for the Characterization 119

6.1.1 The Optical Profilometer.. 120

6.1.2 The FTIR Spectrometer 124

6.2 The Characterization of the DBR.. 129

6.3 The Characterization of the FPI filter 131

6.3.1 The characterization of the Electrostatic Actuation of the FPI filter........ 132

6.3.2 The characterization of the Transmittance Spectrum of the FPI filter 135

6.3.3 The characterization of the tunable filtering of the FPI filter 137

Chapter 7. Discussion and Conclusion 140

7.1 Discussion 140

7.2 Conclusion.. 143

Bibliography 145

LIST OF FIGURES

Fig. 1.1 The Transmission Spectrum of Ethanol …………………………………. 3

Fig. 2.1 Airy summation ………………………………………………………... 12

Fig. 2.2 Fields at the boundaries of three different media ………………………… 21

Fig. 2.3 The Distributed Bragg Reflector ………………………………………. 26

Fig. 2.4 The Spectral Response of the DBR ……………………………………. 28

Fig. 2.5 Parallel Plates Actuator ……………………………………………... 33

Fig. 2.6 The Graphical Solution of $F_m = F_e$ ……………………………………….. 36

Fig. 2.7 A Parallel Plate Actuator with X-beam Structure ……………………….. 37

Fig. M1 An optical path difference between two lights …………………………… 40

Fig. 3.1 A simplified FPI Structure ……………………………………………….. 49

Fig. 3.2 The Lithography Masks for the FPI Filter ………………………………... 50

Fig. 3.3 The Index of Refraction for Ge and ZnS …………………………………. 57

Fig. 4.1 The Reflectance of the Ge/ZnS DBR on air substrate ……………………. 64

Fig. 4.2 The Reflectance of the Ge/ZnS DBR on Si substrate …………………….. 65

Fig. 4.3 The Reflectance of the Ge/ZnS DBR on 25 um Si membrane …………... 66

Fig. 4.4 The Reflectance of the 5 stacks Ge/ZnS DBR on 25 um Si membrane with different AR coating ……………………………………………………………….. 67

Fig. 4.5 The graph of Deflection vs. Applied Bias Voltage ………………………. 71

Fig. 4.6 The graphical Solution of $F_k = F_e$ ……………………………………… 73

Fig. 4.7 The Layout of the X-beam Structure ……………………………………... 74

Fig. 4.8 The 3-dimensional Model of the X-beam Structure ……………………… 76

Fig. 4.9 The Graphical Solution of the FPI Electrostatic Actuation ……………… 78

Fig. 4.10 The Electrostatic Actuation of the FPI ………………………………….. 79

Fig. 4.11 The Transmission Spectrum of the FPI Filter with Constant DBR Reflectance R of 0.95 ……………………………………………………………………….. 81

Fig. 4.12 The Transmission Spectrum of the FPI Filter with Wavelength Dependent DBR Reflectance R ……………………………………………………………… 82

Fig. 5.1 The SVGCOAT tracks …………………………………………………….. 86

Fig. 5.2 The Karlsuss System ……………………………………………………... 88

Fig. 5.3 The SVGDEV and SVGDEV2 ……………………………………………. 89

Fig. 5.4 The CCP-Dep ……………………………………………………………... 94

Fig. 5.5 The INNOTEC ……………………………………………………………. 96

Fig. 5.6 The AMTETCHER ………………………………………………………... 97

Fig. 5.7 The STSETCH …………………………………………………………….. 98

Fig. 5.8 The front side of top membrane wafer ……………………………………102

Fig. 5.9 The back side of top membrane wafer …………………………………… 104

Fig. 5.10 Top Membrane with the X-beam structure after the Fabrication ………. 105

Fig. 5.11 The Fabrication Process Flow of the Top Membrane ………………….. 106

Fig. 5.12 The front side of bottom membrane wafer ……………………………... 108

Fig. 5.13 The back side of bottom membrane wafer ……………………………... 110

Fig. 5.14 The Fabrication Process Flow of the Bottom Membrane ………………. 111

Fig. 5.15 SEM Pictures of 5 Stack DBR ………………………………………….. 114

Fig. 5.16 Top and Bottom Membranes assembled with a UV glue ………………. 116

Fig. 5.17 Pictures of finished Top and Bottom Membranes ……………………… 117

Fig. 5.18 A picture of completed FIP filter ……………………………………….. 117

Fig. 6.1 Operational principle of an Optical Profiler ……………………………... 121

Fig. 6.2 Veeco WYKO NT1100 …………………………………………………….. 122

Fig. 6.3 The Michelson-Morley Inteferometer …………………………………… 124

Fig. 6.4 The inteferogram with different OPD's ………………………………….. 125

Fig. 6.5 Typical interferogram ……………………………………………………. 126

Fig. 6.6 Nicolet iS50 FTIR Spectrometer ………………………………………… 128

Fig. 6.7 The reflectance of the DBR mirrors ……………………………………... 130

Fig. 6.8 The Gap Distance Measurement …………………………………………. 132

Fig. 6.9 The graph of measured electrostatic actuation of the FPI ……………….. 134

Fig. 6.10 The Transmittance of the FPI Filter for λ = 6-13 μm …………………... 135

Fig. 6.11 Simulated Transmittance of the FPI Filter for λ = 6.5-12.5 μm ………... 136

Fig. 6.12 The Transmittance Spectrum of the FPI in λ = 7-12 μm ……………….. 138

Fig. 7.1 The Plate Defects ………………………………………………………… 141

LIST OF TABLES

Table 4.1 The Simulated FWHM of the FPI ..……………………………………… 83

Table 5.1 The description of the SOI wafer used in fabrication ………………….. 100

Table 6.1 Electrostatic Actuation of the FPI ……………………………………... 133

Table 6.2 The expected and measured passing wavelength of the FPI …………... 137

ABSTRACT

DESIGN, SIMULATION, FABRICATION, AND CHARACTERIZATION OF MEMS-BASED, TUNABLE FABRY-PEROT INTERFEROMETER FILTER IN THE LONG WAVELENGTH INFRARED REGION

Tae Sung Kim

Demand for a small, portable IR spectrometer has been growing steadily for many years. A monochromator is one of the essential parts that comprises any spectroscopy system. A MEMS-based, tunable Fabry-Perot interferometer filter (FPI), that is proposed to be a monochromator with a broadband IR detector array in an improvised explosive device detection system, is designed, simulated, fabricated and characterized in this dissertation. With the operational wavelength range in the long wavelength IR region, from 8 to 11 μm, a distributed Bragg reflector with germanium and zinc sulfide is used to implement the mirror that covers the target spectrum. One of the mirrors is fabricated with four beam springs in an X-shape to tune the passing wavelength of the FPI filter by adjusting the gap distance between two membranes using electrostatic attraction.

Designed device is simulated to confirm it meeting the required device specification. Taking advantage of SOI wafer, the FPI filter is fabricated with simple fabrication process with only four lithography masks, one deposition, and three etch steps. The scaffold structure is fabricated with both surface micromachining and bulk micromachining process. The DBR mirror is deposited using EBPVD on two membranes, and then assembled into the FPI filter. The fabrication process is

performed at the Stanford Nanofabrication Facility (SNF). Fabricated device is characterized at the UCSC and the SNF. Completed FPI filter showed the necessary filtering and tuning behavior with 30% transmittance peak and 2 μm FWHM. With expected performance of 100% peak and 0.15 μm FWHM, however, a need for significant performance improvement is observed. The cause of transmission peak degradation is attributed to the loss due to reflection and absorption of Si membrane and of passband broadening to the plate defeats of the DBR. The direction of study for further process improvement is suggested.

CHAPTER 1. INTRODUCTION

In the broadest sense, any study of matter through its interaction with an electromagnetic (EM) wave can be described as spectroscopy. Quantum mechanics taught us that the energy of atoms and molecules inside matter is limited to certain discrete values, or quantized. When EM wave interacts with matter; that is, when matter absorbs or emits light, it changes its internal energy state. Moreover, the difference of energy before and after the change must be the same as the amount of energy the EM wave that is absorbed or emitted. Based on this principle, spectroscopy probes the internal energy structure of matter under study.

Since the dawn of era of quantum mechanics, spectroscopy has been one of the most effective research tools available for scientists and engineers. Wide range of energy is involved in various atomic and molecular transition inside the matter. The energy of EM wave is inversely proportional to the wavelength of the EM wave. Therefore, the energy scale from different interaction dictates what region of EM spectrum is used in certain spectroscopic studies. For example, nuclear spin interaction is studied with low energy and long wavelength radio frequency EM wave (wavelength $\lambda = \sim 10^2$ cm) and for core level electron transition in atoms, spectroscopy is done using high energy and short wavelength X-ray ($\lambda = \sim 10^{-7}$ cm) as a probe. In the middle of these two extremes, infrared (IR) region of the EM spectrum is of particular interests to spectroscopy researchers. Many organic and inorganic materials can be excited by the light with the energy in the IR region. With

the IR spectroscopy, they can identify the type of atoms within the molecule, the type of bonds between atoms, and even the molecular structure itself.

The IR covers very broad spectral region from 700 nm to 1 mm. There are two different schemes in use to divide the entire IR region into subregions. First scheme, ISO 20473, is based on the location of the IR spectrum with respect to the visible (VIS) region of the EM spectrum. The IR spectrum is grouped into three sub-regions: the near-infrared (NIR) region with the wavelength from 0.78 to 3 μm, the mid-infrared (MIR) region from 3 to 50 μm, and the far-infrared (FIR) region from 50 to 1000 μm. The same designation with the slightly different boundaries of sub-regions are used in the astronomy community (NIR: 0.7 – 5 μm, MIR: 5 – 25~40 μm, FIR: 25~40 – 200~350 μm). We use the other common division scheme for the IR spectrum with five sub-regions in this dissertation. In this scheme, NIR covers from 0.75 to 1.4 μm, short-wavelength infrared (SWIR) from 1.4 to 3 μm, mid-wavelength infrared (MWIR) from 3 to 8 μm, long-wavelength infrared (LWIR) from 8 to 15 μm, and FIR from 15 to 1000 μm.

A typical IR spectrum is given in figure 1.1. It is a graph of the sample transmittance given in percentage. Since the transmittance is presented, the peak in the IR spectrum is inverted; more absorption in the sample, deeper the absorption peak. Horizontal axis of the IR spectrum is the wavelength of the spectrum. Most IR spectra covers the wavelength from 2.5 to 25 μm. Instead of wavelength, however, a wavenumber in unit of cm^{-1} is used for the x-axis. It covers the wavenumber from 4000 to 400 cm^{-1} in decreasing order. The IR absorption in this region causes the

excitation of the vibrations of covalent bonds within the molecule. These vibrations include the stretching and bending modes of various atomic interconnections. The IR spectrum is split to two regions; the functional group region from 4000 to 1000 cm^{-1} and the fingerprint region below 1000 cm^{-1}. Many chemical functional groups have an absorption peak at specific wavenumber with a known intensity and width in the functional group region. For example, alkanes group has strong peak in 2850 – 3000 cm^{-1} and alkenes group in 1900 – 1000 cm^{-1}. The complexity of spectrum in the fingerprint region makes it hard to assign all the peaks. However, many materials have unique spectral patterns there. Collection of such data is measured and tabulated for reference and incorporated into a software system for researchers.

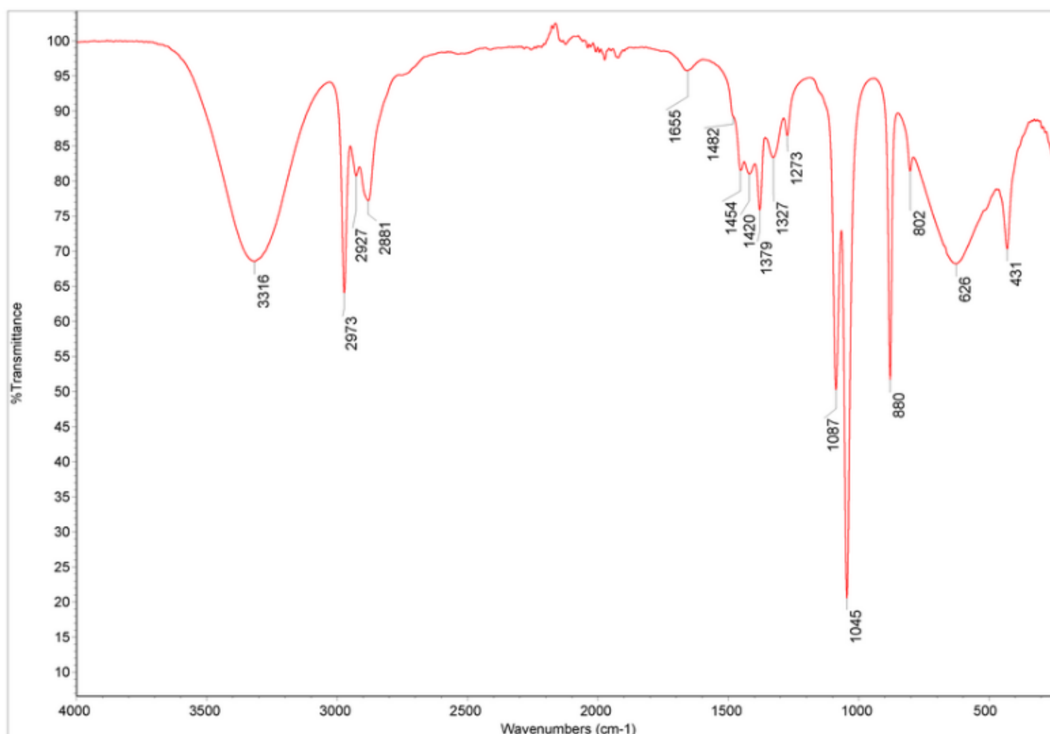

Fig. 1.1 The Transmission Spectrum of Ethanol. The horizontal axis is the wavenumber, and the vertical axis the transmittance. The locations of absorption peaks are annotated.

Two distinct classes of spectrometer are in use. Most spectrometers including an IR spectrometer comprise an IR light source, a monochromator, and a detector. A white (of all wavelengths) IR light from the light source is shone on the sample. As the white IR light is transmitted through the sample, some IR wavelengths are absorbed and some pass through. The transmitted IR waves are measured by the detector as an IR spectrum of the sample. The monochromator separates two classes of spectrometer. Dispersive IR spectrometer uses a dispersive medium, usually a prism or a diffraction grating to disperse the IR spectrum into its individual wavelength components. The second class is called an interferometer type. It uses a Michelson-Morley interferometer, where a single light is split into two beams by beam splitter. They travel along the different beam paths, individually reflected by the mirror, combined again to interfere with each other. By adjusting the length of one beam path, an interferometer can work as a monochromator. More are said in later chapters because first, our device is based on the principle of interferometer and also one of the measurement equipment used in the characterization is an IR spectrometer based on interferometry.

Regardless of its operational mechanism, conventional IR spectrometer is complex and expensive instrument, and only large research institute or industry organization can afford it. On the other hand, strong demand for a robust and transportable IR spectrometer is generated from a diverse field of applications. It includes diagnostics products for medical and health care communities, process monitoring device for pharmaceutical industry, hazardous material detection in the

chemical and petroleum industries, and more. Micro-electro-mechanical system (MEMS) provides a promising technological possibility for such a portable IR spectrometer. MEMS technology uses a semiconductor microfabrication process to produce a micro-sized electro-mechanical device. Commercially successful MEMS devices include now obsolete ink-jet printer nozzle, optical communication relay switch, automobile tire pressure gauge, gyroscope and accelerometer inside the smartphone. Two fabrication approaches are developed in the MEMS technology; surface micromachining and bulk micromachining. In surface micromachining, layers of different materials are deposited and etched to build the desired microstructure on the wafer surface. Some of the deposited layers are sacrificial; that is, they are etched away to produce a structural space between the layers above and below itself. Bulk micromachining, on the other hand, uses the wafer itself to build the structure. For example, a trench on a microfluidic device can be fabricated by pattering it on the wafer and etching into the wafer. More time than not, however, these two approaches are used in tandem to fabricate a MEMS device.

In this comprehensive review, Crocombe [10-13] described different approaches to produce a small and portable IR spectrometer, including many dispersive and interferometer-based designs using wide range of fabrication technology. It is noted there that in MEMS technology, a Fabry-Perot interferometer (FPI) with its simple structure is most scalable and easy to adapt monochromator structure for a small, portable IR spectrometer. An FPI consists of two partially transmitting mirrors facing each other in parallel. The distance between the mirrors

determines the wavelength that passes through the FPI. Detailed theoretical description of the FPI is followed in the next chapter. Many groups around the world have been working on developing FPI-based IR spectrometer using MEMS technology. Among them, three groups have been producing most noticeable results. All three groups use one of two different fabrication approaches to realize an IR spectrometer with MEMS technology.

Microelectronics research group at the University of Western Australia has been developing an FPI-based IR spectrometer for many years [2, 3, 15, 29, 30]. Using the surface micromachining technology, their design monolithically integrates a monochromator into the IR sensor array. They successfully demonstrated their device in NIR and MIR region, and currently developing a device capable of working in the LWIR range. The VTT Technical Research Center of Finland is another research group elected to implement the surface micromachining for their IR spectrometer fabrication [1, 7, 24, 25, 35-40]. Their first commercialized IR spectrometer was a CO_2 gas sensor with spectral range of 3.9 – 4.6 μm (CO_2 absorption peak is at 4.26 μm). Both cases, the fabrication process is rather complicated due to the inherent process complexity of the surface micromachining technology. Infra Tec GmbH in Germany, in conjunction with Technical University in Chemnitz and Fraunhofer Institute for Electronic Nano System, took advantage of the bulk micromachining technology in their IR spectrometer fabrication [31-33]. Two or more wafers are used to build a device structure and bonded together to form an FPI monochromator. A pyroelectric IR detector is packaged with the FPI-based

monochromator in TO-8 package and mounted on a control board as a final product. Bulk micromachining enabled Infra Tec to simplify the FPI fabrication process significantly. However, they paid the price with expensive and time-consuming packaging process.

Initially, my dissertation project was a collaboration between Dr. Joel Kubby's adaptive optics group in the Baskin school of engineering (SOE) at the University of California at Santa Cruz (UCSC) and the EPIR technologies to produce a micro IR spectrometer. Located in Bollingbrook, IL, the EPIR technologies (http://epirtech.com/) is a company specialized in fabricating a broad band IR sensor based on a mercury-cadmium-telluride (HgCdTe, MCT) ternary semiconductor material. By adjusting the ratio of each element in the compound, the MCT can be tuned to response to the IR in different spectral region. For example, $Hg_{0.7}Cd_{0.3}Te$ can detect the IR with 3 – 5 μm wavelength in the MWIR region, and $Hg_{0.8}Cd_{0.2}Te$ the IR with 8 – 12 μm wavelength in the LWIR region. A proposal was submitted to the US Army for a portable improvised explosion device (IED) detection system based on their MCT detector. To fulfil the requirement of the public call for the proposal, the EPIR needed a partner who can provide the monochromator for their IED detection system. As an expert in MEMS-based adaptive optics research community, Dr. Kubby joined the venture and took the responsibility of monochromator fabrication and system integration. Our goal was to fabricate the FPI-based IR spectrometer specialized in explosive chemical detection, with a simple

and cost-effective process using a combination of surface and bulk micromachining technologies.

In this dissertation, a noble approach to fabricate an FPI-based monochromator to be used as a part of an IR spectrometer IDE detection system is proposed. Simple and cost-effective fabrication process is achieved with an innovative process flow design, and a proof of principle performance is demonstrated with the fabricated device. In the next chapter, some theoretical background for the project is presented. It is followed by the device and fabrication flow design considerations in chapter 3. Chapter 4 presents the results of the simulation performed before the device fabrication. The detailed fabrication process with the description of the process equipment is given in chapter 5. The performance of the fabricated device is demonstrated in chapter 6 with the description for the characterization equipment. Finally, in chapter 7, we discuss the result and present the further step that can be taken to improve the performance of our device.

CHAPTER 2. THEORETICAL BACKGROUND FOR THE DESIGN OF THE FPI FILTER

The overall goal of my dissertation project is the development of an optical filter in the LWIR, more specifically in a wavelength range of λ = 8-11 μm. Originally, it is to be used as a component of a low-cost, miniaturized LWIR imaging spectrometer that can reliably detect the IDE in the battle field using the presence and concentration of various gases in the environment. Our implementation of the required optical filter is a tunable MEMS-based Fabry-Perot interferometer (FPI) with a dielectric mirror. It is a special kind of dielectric mirror, called a distributed Bragg reflector (DBR), that comprises alternating layers of materials with high and low index of refraction. To tune the filtering wavelength of the device, we fabricate one of the membranes to move, by supporting it at four corners with beam springs (X-beam). A bias applied between two membranes actuates the movable membrane with electrostatic force. In this chapter, we review the theoretical background behind the working of the FPI, the DBR, and the electrostatic actuation of our MEMS device.

2.1 Fabry-Perot interferometer

The Fabry-Perot interferometer (FPI) is used as an optical filter in the current project. First proposed and manufactured by Charles Fabry and Alfred Perot in the late 1800's [16], the FPI, also known as an etalon, is an example of a multiple beam interferometer, where large numbers of mutually coherent beams are made to interfere. In principle, the FPI is the simplest configuration of an optical cavity. It consists of two flat, highly reflective surfaces (typically of metal or dielectric mirrors) placed in parallel to face each other from a certain distance away. Simple explanation

of the operation of the FPI is followed by more detailed consideration with analytic expressions for the reflectance, transmittance, and other quantities of interests, including the finesse, a number most often quoted as the figure of merit of the FPI. In this section, we will assume a perfect mirror surface without loss or phase shift to simplify the analysis.

Analogous to the acoustic wave on a string musical instrument, like a guitar or a violin for example, the electromagnetic (EM) waves of various frequencies, incident onto one side of a 1-dimensional optical cavity, interfere destructively inside the cavity, except the ones satisfying the standing wave condition

$$d = m\frac{\lambda_m}{2}, m = 1, 2, 3 \ldots \qquad \text{(eq. 2.1)}$$

where d is the distance between two mirrors, λ_m the wavelength of EM wave in the optical cavity, and m a natural number. The value of m, called an order of interference, is the number of times a half the wavelength ($\frac{\lambda_m}{2}$) can fits into the optical cavity. In other words, the value of m determines the mode of each allowed EM wave in the cavity. To see how the FPI works as an optical filter, consider a beam of light incident on one side of the optical cavity, consists of two partially reflecting and partially transmitting mirrors. As the light enters the cavity from one side of the FPI, only specific modes of EM waves satisfying equation 2.1 are sustained inside. The second mirror can transmit only these waves to the other side of the FPI. Thus, the wave with wavelength $\lambda_m = \frac{2d}{m}$ will be transmitted through the FPI.

This simplified discussion of the working of the FPI as an optical cavity presents an occasion to introduce the first quantity of interests, the free spectral range (FSR). As mentioned above, given a specific cavity length d, EM waves with infinitely many different wavelengths (one for each value of m in equation 2.1) can pass through the FPI simultaneously. To discriminate the wavelength filtered through the FPI unambiguously, therefore, we need to limit the spectral range available within two adjacent peaks in the transmitted EM wave spectrum. The FSR is the separation between two neighboring resonant peaks in the transmitted EM wave spectrum. In terms of wavelength, it is given by

$$FSR = \lambda_m - \lambda_{m+1} = \frac{2d}{m} - \frac{2d}{m+1} = \frac{2d}{m(m+1)} = \frac{\lambda_m}{m+1}, m = 1,2,3 \ldots \quad \text{(eq. 2.2)}$$

Simpler expression, without any dependence on the order of interference *m*, can be obtained if we use the frequency instead of the wavelength to write FSR. By using equation 2.1 and $\lambda = \frac{c}{\nu}$,

$$FSR = \nu_{m+1} - \nu_m = \frac{c}{2d} \quad \text{(eq. 2.3).}$$

In short, the FSR tells us that we have half the wavelength spectral range around a transmission peak before we run into other peaks

The expression for the reflectance and transmittance of the FPI can most easily be found by following the approach that G. B. Airy first used in 1833 [42]. He derived the expression for the reflectance and transmittance that results from a multiple interference of the EM waves in three different materials. A typical example of this phenomenon is a multicolored pattern we observe on an oil slick after rain.

The air, thin layers of oil, and the water underneath provide three layers of materials. The beautiful, multicolored pattern is a result of interference among multiple beams repeatedly reflected and refracted on two boundaries. In his derivation, Airy added up the amplitude of multiple reflections and refractions occurring at the two interfaces to find the total reflectance and transmittance.

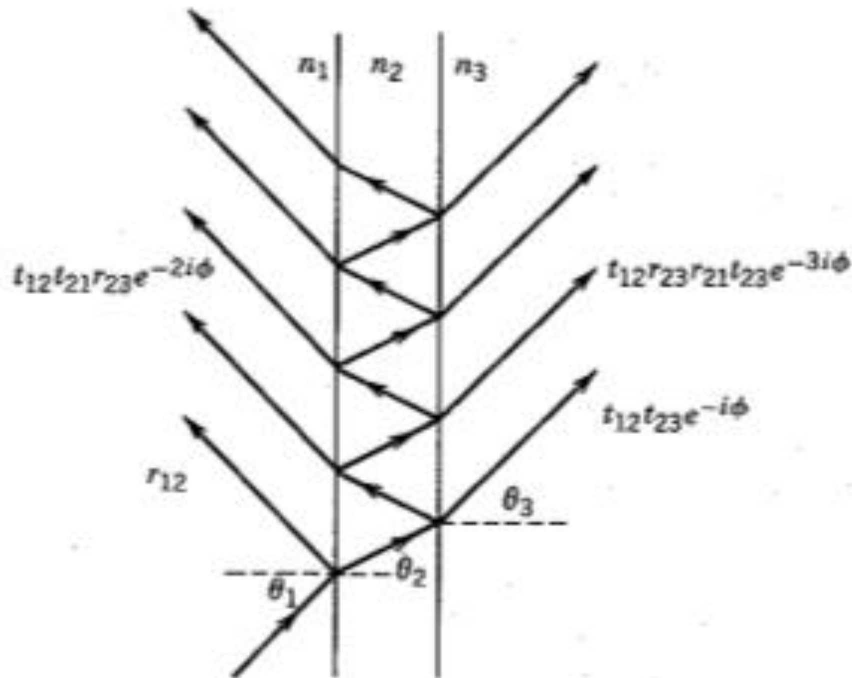

Fig. 2.1 Airy summation. A stack of three materials with index of reflection n_1, n_2, and n_3, in the order shown in the figure. An EM-wave incident from the left, partially reflected (r_{12}) and partially transmitted (t_{12}) at the 1-2 boundary. The beam t_{12} proceeds in the second material toward the 2-3 boundary. There, it partially reflects and transmits again ($t_{12}r_{23}e^{-i\phi}$, and $t_{12}t_{23}e^{-i\phi}$, respectively). The transmitted beam continues in material 3. The reflected one, however, partially reflects and transmits again as $t_{12}r_{23}r_{21}e^{-2i\phi}$, and $t_{12}r_{23}t_{21}e^{-2i\phi}$, respectively. The transmitted beam continues in material 1, and the twice reflected beam will continue producing the multiple reflections and transmissions as shown in the figure. The figure is taken from [42]

Specifically, consider a beam of EM waves fall onto the interface between the medium 1 and medium 2, with the reflection and transmission coefficients r_{12} and t_{12}, respectively. At this first boundary, a part of the beam is reflected back into medium 1 and the rest transmitted into medium 2. The transmitted EM waves continuously get reflected back and forth in the medium 2, at two interfaces as shown in figure 2.1. On each subsequent reflection, a part of the beam also transmits into the other side of the boundary. The reflection coefficient of the entire structure in figure 2.1 can be obtained, therefore, by adding the amplitude of all the lights in medium 1, except the incident light.

$$r = r_{12} + t_{12}t_{21}r_{23}e^{-2i\varphi} + t_{12}t_{21}r_{23}r_{21}r_{23}e^{-4i\varphi} + \cdots$$

$$= r_{12} + \frac{t_{12}t_{21}r_{23}e^{-2i\varphi}}{1-r_{21}r_{23}e^{-2i\varphi}}$$

$$= \frac{r_{12}+r_{23}e^{-2i\varphi}}{1+r_{12}r_{23}e^{-2i\varphi}} \qquad \text{(eq. 2.4)}$$

where we used the results from the Stokes treatment of reflection and refraction based on the principle of reversibility ($r21 = -r12$ and $t_{12}t_{21} - r_{12}r_{21} = 1$). Similarly, we can find the transmission coefficient by adding all the lights in medium 3.

$$t = t_{12}t_{23}e^{-i\varphi}\left(1 + r_{23}r_{21}e^{-2i\varphi} + \left(r_{23}r_{21}e^{-2i\varphi}\right)^2 + \cdots\right)$$

$$= \frac{t_{12}t_{23}e^{-i\varphi}}{1-r_{21}r_{23}e^{-2i\varphi}}$$

$$= \frac{t_{12}t_{23}e^{-i\varphi}}{1+r_{12}r_{23}e^{-2i\varphi}} \qquad \text{(eq. 2.5)}$$

Here the phase factor ϕ accounts for the optical path difference between two successive reflected or transmitted lights, and is given by

$$\varphi = \frac{2\pi d}{\lambda} n_2 cos\theta_2 \qquad \text{(eq. 2.6)}$$

where d, θ_2 and n_2 are the thickness, the angle and the index of refraction of the medium 2.

Compared with the configuration in figure 2.1, where a material 2 is immersed between materials 1 and 3 on each side, a typical FPI consists of two mirrors separated by a distance d. The two mirrors of the FPI are represented by the interfaces between two different materials in figure 2.1. The reflection and transmission coefficients of the first and the second mirrors are denoted by r_{12} and t_{12}, and r_{23} and t_{23}, respectively. If we further assume that two mirrors are symmetric, we have $r_{12} = r_{32}$, and $t_{12} = t_{32}$. Therefore, from equations 2.4 and 2.5 and the Stokes reversal treatments, the coefficients of reflection r_{FP}, and that of transmission t_{FP}, for the FPI is given by

$$r_{FP} = \frac{(1-e^{-2i\varphi})\sqrt{R}}{1-Re^{-2i\varphi}} \qquad \text{(eq. 2.7)}$$

$$t_{FP} = \frac{Te^{-i\varphi}}{1-Re^{-2i\varphi}}, \qquad \text{(eq. 2.8)}$$

where $R = {r_{12}}^2 = {r_{23}}^2, T = t_{12}t_{23}$ are the mirror reflectance and transmittance, respectively. When normalized to the intensity of the incident beam of lights, then, from equations 2.7 and 2.8, the reflectance R_{FP}, and the transmittance T_{FP}, of the FPI is given by

$$R_{FP} = |r_{FP}|^2 = \frac{4Rsin^2\varphi}{(1-R)^2+4Rsin^2\varphi} \qquad \text{(eq. 2.9)}$$

$$T_{FP} = |t_{FP}|^2 = \frac{(1-R)^2}{(1-R)^2+4Rsin^2\varphi} \qquad \text{(eq. 2.10)}$$

From equation 2.10, we can see that the maximum transmittance of 100% occurs whenever $sin^2\varphi = 0$, or

$$\varphi = \frac{2\pi d}{\lambda} n_2 cos\theta_2 = m\pi, m = 1,2,3 \dots \qquad \text{(eq. 2.11)}$$

Assuming a normal incidence ($\theta_i = 0$), we can verify that equation 2.11 is identical to equation 2.1, the condition for the EM wave transmission through the FPI. We also observe the following fact. In the derivation above, the loss of the EM wave through this idealized FPI is completely ignored. Accordingly, we should have $R + T = 1$ from the conservation of energy, which indeed is satisfied by equations 2.9 and 2.10.

In most spectroscopy studies, we don't expect to get the transmission peak as a spectral line of a single frequency. Instead, what we get is a certain distribution of signals spread over a range of frequencies, usually with a maximum located around the middle, and dropped off on either side of the peak. Thus, we might not be able to discriminate or resolve two such peaks if they are located close together in the spectrum and overlap each other. The full width at the half maximum (FWHM), also known as a bandwidth, of this spectral distribution of the signal is often used as a measure of the resolution power of a spectroscopy system. The FWHM of the transmission spectrum of the FPI can be derived from equation 2.10 by letting $T_{FP} = \frac{1}{2}$, or $sin^2\varphi = \frac{(1-R)^2}{4R}$. Assuming the mirror reflectance R close to 1, and with an approximation of $sin\varphi \approx \varphi$ for small φ, we have $\varphi = m\pi \pm \frac{1-R}{2\sqrt{R}}$, and the uncertainty in phase angle $\Delta\varphi$ at the FWHM as

$$\Delta\varphi = 2\frac{1-R}{2\sqrt{R}} \quad \text{(eq. 2.12)}$$

By substituting the definition of φ (equation 2.6) with $\theta = 0$ (normal incidence), into equation 2.12, the FWHM in terms of frequency $\Delta\nu_{\frac{1}{2}}$ is given by

$$\Delta\nu_{\frac{1}{2}} = \frac{c}{2d}\frac{1-R}{\pi\sqrt{R}} \quad \text{(eq. 2.13)}$$

Approximating $\Delta\nu$ with $d\nu = \frac{-c}{\lambda^2}d\lambda$, the FWHM as a function of wavelength $\Delta\lambda_{\frac{1}{2}}$ is nominally given by

$$\Delta\lambda_{\frac{1}{2}} = \frac{\lambda}{m}\frac{1-R}{\pi\sqrt{R}} \quad \text{(eq. 2.14)}$$

Another measure of resolving power of a spectroscopy system is called the spectral resolution. The spectral resolution ***R*** is defined as the ratio between a specific wavelength of the EM wave and the FWHM at the given wavelength. In other words, the spectral resolution ***R*** in terms of wavelength is

$$\boldsymbol{R} = \frac{\lambda}{FWHM} = \frac{m\pi\sqrt{R}}{1-R} \quad \text{(eq. 2.15)}$$

The FWHM and the spectral resolution ***R***, when expressed as a function of wavelength, all depend on the order *m* of interference. A quantity to characterize the resolving power of the FPI, that is independent of the order m, is called the reflection finesse, or simply finesse. The finesse F, often used as the main figure of merit of the FPI, is the ratio of the FSR and the FWHM. Clearly, then, the meaning of F is the number of times the peak with the certain width (FWHM) fits into the separation between adjacent peaks (FSR). The finesse F is given by

$$F = \frac{FSR}{FWHM} = \frac{\pi\sqrt{R}}{1-R} \quad \text{(eq. 2.16)}$$

From equation 2.16, we observe that the finesse F is indeed independent of the order *m* of interference. We can also see that the spectral resolution ***R*** is simply a product of the order of interference *m* and the finesse F.

The choice of order m used in the operation of the FPI needs to balance two conflicting design requirements. On one hand we have wider FSR with lower order of operation. On the other hand, both the FWHM and the spectral resolution ***R*** improve as higher order is used. In a communication application such as wavelength-division multiplexing where small FWHM and a relatively narrow tuning range are required, the FPI is operated in a higher mode. In many spectroscopy applications where the wider tuning range is desired, however, lower operation mode is needed. The smaller separation distance is preferred due to the restriction on the physical size of the device, and on the actuation bias voltage (described in the electrostatic actuation section). Therefore, in our design of the device, we choose to use the lowest order of operation, $m = 1$. Once the order of operation is determined, the reflectance of the mirror R can be adjusted to improve the performance of the FPI. For a majority of applications, it is done by increasing the finesse F and decreasing the FWHM, as this would allow for higher spectral resolution ***R***. After inspecting equations 2.14, 2.15 and 2.16, we see that the values of the finesse F, the spectral resolution ***R***, and the FWHM all improved as the mirror reflectance R increases. The dielectric mirror, including its reflectance, will be discussed in the next section.

2.2 The Distributed Bragg Reflector

As reviewed in the previous section, every figure of merit (the FWHM, the spectral resolution ***R***, and the Finesse) of the FPI is improved if mirrors with a high value of reflectance are used to construct the optical cavity. Therefore, developing a highly reflective mirror with low loss in our spectrum of interest is one of the most critical components of the project. The Distributed Bragg reflector (DBR), also known as a Quarter Wave Stack (QWS), is considered a promising candidate for a couple of reasons: First, being a dielectric mirror, the DBR is almost lossless compared to a metallic mirror. The reflectance and the absorption of a metallic mirror both are improved with the increasing thickness of the metal layer. Thus, higher reflectance produces more absorption, which in turn decreases the transmission peak of the FPI significantly. Since modern micro-fabrication technology made the deposition of dielectric films as easy as metallic layers, a dielectric mirror became a preferred choice, especially in MEMS FPI [28]. Most importantly, with dielectric mirrors one can tailor the configuration of the DBR so that its spectral behavior suits the need of the project. The DBR consists of two dielectric materials, one with high index of reflection and the other with low index of reflection, stacked in alternating order. The thickness of each layer is a quarter of the wavelength of the light in the layer material. The number of double layers of two different dielectric materials, that we will call a 'stack' in this dissertation, is one parameter we can adjust.

The physics behind and the analytic expression for the reflectance of the DBR is presented now. Hecht [18] presents an intuitive and practical way to analyze multi-layer dielectric films using matrix algebra. Instead of dealing with rays from multiple reflections and transmissions through the films (for example, Airy's method we used in the previous section), the total electric and magnetic fields at the boundaries of each medium are represented as a two-dimensional column vector. To satisfy the Maxwell's equations, the boundary conditions require that the tangential components of both the electric and magnetic fields need to be continuous at these interfaces. These boundary conditions produce two equations that relate the electric and magnetic field at these two boundaries. The system of these two linear equations can be rewritten into a single matrix equation, where all the information relating the fields at the two adjacent boundaries are included in a 2 by 2 matrix called a characteristic matrix, or optical transfer matrix. Consequently, when you have a system of many layers of materials deposited on a substrate, the characteristic matrix for the entire system, that relates the incident wave with the wave in the substrate, can be obtained by multiplying the characteristic matrices for individual layers in the proper order. An analysis method using matrix algebra almost identical to that found in Hecht [18] is also in Macleod [28]. The only difference between them is the quantities used to represent the EM wave. In Hecht [18], the total electric and magnetic field E and H at each boundary are used to represent the EM wave as a two-dimensional column vector. Macleod [28] uses an optical admittance, a ratio of H and E, instead. The

characteristic matrix method reviewed below follows the notions and logic presented in Hecht [18].

Consider first an s-wave, also known as a TE wave since its electric field vector E is transverse to the plane of incidence. On figure 2.2, a situation similar to the one reviewed in the section 2.1 is depicted where three different materials with indices of refraction, n_0, n_1, and n_s, respectively, are adjacent to each other. An s-wave is impinging from medium 1 onto medium 2. There occur reflection and transmission of the incident EM wave on the first boundary (Boundary I). The transmitted part of the s-wave reflects and transmits once more when it hits the second boundary (Boundary II). As described in the previous section, there are multiple beams from successive reflections and transmissions at each boundary. However, all waves in the same direction are added up and represented by E_{rI}, E_{tI}, E_{rII}, and E_{tII} for total electric field reflected at boundary I, total electric field transmitted at boundary I, total electric field reflected at boundary II, and total electric field transmitted at boundary II, respectively. Four magnetic fields are defined similarly.

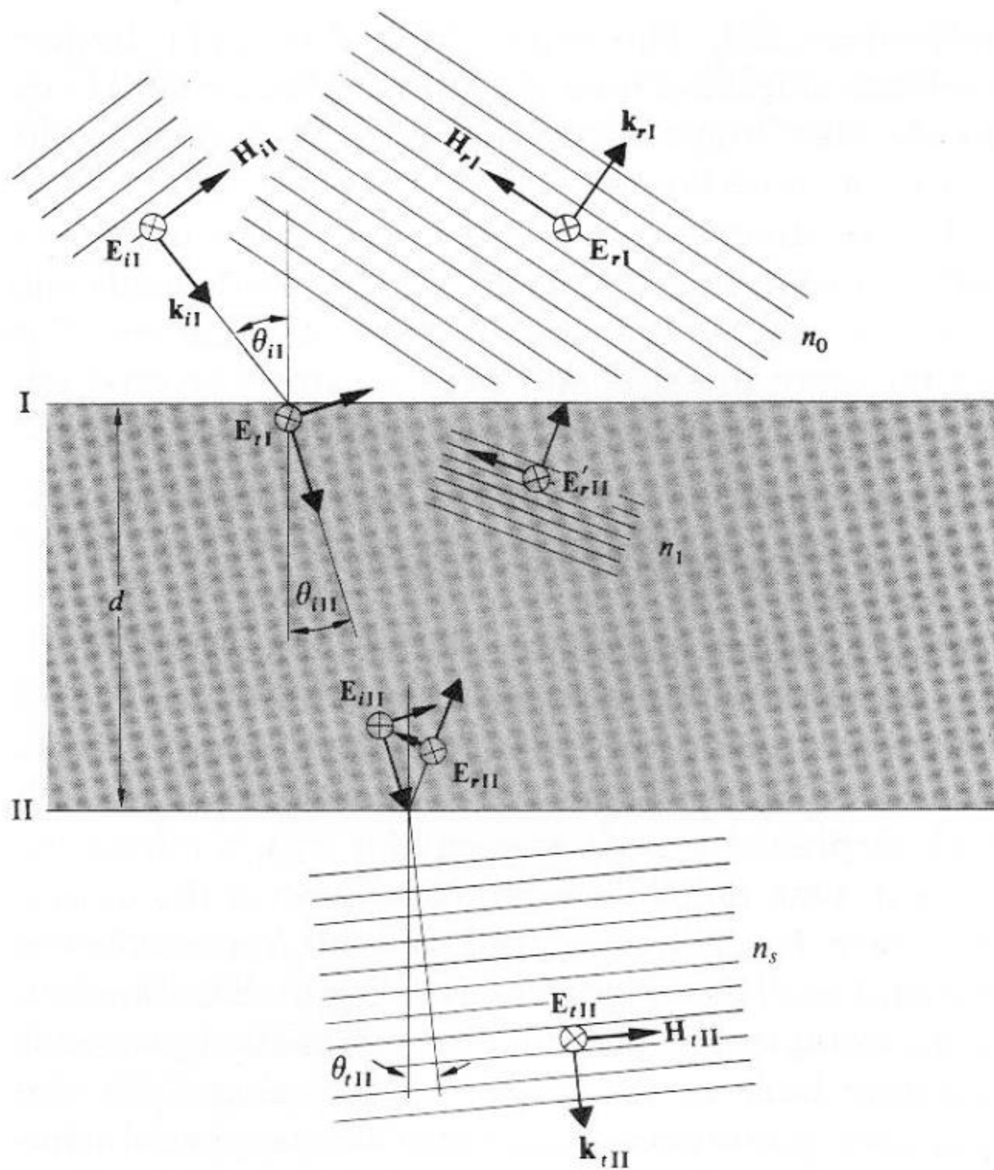

Fig. 2.2 Fields at the boundaries of three different media, with the index of refraction n_0, n_1 and n_s, respectively. E_{iI}, E_{tI}, and E_{rI} represent the incident, transmitted, and reflected E-fields at the boundary I, respectively. At the boundary II, E_{iII}, E_{tII}, and E_{rII} are similarly defined. See the paragraph below for detailed description of the figure. The figure is taken from [18].

From the Maxwell's equations, we write the following boundary conditions. At boundary I,

$$E_I = E_{iI} + E_{rI} = E_{tI} + E'_{rII} \qquad \text{(eq.2.17)}$$

and

$$H_I = \sqrt{\frac{\varepsilon_0}{\mu_0}}(E_{iI} - E_{rI})n_0 cos\theta_{iI} = \sqrt{\frac{\varepsilon_0}{\mu_0}}\left(E_{tI} - E'_{rII}\right)n_1 cos\theta_{iII} \qquad \text{(eq. 2.18)}$$

where we used one of the consequences of the Maxwell's equations that in non-magnetic medium $\vec{E}$ and $\vec{H}$ are related by: $\vec{H} = \sqrt{\frac{\varepsilon_0}{\mu_0}} n\hat{k} \times \vec{E}$.

At boundary II,

$$E_{II} = E_{iII} + E_{rII} = E_{tII} \qquad \text{(eq. 2.19)}$$

and

$$H_{II} = \sqrt{\frac{\varepsilon_0}{\mu_0}}(E_{iII} - E_{rII})n_1 cos\theta_{iII} = \sqrt{\frac{\varepsilon_0}{\mu_0}} E_{tI} n_s cos\theta_{tII} \qquad \text{(eq. 2.20)}$$

To account for the phase shift that the s-wave experiences as it traverses trough the medium 2, we let $E_{iII} = E_{tI}e^{-ik_0h}$, and $E_{rII} = E'_{rII}e^{ik_0h}$, where $h = \frac{2n_1 dcos\theta_{iII}}{2}$. (See Mathematical Derivation I at the end of the chapter for the derivation of this result.) With these equations, now we can rewrite equations 2.19 and 2.20 as

$$E_{II} = E_{tI}e^{-ik_0h} + E'_{rII}e^{ik_0h} \qquad \text{(eq. 2.21)}$$

and

$$H_{II} = \sqrt{\frac{\varepsilon_0}{\mu_0}}\left(E_{tI}e^{-ik_0h} - E'_{rII}e^{ik_0h}\right)n_1 cos\theta_{iII} \qquad \text{(eq. 2.22)}$$

Solving equations 2.21 and 2.22 for E_{tI} and E'_{rII} and substituting them into equations 2.17 and 2.18 yields

$$E_I = E_{II} cos k_0 h + \frac{H_{II} i sin k_0 h}{Y_1} \qquad \text{(eq. 2.23)}$$

and

$$H_I = E_{II} Y_1 i sin k_0 h + H_{II} cos k_0 h \qquad \text{(eq. 2.24)}$$

where $Y_1 = \sqrt{\frac{\varepsilon_0}{\mu_0}} n_1 cos\theta_{iII}$.

The system of linear equations 2.23 and 2.24 can be rewritten into a single matrix equation,

$$\begin{bmatrix} E_I \\ H_I \end{bmatrix} = m_1 \begin{bmatrix} E_{II} \\ H_{II} \end{bmatrix},$$

where m_1, the characteristic matrix that relates E and H fields at a boundary, is given by

$$m_1 = \begin{bmatrix} cos k_0 h & \frac{i sin k_0 h}{Y_1} \\ Y_1 i sin k_0 h & cos k_0 h \end{bmatrix} \qquad \text{(eq. 2.25)}$$

With the similar calculations, it can be shown that for a p-wave or TM wave, where magnetic field is perpendicular to the plane of incidence, we find the same characteristic matrix, except $Y_1 = \sqrt{\frac{\varepsilon_0}{\mu_0}} \frac{n_1}{cos\theta_{iII}}$. See Mathematical Derivation II at the end of the chapter for a detailed derivation.

If we have more than one layer of material in the middle, we can obtain one characteristic matrix for each such medium that relates the fields at its two boundaries. For example, with two layers of materials deposited on a substrate, we

have $\begin{bmatrix} E_I \\ H_I \end{bmatrix} = m_1 \begin{bmatrix} E_{II} \\ H_{II} \end{bmatrix}$ and $\begin{bmatrix} E_{II} \\ H_{II} \end{bmatrix} = m_2 \begin{bmatrix} E_{III} \\ H_{III} \end{bmatrix}$, which in turn can be combined

into $\begin{bmatrix} E_I \\ H_I \end{bmatrix} = m_1 m_2 \begin{bmatrix} E_{III} \\ H_{III} \end{bmatrix}$. To generalize, if we have n number of layers deposited on a substrate, the E and H fields at the first and the last boundaries can be written as

$$\begin{bmatrix} E_I \\ H_I \end{bmatrix} = m_1 m_2 \ldots m_n \begin{bmatrix} E_{n+1} \\ H_{n+1} \end{bmatrix} = m \begin{bmatrix} E_{n+1} \\ H_{n+1} \end{bmatrix} \qquad \text{(eq. 2.26)}$$

where each m_i has its corresponding values of n and h. The characteristic matrix m for the entire system is, then, given by

$$m = m_1 m_2 \ldots m_n = \begin{bmatrix} m_{11} & m_{12} \\ m_{21} & m_{22} \end{bmatrix}.$$

Finally, the coefficients of reflection and transmission can be obtained as follows. By defining $Y_0 = \sqrt{\frac{\varepsilon_0}{\mu_0}} n_0 cos\theta_{iI}$ and $Y_{n+1} = \sqrt{\frac{\varepsilon_0}{\mu_0}} n_n cos\theta_{tn}$, equation 2.26 can be rewritten as $\begin{bmatrix} E_{iI} + E_{rI} \\ (E_{iI} - E_{rI})Y_0 \end{bmatrix} = \begin{bmatrix} m_{11} & m_{12} \\ m_{21} & m_{22} \end{bmatrix} \begin{bmatrix} E_{tn+1} \\ E_{tn+1} Y_{n+1} \end{bmatrix}$. With $r = \frac{E_{rI}}{E_{iI}}$ and $t = \frac{E_{tn+1}}{E_{iI}}$, the above matrix equation becomes $1 + r = m_{11} t + m_{12} Y_{n+1} t$ and $(1 - r)Y_0 = m_{21} t + m_{22} Y_{n+1} t$, or

$$r = \frac{Y_0 m_{11} + Y_0 Y_{n+1} m_{12} - m_{21} - Y_{n+1} m_{22}}{Y_0 m_{11} + Y_0 Y_{n+1} m_{12} + m_{21} + Y_{n+1} m_{22}} \qquad \text{(eq. 2.27)}$$

and

$$t = \frac{2Y_0}{Y_0 m_{11} + Y_0 Y_{n+1} m_{12} + m_{21} + Y_{n+1} m_{22}} \qquad \text{(eq. 2.28)}$$

Let's consider a simple example to make sense of all the mathematics we have been through. Depicted in figure 2.3 is a schematic of a DBR with two alternating layers of material 1 and 2, with their indices of refraction n_1 and n_2, and the thickness

d_1 and d_2, respectively. The index of refraction of the incident media is n_0, and n_s that of the substrate. The index of refraction n_1 is assumed to be higher than n_2 ($n_1 > n_2$) and a normal incidence of light is also assumed ($\theta_i = 0$). In such case, it is easy to see how the DBR works qualitatively. We just need to remind ourselves the consequence of Fresnel's equations for the normal incidence, $r_{12} = \frac{n_1 - n_2}{n_1 + n_2}$ and $t_{12} = \frac{2n_1}{n_1 + n_2}$. They are the coefficients of reflection and transmission when a normally incident EM wave, traveling from material 1 to material 2, is reflected and transmitted at the boundary. Here we can see that t_{12} is always positive, but the sign of r_{12} depends on the relative magnitude of n_1 and n_2. When $n_1 > n_2$, r_{12} is positive. When $n_1 < n_2$, it is negative. The sign of r and t signifies the phase change at the boundary. When it is positive, the EM wave suffers no phase change. When negative, there is π or 180° phase shift. In other words, there will be no phase change when a light beam is transmitted through a boundary, or it is reflected as it traverses from a material with higher index of refraction to a lower index material. On the other hand, if the light travels from a lower index of refraction material into a higher index one, there is 180° phase shift. In figure 3, beam A suffers 180° phase shift upon a reflection at air-1boundary, relative to the incident light. Beam B is in phase with beam A since it travels twice the distance of $\frac{\lambda}{4}$, but no phase shift upon a reflection at 1-2 boundary, results in 180° phase shift relative to the incident beam. Similarly, beam C is also in phase with A since it travels a whole wavelength ($4 \times \frac{\lambda}{4}$) and suffers 180° phase shift at 2-1 boundary. Therefore, all the lights reflected at each boundary are in phase with

each other and interfere constructively. Consequently, they give rise to a substantial amount of light reflected from the DBR mirror.

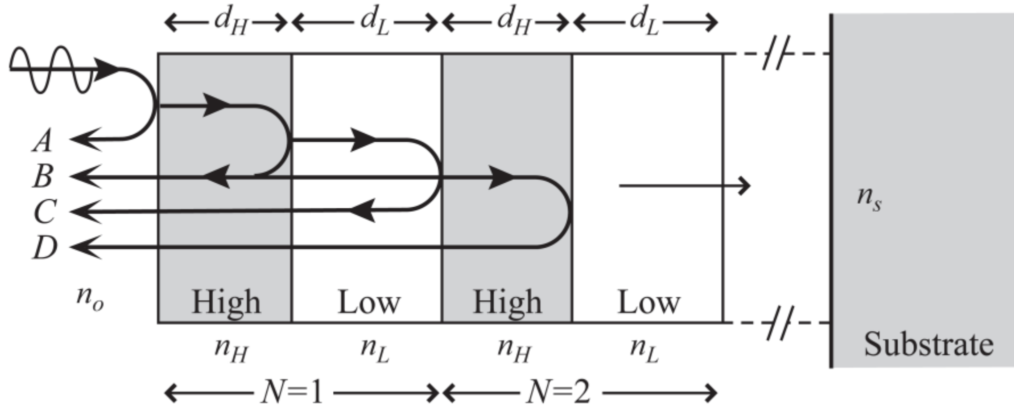

Fig. 2.3 The Distributed Bragg Reflector with two alternating layers of material High and Low, with their indices of refraction n_H and n_L, and the thickness d_H and d_L, respectively. The index of refraction of the incident media is n_0, and n_s that of the substrate. The index of refraction n_H is higher than n_L ($n_H > n_L$) and a normal incidence of light is also assumed ($\theta_i = 0$). See the paragraph above the figure for the description of how the DBR works qualitatively. The figure is taken from [21]

Though instructive and insightful, the simplified description of the DBR above does not take into account the effect of multiple reflection occurring at each successive boundary as described in section 2.1 (i.e. Airy summation). Quantitative analysis based on the characteristic matrix method presented earlier in this section is followed. For a quarter wave stacks ($d = \frac{\lambda_i}{4}$) with a normal incident light ($\theta_i = 0$), $k_0 h = k_0 n_i d cos\theta_i = \frac{2\pi}{\lambda_0} n_i \frac{\lambda_i}{4} = \frac{2\pi}{\lambda_0} n_i \frac{\lambda_0}{4n_i} = \frac{\pi}{2}$. The characteristic matrix m_i, then, is given by

$$m_i = \begin{bmatrix} cosk_0h & \frac{isink_0h}{Y_i} \\ Y_iisink_0h & cosk_0h \end{bmatrix} = \begin{bmatrix} 0 & \frac{i}{Y_i} \\ iY_i & 0 \end{bmatrix} = \begin{bmatrix} 0 & \frac{i}{\sqrt{\frac{\varepsilon_0}{\mu_0}}n_i} \\ i\sqrt{\frac{\varepsilon_0}{\mu_0}}n_i & 0 \end{bmatrix}.$$

Thus, the characteristic matrix for a single stack of double layers m_1m_2 is

$$m_1m_2 = \begin{bmatrix} 0 & \frac{i}{\sqrt{\frac{\varepsilon_0}{\mu_0}}n_1} \\ i\sqrt{\frac{\varepsilon_0}{\mu_0}}n_1 & 0 \end{bmatrix} \begin{bmatrix} 0 & \frac{i}{\sqrt{\frac{\varepsilon_0}{\mu_0}}n_2} \\ i\sqrt{\frac{\varepsilon_0}{\mu_0}}n_2 & 0 \end{bmatrix} = \begin{bmatrix} \frac{-n_2}{n_1} & 0 \\ 0 & \frac{-n_1}{n_2} \end{bmatrix},$$

and for N such stacks,

$$m = m_1m_2{}^N = \begin{bmatrix} \left(\frac{-n_2}{n_1}\right)^N & 0 \\ 0 & \left(\frac{-n_1}{n_2}\right)^N \end{bmatrix}.$$

Substituting this result into equation 2.27 and with a bit of algebra, we have an expression for the coefficient of reflection r as

$$r = \frac{\left(\frac{-n_2}{n_1}\right)^N \sqrt{\frac{\varepsilon_0}{\mu_0}}n_0 - \left(\frac{-n_1}{n_2}\right)^N \sqrt{\frac{\varepsilon_0}{\mu_0}}n_s}{\left(\frac{-n_2}{n_1}\right)^N \sqrt{\frac{\varepsilon_0}{\mu_0}}n_0 + \left(\frac{-n_1}{n_2}\right)^N \sqrt{\frac{\varepsilon_0}{\mu_0}}n_s} = \frac{n_1{}^{2N} - \left(\frac{n_0}{n_s}\right)n_2{}^{2N}}{n_1{}^{2N} + \left(\frac{n_0}{n_s}\right)n_2{}^{2N}}.$$

Finally, the reflectance of the DBR illustrated in figure 3, upon a normal incidence of light with the wavelength $\lambda_0 = 4n_id_i$ is given by

$$R_N = |r|^2 = \left[\frac{n_1{}^{2N} - \left(\frac{n_0}{n_s}\right)n_2{}^{2N}}{n_1{}^{2N} + \left(\frac{n_0}{n_s}\right)n_2{}^{2N}}\right]^2, \text{ (eq. 2.29).}$$

A couple of general observations can be made for the reflectance of the DBR. From equation 2.29, we can see that the reflectance R is increased with N, the number of the stacks of high-low indices of refraction double layer pairs. R is also increased as the index contrast, defined as $\frac{n_H}{n_L}$, the ratio of the indices of refraction increases, or

putting it differently, as the difference in the index of refraction of the two materials increases. These observations can be seen graphically from the spectral response of the reflectance of the DBR shown in figure 2.4.

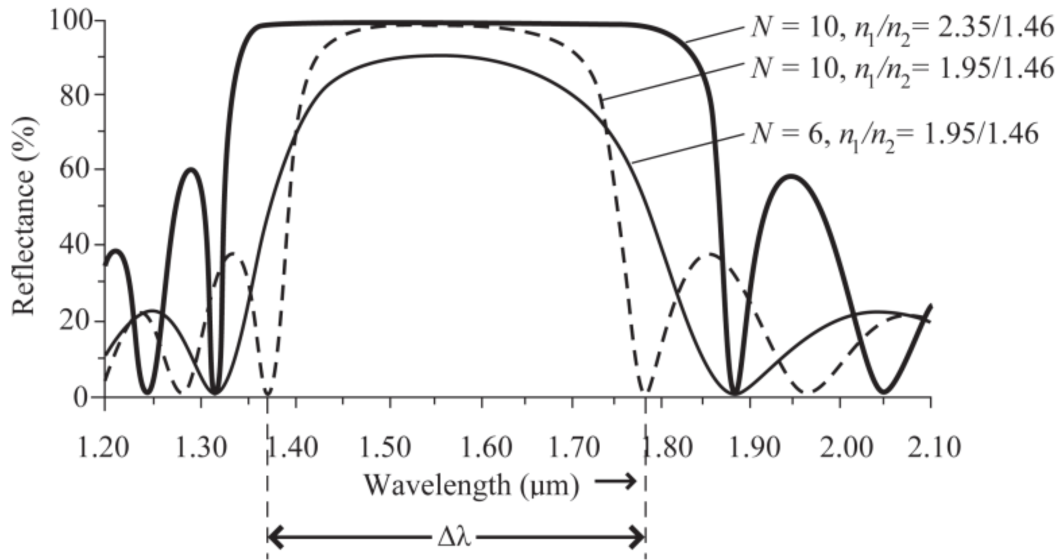

Fig. 2.4 The Spectral Response of the DBR. The reflectance R of the DBR improves as the number of high/low index layer stacks increase. Similarly, higher R is achieved with the higher index contrast. The higher index contrast widens the bandwidth of the DBR as well. The bandwidth of the DBR, Δλ, where the high reflectance is maintained is also shown in the figure. The bandwidth can be adjusted to cover the entire spectrum of interest with the higher index ratio. The figure is taken from [21]

One other important feature is the band width of DBR, denoted Δλ, in figure 2.4. We assume the incident light with the design wavelength of the DBR (λ = 1.55 µm in the figure) or $k_0 h = \frac{\pi}{2}$, when the reflectance of the DBR (equation 2.29) is derived. However, we observe that the high reflectance is maintained in a small range of wavelength centered at the design wavelength of the DBR, and then abruptly falls down and exhibits oscillatory behavior with decreasing amplitude. The band

width Δλ is the width of the region of spectrum where the reflectance is high and steady. Therefore, the DBR works as an efficient mirror not only at the design wavelength but also on the entire band width of the wavelength spectrum. We can take advantage of this fact when we design a device that will work on a range of wavelength such as the FPI described in this thesis with its operation wavelength $\lambda = 8 - 11\ \mu m$.

The expression for the band width is derived below. This derivation found in MacLeod [28] is rather a justification than a proof. Since we introduce the characteristic matrix method following Hecht [18], the notions and quantities used are adapted to those used by him. A mathematically rigorous proof of this result is given in Born and Wolf [8].

The transmittance T of a DBR can be obtained from equation 2.28

$$T = |t|^2 = \left|\frac{2Y_0}{Y_0 m_{11} + Y_0 Y_{n+1} m_{12} + m_{21} + Y_{n+1} m_{22}}\right|^2 \qquad \text{(eq. 2.30)}$$

where $Y_0 = \sqrt{\frac{\varepsilon_0}{\mu_0}} n_0 cos\theta_{iI}$ and $Y_{n+1} = \sqrt{\frac{\varepsilon_0}{\mu_0}} n_n cos\theta_{tn}$ as before, and m_{ij}'s are the components of the characteristic matrix for the entire DBR. If there is no DBR presents, the characteristic matrix becomes an identity matrix, and the transmittance in such a case, called T_0 is given as

$$T_0 = \frac{4{Y_0}^2}{(Y_0 + Y_{n+1})^2} \qquad \text{(eq.2.31).}$$

With a DBR presents, the Transmittance T will be less than T_0 ($T < T_0$) or $|Y_0 m_{11} + Y_0 Y_{n+1} m_{12} + m_{21} + Y_{n+1} m_{22}|^2 = (Y_0 m_{11} + Y_{n+1} m_{22})^2 + (Y_0 Y_{n+1} m_{12} + m_{21})^2 > (Y_0 + Y_{n+1})^2$, where we make use of the fact that m_{12} and m_{21} are imaginary

numbers (See equation 2.25). This will be true regardless of the values of m_{12} and m_{21}, therefore, we have $(Y_0 m_{11} + Y_{n+1} m_{22})^2 > (Y_0 + Y_{n+1})^2$. If we further assume the same incident and emergent materials ($Y_0 = Y_{n+1}$), the above condition can be simplified to $\left|\frac{m_{11}+m_{22}}{2}\right| > 1$.

For a DBR, the characteristic matrix m can be written as $m = (m_1 m_2)^N$, where m_1 and m_2 are the characteristic matrix of media 1 and 2, respectively, and N the number of stacks. Let $M = m_1 m_2$ (i.e. N=1). If $\left|\frac{M_{11}+M_{22}}{2}\right| > 1$, then $\left|\frac{m_{11}+m_{22}}{2}\right|$ tends to infinity as we increase N. This claim is made plausible when we consider $M^2 = L$. Then $L_{11} + L_{22} = M_{11}^2 + 2M_{12}M_{21} + M_{22}^2$. Now since determinant of M = $M_{11}M_{22} - M_{12}M_{21} = 1$ at the DBR design wavelength ($M = \begin{bmatrix} \frac{-n_2}{n_1} & 0 \\ 0 & \frac{-n_1}{n_2} \end{bmatrix}$) , we have $2M_{12}M_{21} = 2M_{11}M_{22} - 2$, and $L_{11} + L_{22} = M_{11}^2 + 2M_{11}M_{22} + M_{22}^2 - 2 = (M_{11} + M_{22})^2 - 2$. Let $\left|\frac{M_{11}+M_{22}}{2}\right| = 1 + \varepsilon$. Then $L_{11} + L_{22} = (2 + 2\varepsilon)^2 - 2 = 2 + 8\varepsilon + 4\varepsilon^2$. Squaring L once more, we have $L^2{}_{11} + L^2{}_{22} = (N_{11} + N_{22})^2 - 2 = (2 + 8\varepsilon + 4\varepsilon^2)^2 - 2 = 2 + 96\varepsilon + 16\varepsilon^2 + 64\varepsilon^3 + 16\varepsilon^4$. Continuing this way, we see that $\left|\frac{m_{11}+m_{22}}{2}\right| \rightarrow \infty$ as $N \rightarrow \infty$. We can also deduce from the equation 2.30 that as $\left|\frac{m_{11}+m_{22}}{2}\right|$ increases, the denominator of the equation increases and as a result the transmittance T of the DBR decreases. In other words, the reflectance R of the DBR increases as the number of stacks of double layers increases when $\left|\frac{M_{11}+M_{22}}{2}\right| > 1$.

Now, in general, $M = m_1 m_2 = \begin{bmatrix} cosk_0h & \frac{isink_0h}{Y_1} \\ Y_1 isink_0h & cosk_0h \end{bmatrix} \begin{bmatrix} cosk_0h & \frac{isink_0h}{Y_2} \\ Y_2 isink_0h & cosk_0h \end{bmatrix}$,

then $\left|\frac{M_{11}+M_{22}}{2}\right| = cos^2k_0h - \frac{1}{2}\left(\frac{Y_2}{Y_1} + \frac{Y_1}{Y_2}\right) sin^2k_0h > 1$ where the DBR maintains a high reflectance. Therefore, the boundary of the spectrum where the DBR maintains high reflectance can be found by $\left|\frac{M_{11}+M_{22}}{2}\right| = \left|cos^2k_0h - \frac{1}{2}\left(\frac{Y_2}{Y_1} + \frac{Y_1}{Y_2}\right) sin^2k_0h\right| = 1$ or

$$\frac{M_{11}+M_{22}}{2} = cos^2k_0h - \frac{1}{2}\left(\frac{Y_2}{Y_1} + \frac{Y_1}{Y_2}\right) sin^2k_0h = -1 \qquad \text{(eq. 2.32)}$$

Since $\frac{M_{11}+M_{22}}{2} = 1$ gives a condition ($sin^2k_0h = 0$) that is incompatible with the thickness of each layer, i.e. a quarter of the design wavelength, we throw it away on the physical ground. With $sin^2x + cos^2x = 1$, equation 2.32 further simplifies to

$$cos^2k_0h = \left(\frac{Y_1-Y_2}{Y_1+Y_2}\right)^2 \qquad \text{(eq. 2.33)}$$

Now $k_0h = k_0 n_i d cos\theta_i = \frac{2\pi}{\lambda_0} n_i \frac{\lambda_i}{4} = \frac{2\pi}{\lambda_0} n_i \frac{\lambda_0}{4n_i} = \frac{\pi}{2}$ at the design wavelength of the DBR. Let $\lambda^{'} = \lambda \pm \frac{1}{2}\Delta\lambda$ at the boundary where the reflectance drops rapidly. Then we have,

$$cos^2\left(\frac{\pi}{2}\frac{\lambda^{'}}{\lambda}\right) = cos^2\left[\frac{\pi}{2}\left(1 \pm \frac{1}{2}\frac{\Delta\lambda}{\lambda}\right)\right] = sin^2\left(\pm\frac{\pi}{4}\frac{\Delta\lambda}{\lambda}\right) \qquad \text{(eq. 2.34)}$$

From equations 2.33 and 2.34, we have $sin^2\left(\pm\frac{\pi}{4}\frac{\Delta\lambda}{\lambda}\right) = \left(\frac{Y_1-Y_2}{Y_1+Y_2}\right)^2$. Assuming a normal incident EM wave to simplify it further, we have $cos\theta_{iII} = cos\theta_{iIII} = 1$, and $\frac{Y_1-Y_2}{Y_1+Y_2} = \frac{\sqrt{\frac{\varepsilon_0}{\mu_0}} n_1 cos\theta_{iII} - \sqrt{\frac{\varepsilon_0}{\mu_0}} n_2 cos\theta_{iIII}}{\sqrt{\frac{\varepsilon_0}{\mu_0}} n_1 cos\theta_{iII} + \sqrt{\frac{\varepsilon_0}{\mu_0}} n_2 cos\theta_{iIII}} = \frac{n_1-n_2}{n_1+n_2}$. Finally, the fractional bandwidth $\frac{\Delta\lambda}{\lambda}$ of a DBR with a beam of light that is incident normally upon it, is given by

$$\frac{\Delta\lambda}{\lambda} = \frac{4}{\pi} sin^{-1}\frac{n_H - n_L}{n_H + n_L} = \frac{4}{\pi} sin^{-1}\frac{\frac{n_H}{n_L} - 1}{\frac{n_H}{n_L} + 1} \quad \text{(eq. 2.35)}$$

As seen on figure 2.4, the higher value of the index contrast widens the bandwidth $\Delta\lambda$, which is expected from equation 2.35. However, the bandwidth of the DBR does not improved by increasing the number of double layer stacks N.

2.3 An electrostatic actuator

As discussed in section 2.1, the wavelength of the EM wave that passes through the FPI is determined by the length of the optical cavity defined as the distance of the gap between the two mirrors of the FPI. In other words, once this gap distance is fixed the EM wave with only one specific wavelength can transmitted through the FPI. If we want the FPI to act as an optical filter over some spectrum of wavelength (λ= 8-11 μm for the current project), therefore, we need a mean to change this gap distance so that we can tune the FPI to accommodate the entire spectrum of interest. Among many possibilities of the tuning mechanism of the FPI, an electrostatic actuator, more specifically a parallel plate actuator is implemented in our design. The scalability into micro-size domain, the low power consumption, and the straightforward fabrication process made the electrostatic actuator one of the most common actuation methods in MEMS devices. Particularly for the current project, the physical configuration of the FPI, with two mirrors facing each other, is exactly the same as that of the parallel plate actuator, so the choice of parallel plate actuator for the actuation mechanism in our implementation is a natural one. In this section, we review the physical principle behind the parallel plate actuator, and present important equations describing its operation for the future reference in this thesis.

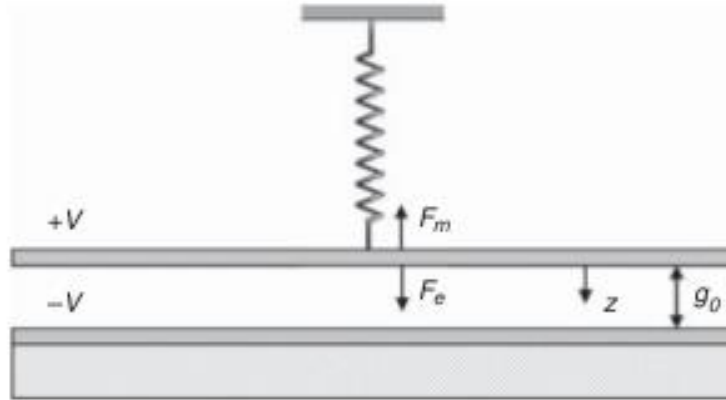

Fig. 2.5 Parallel Plates Actuator. Two conductive plates put in parallel to each other with an initial gap distance of g_0. One of the plates is designed to move freely. Two plates are biased with +/- V. Opposite charges accumulate on each plate, and an electrostatic attraction pulls them close. A restorative force, represented by spring in the figure, balances out the attraction, and the equilibrium distance of g_o-z in reached. The figure is taken from [27]

In a nutshell, the parallel plate actuator is a basic capacitor consists of two conducting plates faced each other in parallel. In the parallel plate actuator, one of the plates is release in the fabrication process and able to move in response to the applied bias. As we apply the bias, the attraction between the opposite charges accumulated on each plate pull them closer. Let us consider a parallel plate capacitor with an overlapping area of A and a spacing of z between two plate. The capacitance of such a capacitor is $C = \varepsilon\frac{A}{z}$, and the electric energy stored in this capacitor is given by

$$U = \frac{1}{2}CV^2 = \frac{1}{2}\varepsilon\frac{A}{z}V^2 \qquad \text{(eq. 2.36)}$$

where V is the applied bias voltage, and ε, the permittivity for the medium filling the gap. It is a product of ε_r and ε_0, where ε_r is dielectric constant or relative electrical

permittivity, and $\varepsilon_0 = 8.85 \times 10^{-14}$ (F/V) is the permittivity of free space. Given a certain bias voltage (i.e. V is held constant), the electrostatic force of attraction can be found by taking the derivative of the energy U with respect to the gap distance z.

$$F_e = \frac{-dU}{dz} = \frac{-1}{2}\varepsilon A V^2 \frac{d}{dz}\left(\frac{1}{z}\right) = \varepsilon \frac{A}{2}\frac{V^2}{z^2} \qquad \text{(eq. 2.37)}$$

To balance this attractive force, a mechanical restoring force is introduced in the design of the device. Various mechanical springs of different types are typically used to provide this restoring force. Thus, at equilibrium, the mechanical restoring force, given by the Hook's law, $F_k = -kz$, will be equal in magnitude and opposite in direction to the electrostatic force, given by $F_e = \varepsilon \frac{A}{2}\frac{V^2}{(g_0 - z)^2}$, where k is the spring constant, g_0 the initial distance between two plates, and z now denotes the change in the gap distance (See figure 2.5, and compare with equation 2.37). By equating F_k and F_e, we can find the distance between two plates at the equilibrium as a function of the applied bias voltage V.

However, graphical solution of the equation $F_k = F_e$ gives more insight into the relation between the gap distance (g_0-z) and the applied bias voltage V. A graph of F_k and series of graphs of F_e for a few different values of the bias voltage V are given in figure 2.6. At lower values of V, the graphs of F_k and F_e, with two different intersection points, gives two solutions for the gap distance. The larger of these two gap distances is discarded as physically impossible solution, as explained shortly. As the bias voltage increases, the graphs of F_k and F_e intersect at a single point. This is an onset of pull-in or snap-in phenomenon. This critical voltage at which the pull-in

sets in is called the pull-in voltage or V_p. With bias voltage larger than V_p, there is no common intersection of F_k and F_e. Thus, no equilibrium gap distance can be obtained. Physically, linearly growing F_k can no longer catch up with much faster growing F_e, and two plates will be pulled in rapidly until they make a contact with each other.

Let us quantify the pull-in condition in detail. At the onset of pull-in, the value and the slope of the graphs of F_k and F_e are identical. Assuming the air gap, from $F_k = F_e$, we have

$$kz = \varepsilon_0 \frac{A}{2} \frac{V^2}{(g_0 - z)^2} \qquad \text{(eq. 2.38)}$$

The condition $\frac{dF_k}{dz} = \frac{dF_e}{dz}$ gives

$$k = \varepsilon_0 A \frac{V^2}{(g_0 - z)^3} \qquad \text{(eq. 2.39)}$$

Canceling k from equations 2.38 and 2.39, and solving for z, we get $= \frac{g_0}{3}$. In other words, when one third of the initial gap distance is reached, the pull-in sets in and two plates snap together. Therefore, when a parallel plate actuator with the initial gap distance of g_0 used, the maximum actuation distance achievable is $\frac{g_0}{3}$. For the pull-in voltage V_p, we substitute $z = \frac{g_0}{3}$ into equations 2.38 or 2.39. After short algebra, we get

$$V_P = \sqrt{\frac{8k{g_0}^3}{27\varepsilon_0 A}}, \text{ (eq. 2.40).}$$

This is the maximum bias voltage we can apply to the parallel plate actuator.

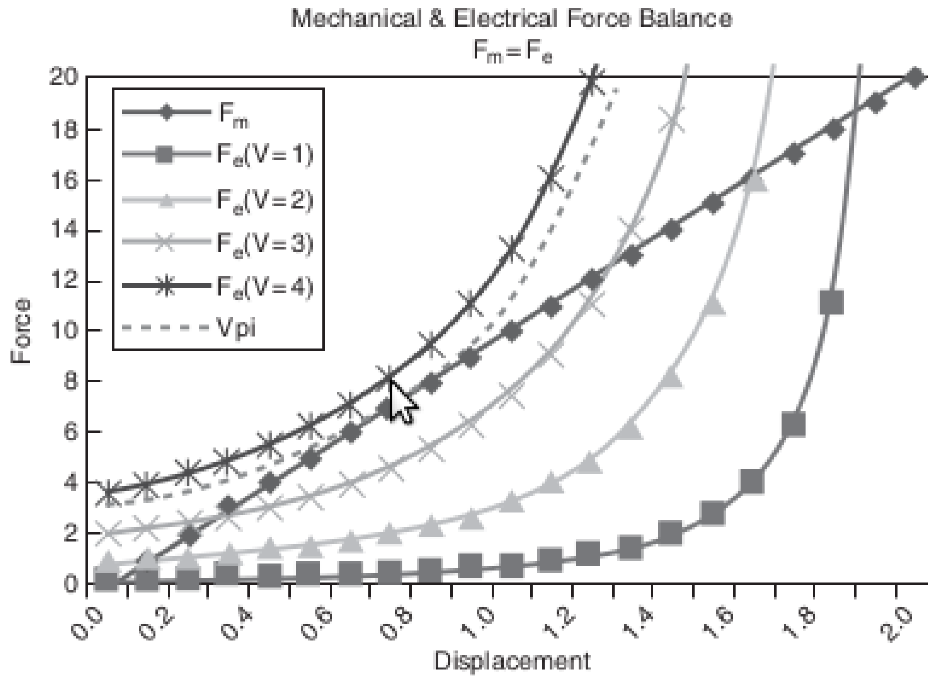

Fig. 2.6 The Graphical Solution of $F_m = F_e$. The graph of mechanical force F_m and that of electrostatic force F_e at five different bias voltage values are depicted as a function of the displacement distance of the moving plate. Below V_{pi}, two solutions of $F_m = F_e$ can be found. At V_{pi}, only one solution exists. With any bias voltage greater than V_{pi}, no solution can be found. Detailed analysis can be found in the paragraph below. The figure is taken from [27].

Now we can see why we discard the larger solution of the $F_k = F_e$ for bias voltage under the pull-in voltage V_p. From the figure 2.6, we observe that the larger gap distance is always greater than the one-third of the initial gap. At this gap distance, the pull-in already sets in, and two membranes snap to each other. Therefore, only one solution of $F_k = F_e$ is meaningful as the gap distance of the parallel plate actuator.

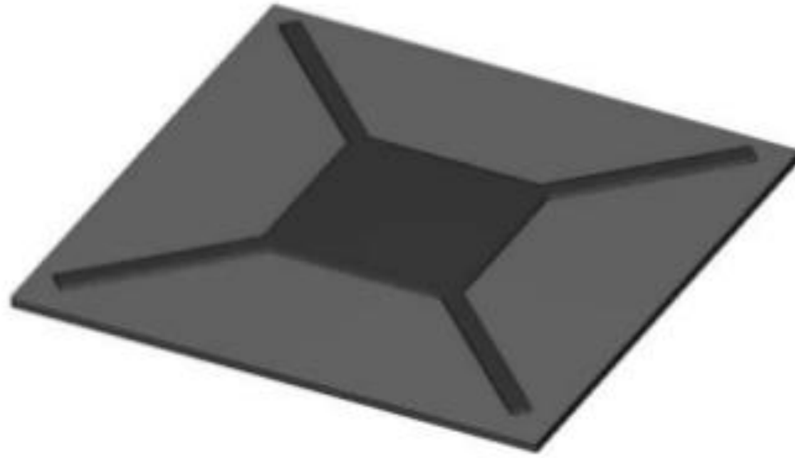

Fig. 2.7 A Parallel Plate Actuator with X-beam Structure. Four beams attached at each corner of the plate act as bar springs and exert a restorative force and balance the electrostatic attractive force. The figure is taken from [27]

In figure 2.7 is a simplified sketch of our FPI design. To tune the device, the top membrane is fabricated to move, by supporting it at four corners with beam springs (X-beam). The beam spring in our design satisfies a 'fixed-guided' boundary condition, where far end of the beam is held fixed so that its displacement and the slope cannot be changed by any applied force ('fixed'). The other end where the beam is attached to the membrane in the middle at its corner is free to move, but the slope is fixed to match that of the membrane ('guided'). An expression for the pull-in voltage V_p is followed. The spring constant k for the fixed-guided beam spring is given by [27]

$$k = \frac{Ewt^3}{l^3} \qquad \text{(eq. 2.41)}$$

where w, t, and l are the width, thickness, and length of the beam, respectively. E is the Young's modulus, a quantity that indicates how stiff the material is. The X-beam structure is analogous to the membrane with four springs attached in parallel. The spring constants add up when the springs are attached in parallel. The total spring constant for the entire structure is, therefore, $4k = \frac{4Ewt^3}{l^3}$. By substituting this expression into equation 2.40, we finally have

$$V_P = \sqrt{\frac{32{g_0}^3}{27\varepsilon_0 A}\frac{Ewt^3}{l^3}} \qquad \text{(eq. 2.42)}$$

Again, this is the maximum bias voltage we need to deflect the top membrane to the maximum actuation distance of $\frac{g_0}{3}$. The pull-in voltage V_p is proportional to the initial gap distance ($\sim {g_0}^{\frac{3}{2}}$), the area of capacitor A ($\sim A^{\frac{1}{2}}$), the Young's modulus of the beam spring material ($\sim E^{\frac{1}{2}}$), the width ($\sim w^{\frac{1}{2}}$) and the thickness ($\sim t^{\frac{3}{2}}$) of the beam spring, and inversely proportional to the length of the beam spring ($\sim l^{\frac{-3}{2}}$).

Mathematical Derivation I: Derivation of $h = \frac{2n_1 d cos\theta_{iII}}{2}$

Consider the optical path-length difference L between two beams, one reflected on the front surface of a parallel dielectric medium and the other on the back surface. They are denoted as E_{1r} and E_{2r} in figure M1, respectively. The index of refraction of the incident medium is n_1 and that of the dielectric n_f. The thickness of the dielectric medium is d. From figure M1, $n_f(\overline{AB} + \overline{BC}) + n_1\overline{AD}$. Since$\overline{AB} = \overline{BC} = \frac{d}{cos\theta_t} = \frac{2n_f d}{cos\theta_t} - n_1\overline{AD}$. Now $\overline{AD} = \overline{AC}sin\theta_i = \overline{AC}\frac{n_f}{n_1}sin\theta_t$, where Snell's law is used in the last step. But $\overline{AC} = 2dtan\theta_t$, and $L = \frac{2n_f d}{cos\theta_t}(1 - sin^2\theta_t) = 2n_f dcos\theta_t$.

Comparing L with h in figure 2.2, we can easily see that $h = \frac{L}{2}$. With the notation used in figure 2.2, therefore, $h = \frac{2n_1 dcos\theta_{iII}}{2}$.

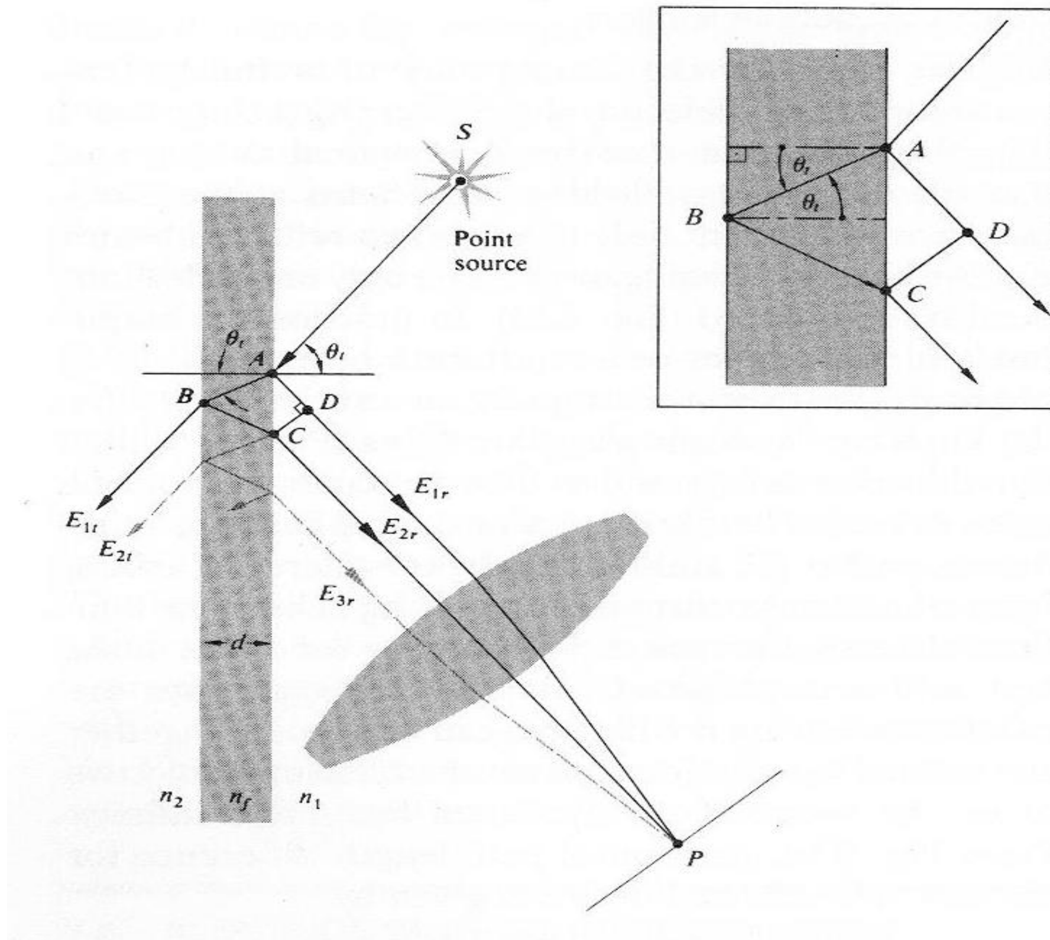

Fig. M1 An optical path difference between two lights emanate from the boundary.

Figure from [18]

Mathematical Derivation II: Derivation of the characteristic matrix for TM wave

Referring to figure 2.2, for the p-wave or TM wave we need to switch every E and H pair first (so that its magnetic field H is transverse to the plane of incidence), and then reverse the direction of H from into the paper to out of it (so that we have the correct direction of EM wave propagation). As before, three different materials have the indices of refraction, n_0, n_1, and n_s, respectively. A p-wave is impinging from medium 1 onto medium 2. There occur reflection and transmission of the incident EM wave on the first boundary. The transmitted part of the p-wave reflects and transmits once more when it hits the second boundary. As seen in figure 2.1, there are multiple beams from successive reflections and transmissions at each boundary. However, all waves in the same direction are added up and represented by E_{rI}, E_{tI}, E_{rII}, and E_{tII}. From the Maxwell's equations, we have the following boundary conditions. At boundary I,

$$E_I = (E_{iI} - E_{rI})cos\theta_{iI} = (E_{tI} - E'_{rII})cos\theta_{iII} \qquad \text{(eq. M1)}$$

and

$$H_I = \sqrt{\frac{\varepsilon_0}{\mu_0}}n_0(E_{iI} + E_{rI}) = \sqrt{\frac{\varepsilon_0}{\mu_0}}n_1\left(E_{tI} + E'_{rII}\right) \qquad \text{(eq. M2)}$$

where we use one of the consequences of the Maxwell's equations that in non-magnetic medium E and H are related by: $\vec{H} = \sqrt{\frac{\varepsilon_0}{\mu_0}}n\hat{k} \times \vec{E}$.

At boundary II,

$$E_{II} = (E_{iII} - E_{rII})cos\theta_{iII} = E_{tII}cos\theta_{tII} \qquad \text{(eq. M3)}$$

and

$$H_{II} = \sqrt{\frac{\varepsilon_0}{\mu_0}} n_1 (E_{iII} + E_{rII}) = \sqrt{\frac{\varepsilon_0}{\mu_0}} n_s E_{tI} \qquad \text{(eq. M4)}$$

To account for the phase shift that the p-wave experiences as it traverses through the medium 2, we define $h = \frac{2n_1 d cos\theta_{iII}}{2}$. (See Mathematical Derivation I for the derivation of this result.) Then we have $E_{iII} = E_{tI} e^{-ik_0 h}$, and $E_{rII} = E'_{rII} e^{ik_0 h}$. With these equations, now we can rewrite equations M3 and M4 as

$$E_{II} = \left(E_{tI} e^{-ik_0 h} - E'_{rII} e^{ik_0 h}\right) cos\theta_{iII} \qquad \text{(eq. M5)}$$

and

$$H_{II} = \sqrt{\frac{\varepsilon_0}{\mu_0}} n_1 \left(E_{tI} e^{-ik_0 h} + E'_{rII} e^{ik_0 h}\right) \qquad \text{(eq. M6)}$$

Solving equations M5 and M6 for E_{tI} and E'_{rII} and substituting them into equations M1 and M2 yields

$$E_I = E_{II} cos k_0 h + \frac{H_{II} i sin k_0 h}{Y_1} \qquad \text{(eq. M7)}$$

and

$$H_I = E_{II} Y_1 i sin k_0 h + H_{II} cos k_0 h \qquad \text{(eq. M8)}$$

where $Y_1 = \sqrt{\frac{\varepsilon_0}{\mu_0}} \frac{n_1}{cos\theta_{iII}}$.

The system of linear equations M7 and M8 can be rewritten into a single matrix equation,

$$\begin{bmatrix} E_I \\ H_I \end{bmatrix} = m_1 \begin{bmatrix} E_{II} \\ H_{II} \end{bmatrix},$$

where the m_1, the characteristic matrix that relates E and H fields at a boundary, is given by

$$m_1 = \begin{bmatrix} cosk_0h & \frac{isink_0h}{Y_1} \\ Y_1isink_0h & cosk_0h \end{bmatrix} \qquad \text{(eq. M9)}$$

CHAPTER 3. IMPLEMENTATION OF THE FPI FILTER

With the relevant theoretical background reviewed in the previous chapter, we start the design of our FPI filter. In our current project, we are developing an optical filter in long wavelength infrared range (LWIR: λ = 8-11 μm), which will be integrated with broad band mercury cadmium telluride (HgCdTe, MCT) detector and complementary metal-oxide-semiconductor (CMOS) control circuitry into a low-cost, miniaturized LWIR spectrometer that can reliably detect the improvised explosive devices in the battle field using the presence and concentration of various gases in the environment.

In more traditional spectrometer, a dispersive medium such as a prism or an optical grating is used to generate a spectrum of light that is continuously distributed by its wavelength. However, dispersive spectrometer tends to be bulk in size, and not suitable for a compact spectrometer. An attractive alternative is an interferometer-based spectrometer where the light passing through the optical cavity of the spectrometer interacts with itself to generate the spectrum of light. A famous experiment by Michelson and Morley is one example of the application of interferometer-based spectrometry. In their experiment, a beam of light is split into two perpendicular beams at a partially transmitted mirror. Two beams then travel to the fully reflected mirror a certain distance away and back to where they are split. They are combined to interfere there, thus reveal the difference two beams experience along their individual path from the split to the way back to the partially transmitted mirror. In original Michelson and Morley experiment, they tried to see the difference

the light experiences as it travels along and perpendicular to the ‘luminiferous aether’, a theoretical medium on which the light wave travels on. The experiment found no evidence of the difference, and this null result in turn contributed greatly to Einstein’s special theory of relativity.

To implement the required optical filter, we chose a MEMS-based Fabry-Perot interferometer (FPI) as a base structure. As discussed in the previous chapter, the structure of the FPI is basically two partially transmitted mirrors facing each other in parallel with some distance between them. The gap distance determines the wavelength of the light that passes through the FPI. A dielectric mirror, called a distributed Bragg reflector (DBR), is used to implement the necessary mirrors. The DBR comprises of a number of stacks of alternating layers of materials with high and low index of refraction. To tune the filtering wavelength of the device, we need a mean to change the gap distance between two mirrors. One of the membranes on which the mirror is constructed is fabricated to move, by supporting it at four corners with beam springs (X-beam). A bias voltage is applied between two membranes and actuates the movable membrane with electrostatic force. The detailed design specification of our implementation is followed, with key characteristics of the fabricated device expected from the theory presented in the next chapter.

3.1 The Design of the FPI Structure

The decision to implement our optical filter with MEMS-based Fabry-Perot interferometer is followed by the detailed discussion of how to realize the device from the scratch. The first issue to discuss was the substrate on which the filter is

fabricated. One possibility utilized commonly in the MEMS device fabrication is called the surface micromachining. In the surface micromachining, the device structure is fabricated monolithically on the substrate surface with many steps of deposition, lithography, and etching. With cutting edge technology, more than 30-40 layers is constructed routinely. Some of the fabricated layers can be sacrificial layers that are partially etched out and thus release a structure so that it can be moved to accommodate the actuation of the device. The complexity of the envisioned fabrication process and most of all the difficulty with implementing the mirror needed in the FPI filter in the surface micromachining exclude the possibility of the monolithic fabrication with the surface micromachining. Instead, we decided to fabricate two membranes separately on a Silicon on Insulator (SOI) wafer, and bond them together to form the final FPI filter.

As the name indicates, the SOI wafer has three different material layers stack on top of each other. The top active layer is called a 'device layer'. It is made from high quality semiconductor material, and this is where the semiconductor device structure is fabricated. Under the device layer is a 'buried oxide' or BOX layer, a thin silicon dioxide layer that isolates and electrically insulates the device layer from the bulk 'handle' wafer, a thick layer that physically supports the wafer. A variety of device and BOX layer and handle wafer thickness is available, off the shelf most of the time, from many vendors nowadays. Originally developed to improve the performance of CMOS device, SOI wafers found many applications in MEMS fabrication because it can provide process solutions that is very difficult or impossible

with more traditional silicon wafers. There are two different ways to fabricate an SOI wafers: Bonded and Etchback SOI (EBSOI) and Separation by Implantation of Oxygen (SIMOX).

Early SOI is produced with EBSOI method. In EBSOI, two starting wafers undergo thermal oxidation to grow silicon dioxide (thermal oxide) layers. When in the furnace, oxide will grow on all sides of the wafer. Once the oxide layer is sufficiently thick, the wafers are bonded together at the oxide layer. The atomic structure of silicon dioxide allows the wafers to partially bond at room temperature by simply applying a physical force, but they are baked at about 1100°C to solidify the bonds. This bonded oxide film becomes the BOX layer. After bonding, the wafers undergo chemical mechanical polishing (CMP) or etching in order to remove the majority of one of the substrates, leaving just a thin layer of silicon above the silicon dioxide film. This is how the device layer of the SOI wafer is formed. Because of the CMP or other wafer grinding process, the BESOI can generally be used to produce the SOI with thicker (> 2μm) device layer. The SIMOX is preferred fabrication method over the EBSOI due to its ability to precisely control the thickness of the device and BOX layers. To produce the SIMOX SOI wafer, large quantity of oxygen ions is implanted on the surface of a wafer with ion implantation process. Originally developed as improved process technique for doping semiconductors, ion implantation can be used to add any impurities to a wafer. The energy used to implant the oxygen ions determines the depth and the thickness of the BOX layer, as well as the subsequent device layer. After implanting the oxide layer, the wafer is

baked for several hours at ~1300°C to solidify the oxide layer and produces a uniform BOX layer throughout the entire wafer.

By using SOI wafer as a substrate to fabricate our device, we expect a significant simplification in the entire fabrication process. Two chips are cut from the SOI wafer. The device layer on each of two chips is used to form a membrane where the DBR mirror is constructed. To construct the membrane, the handle wafer is patterned and etched through using bulk micromachining technology. The BOX layer can work as a natural etch stopper in the through etch process. On the top membrane, the X-beam structure is fabricated with the process steps (pattern and etch) similar to those used in the backside through etch. The BOX layer is again used as an etch stopper. The bottom membrane doesn't need any process at all. Once two membranes are fabricated, the mirrors are constructed on them and two chips are bonded together to form the final FPI filter. During the design stage we envisioned four lithography masks for the entire fabrication process. The general structure of the device is given in figure 3.1. The lithography masks necessary for the fabrication process are shown in figure 3.2. The detailed process flow used in the actual fabrication of the device and the description of each step performed are provided in chapter 5.

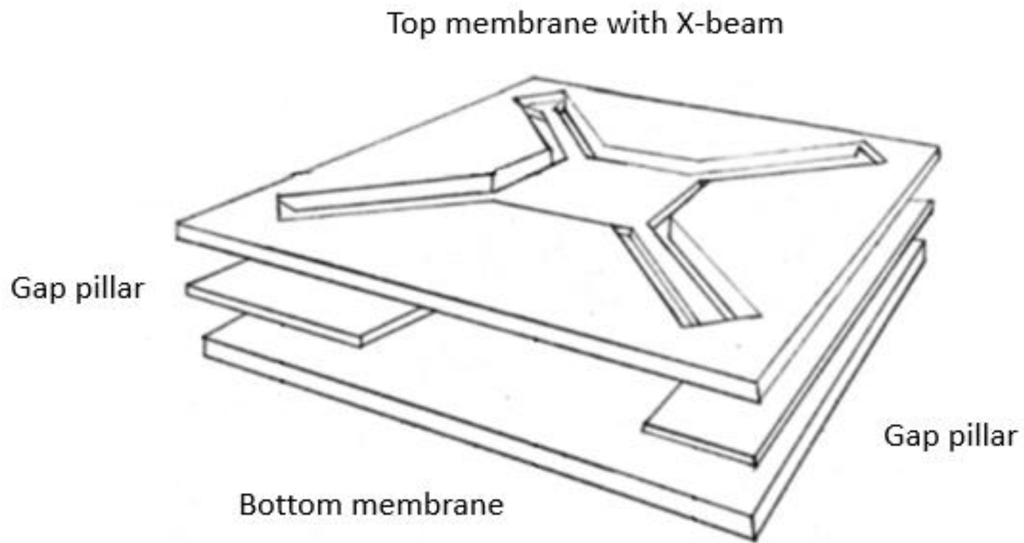

Fig. 3.1 A simplified FPI Structure. The dimension of the chip is 10 mm by 10 mm in a square shape. The optically active area is 2 mm by 2 mm in the middle of the chip, offset by 1 mm from one side of the chip to place bond pad at the edge to apply a bias voltage for electrostatic actuation. The final dimension of the beam spring is chosen to be l = 2.12 mm, w = 0.15 mm, and t = 25 µm, for length, width, and thickness, respectively. The initial gap distance is defined with the gap pillars and determined to be g_0 = 25 µm.

a) Masks for device layer and handle wafer side on top membrane

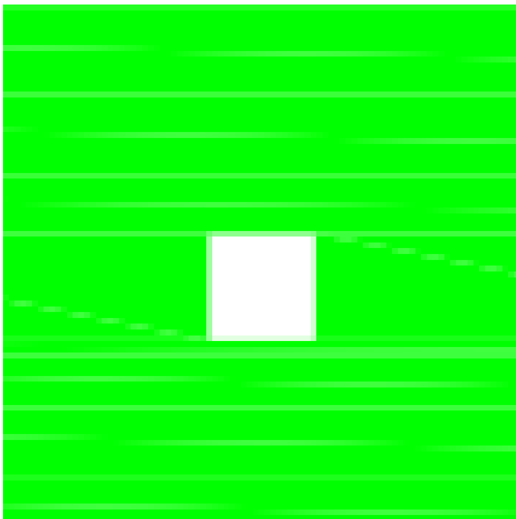
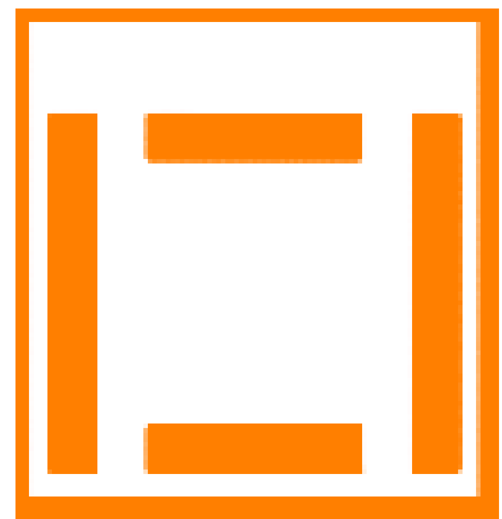

b) Masks for handle wafer side on bottom membrane and the gap pillar

Fig. 3.2 The Lithography Masks for the FPI Filter. The device layer on the bottom membrane doesn't need any process, and no mask is necessary. The bottom membrane handle wafer mask is used for the shadow mask of mirror deposition as well.

The physical dimension of the FPI filter is discussed. The overall size of the chip and the optically active area in the middle of the chip were dictated by the collaboration. Since the FPI filter is used in front of the MCT IR detector, its size needed to accommodate the physical size of the detector. As a result, the dimension of the chip is determined to be 10 mm by 10 mm in a square shape, and the optically active area is 2 mm by 2 mm in the middle of the chip in a square shape as well, offset by 1 mm from one side of the chip to place bond pad at the edge to apply a bias voltage for electrostatic actuation. The dimension of the beam spring is chosen to accommodate an adequate bias voltage. The detailed calculation is provided in section 4.2, where we discussed the simulation of electrostatic actuation of our FPI filter. The final dimension of the beam spring is given by l = 2.12 mm, w = 0.15 mm, and t = 25 μm, for length, width, and thickness, respectively. The thickness of the device layer of the SOI wafer used in the fabrication process determined the thickness of the membrane and the thickness of four X-beam springs. The gap distance should accommodate the tuning of the specified operational spectrum of 8-11 μm. Half the wavelength of the passing EM wave is the gap distance between two mirrors, thus we need 5.5 μm space between the mirrors. After adding the thickness of two mirrors on the top and bottom membranes (See next section for the discussion of the DBR mirror), the initial gap distance is finalized to be g_0 = 25 μm, and this distance is defined with four gap pillars fabricated on the device layer of the bottom membrane.

3.2 The Design of the DBR mirror

The FPI comprises of two mirrors facing each other in parallel. As discussed in previous chapter, metallic mirror cannot be used in the infrared region for its high absorption in the region. The mirror we use in the design of our FPI is a DBR mirror, a dielectric mirror made of a certain number of stacks of alternating layers of two materials with high and low index of refractions. Two considerations needed to go into the DBR design: the DBR materials and the fabrication method. The fabrication method is discussed first.

The thin film deposition has been developed for a long time in various fields of applications and matured enough to deposit a layer of material of single atomic constituent. As such, we will use thin film deposition process to fabricate the DBR mirror. Thin film deposition process is largely classified into two categories: Physical Vapor Deposition (PVD) and Chemical Vapor Deposition (CVD). In CVD, starting materials called precursors are introduced in a chamber where substrate is located. A chemical reaction ensues, and the thin film is formed on the surface of the substrate. The chemical reaction can occur by themselves in low pressure environment inside a tube (Low Pressure CVD, LPCVD), or triggered by means of an electrically induced plasma in the active vapors (Plasma Enhanced CVD, PECVD). In general, CVD produces better quality thin film. However, the need for the suitable chemical reaction and precursors, and the necessity of the complicated reaction chamber, we will use more flexible PVD for our mirror deposition.

In PVD, the target material to be deposited, called an evaporant, is heated to vaporize in a vacuum, the resulting vapor molecules travel to everywhere in line of sight and condenses into a solid film on the substrate, which is kept below the freezing temperature of the evaporant. Compare to CVD, PVD is more widely adapted in thin film deposition because it is simpler to implement in principle, has much more available targets and more flexible equipment design to accommodate different substrate geometry. Three different ways to induce the evaporation of the target further divide the PVD into three different techniques: 1. Thermal PVD where the target is simply heated up in a crucible to vaporize, 2. Electron Beam PVD (EBPVD) where an electron beam is used to produce the target vapor, and 3. Sputtering where energetic ions are produced to bombard on the target so that an atom or molecule of target is ejected from it. Mostly because of the equipment availability, we decided to use the EBPVD for our DBR deposition. The details of deposition process are given in chapter 5, where we describe the entire fabrication process.

The target materials for the mirror deposition are considered at the same time as the deposition method. Many categories of materials can be used for optical thin film in the IR region. The oxide and fluoride compounds, single element and compound semiconductors, and transparent conductors including some metals are some of the examples. The candidate materials used for the DBR mirror must allow high transmission in the operational wavelength regions of the mirror. A distinct division in usable IR materials occurs near wavelengths between the Mid-Wave IR

(MWIR) and LWIR. Oxide compounds such as aluminum oxide (Al_2O_3), chromium oxide (Cr_2O_3), hafnium dioxide (HfO_2), indium oxide (In_2O_3), indium-tin oxide (ITO), niobium pentoxide (Nb_2O_5), praseodymium oxide (Pr_2O_3), scandium oxide (Sc_2O_3), silicon dioxide (SiO_2), silicon monoxide (SiO), tantalum pentoxide (Ta_2O_5), titanium dioxide (TiO_2), yttrium oxide (Y_2O_3), and zirconium oxide (ZrO_2) are transparent at wavelengths shorter than about 7 µm. There, oxide compound materials provide the low- ($n < 1.6$, SiO_2), medium- ($1.6 < n < 1.8$, Al_2O_3, Y_2O_3, SiO), and high- ($n > 2$, HfO_2, Sc_2O_3, Ta_2O_5, Nb_2O_5, TiO_2) refractive indices required in the design of the DBR. Many optical thin films in the MWIR region can be made using oxide compounds, from which durable multi-layer product including the DBR can be produced.

At wavelengths longer than about 7 µm, the corresponding available material choices are fluoride compounds including aluminum fluoride (AlF_3), calcium fluoride (CaF_2), cerium fluoride (CeF_3), lanthanum fluoride (LaF_3), magnesium fluoride (MgF_3), thorium fluoride (ThF_4), and yttrium fluoride (YF_3), single element semiconductor silicon (Si) and germanium (Ge), II-VI compound semiconductor cadmium telluride (CdTe), lead telluride (PbTe), zinc sulfide (ZnS) and zinc selenide (ZnSe). As discussed in the previous chapter, the DBR performance benefits when the index contrast is large. Some DBR designs require a total number of stacks as large as 20 to 30 to achieve required reflectance of the mirror and are thus prone to high accumulated mechanical stress that threatens the physical integrity of the DBR. Fewer layers are required when the indices have a large difference in value, and this

thinner combination results in lower stress. For the combination ZnS / Fluoride, the index ratio at 10 µm wavelength is around 1.6. For the combination Ge / Fluoride, the ratio is about 3, suggesting that this combination has advantages. However, fluoride layers are not compatible with Ge surfaces due to their atomic lattice mismatch. A thin layer of a binding material must be inserted between these layers which complicates the design. The fluoride compounds have another structure issue as well. They grow with a columnar microstructure that contains a large void volume that water vapor can occupy when the thin film layer is exposed to the atmosphere. This columnar microstructure also exhibits high tensile stress, and thick fluoride layer often relieve stress to form tensile crack patterns. Simultaneously, water vapor can permeate the film void volume and change optical properties and adhesion strength. The ZnS and Ge surfaces are compatible and produce a desirable index ratio of about 1.8. Many IR designs are based on this latter combination of materials, with outer layers requiring a fluoride as an antireflection (AR) layer to minimize the reflection and thus maximize the performance of the device.

The material commonly used for low-index components for MWIR to LWIR film deposition are zinc sulfide (ZnS) and zinc selenide (ZnSe). They sublime and dissociate when evaporated. The starting materials are produced in a CVD process from the reaction of gases. The condensed solids are crushed and sized or pressed into desired working shapes. If substrate surface and chamber atmosphere conditions are favorable, the dissociated components will recombine with correct chemical composition at the substrate and produce non-absorbing dense films. While e-beam

is a useable evaporation technique, a heated baffled box source is preferred because in the nearly isothermal evaporation environment created, there are fewer hot spots that can produce unrecoverable composition deviations. The zinc selenide vapor is known to be toxic and health hazard, and special disposal scheme is necessary.

The high-index component of a LWIR multilayer AR, bandpass, or edge filter is usually germanium (Ge), with index n of about 4, and is evaporated with EBPVD. Procedure to obtain non-absorbing films includes the elimination of oxygen and operation at a deposition rate and a substrate temperature that prevents the formation of an oxide. Silicon (Si) can be used for SWIR films, but it is difficult to avoid the formation of a silicon oxide whose evaporation temperature is much higher than that of the metal, and consequently produces spatter.

After exhaustive literature search related the IR thin film coating, we decided to use germanium (Ge) and zinc sulfide (ZnS) for high and low index materials, respectively. Before we determined the detailed design specification of the DBR using Ge and ZnS. The indexes of refraction for Ge and ZnS are scrutinized. One of the design requirements of our FPI filter is its tunability. The device should operate on the wavelength spectrum of 8-11 μm. The DBR should maintain a high reflectance throughout the spectrum. Since the high index contrast is necessary for the high reflectance of the mirror, it can be achieved when the index of refraction for each material remains as constant as possible. The graphs of index of refraction for germanium and zinc sulfide in the operation wavelength spectrum range are given in figure 3.3. They do not remain constant in 8-11 μm wavelength range. However, the

relative change in their value is very small (0.003/4 < 0.1% for Ge, and 0.04/2.21 < 2% for ZnS), and so is the variation in the index contrast (< 2%).

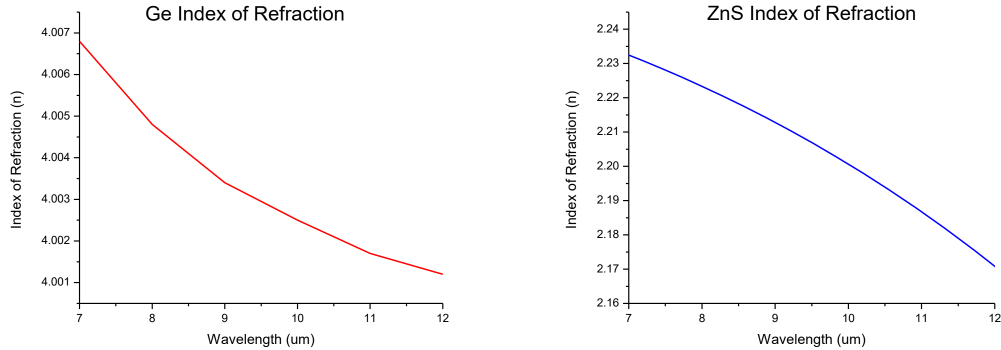

Fig. 3.3 The Index of Refraction for Ge and ZnS [14, 20, 26].

Now is the good time to discuss the design wavelength of the DBR. As discussed in chapter 2, the DBR is designed at a single wavelength of the light. Our mandate of 8-11 μm wavelength operation spectrum contradicts the single DBR design wavelength condition. The way to resolve this issue is to pick one wavelength that represents the entire operation spectrum. An average of the value at the boundaries of the region would be most natural choice. However, it is customary to use the frequency instead of length in such calculation. This is from the fact that the harmonics of a certain wave are integer multiples of the fundamental when expressed in frequency. Therefore, they are separated by equal distance in frequency domain. On the other hand, if wavelength is used, the fundamental and the high harmonics exhibit the harmonic progression ($\frac{1}{n}$ for n = 1, 2, 3, …) and bunched up as n increases. Since for any EM wave the frequency f and wavelength λ are related by $= f \cdot \lambda$, where c = $3\text{x}10^8$ m/s is the speed of light in vacuum, for the operation spectrum

of [λ_L, λ_H], the design wavelength λc is given by $\frac{1}{\lambda c} = \frac{1}{2}\left(\frac{1}{\lambda L} + \frac{1}{\lambda H}\right)$. Using the values at the boundaries of our spectrum range of [λ_L, λ_H] = 8-11 µm and the equation for λc, the value of our design wavelength is found to be λc = 9.264 µm.

With the design wavelength determined, the thickness of quarter wave layer should be straight forward. However, there are another consideration to be made. The wavelength of the EM wave is dependent on the medium it travels, while the frequency remains the same as the light exits from one medium and enters the other. When a wavelength of light is mentioned without any reference to the medium it travels, it is assumed to be in vacuum. The change in wavelength of the light without corresponding change in frequency results in a change of speed of light as it traverses between different media. This difference in the speed of light is the physical mechanism that causes the refraction of light. The index of refraction of some material is the ratio of the speed of light in the vacuum and that material ($n = \frac{c}{v}$). Since speed of wave is the product of its frequency and wavelength and the frequency remains constant as light progress through different media, we can express the index of refraction as the ratio of the wavelength in the vacuum and the medium ($n = \frac{\lambda_{vacuum}}{\lambda_{medium}}$). The concept of Optical Path Length (OPL) is relevant. Contrast to the Geometric Path Length (GPL), which is simply a physical length measured with a ruler, the OPL is the length a light needs to travel through a material to cover the same phase change as it experiences while it travels in the GPL in vacuum. For example, a light of 1 m wavelength experiences a phase change of 2π while it travels

1 m in vacuum. However, it only needs to advance 1/1.333 = 0.75 m to produce 2π phase shift when it travels through water (n = 1.333). In other words, the GPL of 0.75 m in water corresponds to the optical path length of 1 m. The OPL is given by $OPL = n \cdot GPL$, where n is the index of refraction of the medium in question. Once OPL is obtained from different materials, we can compare the light travels through them on the equal footing.

The name 'quarter wave stacks' refers to the OPL of the layer. To determine the physical thickness of each layer in the DBR, therefore, we need to find the GPL of the Ge and ZnS layers. The OPL is quarter of the design wavelength ($OPL = \frac{\lambda_c}{4} = \frac{9.264}{4} = 2.316\ \mu m$). At the design wavelength of 9.264 µm, the indexes of refraction are $n_{Ge} = 4.00$ and $n_{ZnS} = 2.21$ for Ge and ZnS, respectively. The GPL, that is the necessary thickness of each layer, are 2.316/4.00 = 0.579 µm and 2.316/2.21 = 1.048 µm for germanium and zinc sulfide, respectively. The single stack of high and low index double layers is then 0.519 + 1.048 = 1.567 µm.

Finally, we find the number of double layer stacks we need for the necessary for greater than 95% of the DBR reflectance. The expression for the reflectance of the N stacks DBR is given in equation 2.29 ($R_N = \left[\frac{{n_1}^{2N} - \left(\frac{n_0}{n_s}\right){n_2}^{2N}}{{n_1}^{2N} + \left(\frac{n_0}{n_s}\right){n_2}^{2N}}\right]^2$). With $n_0 = 1$ and $n_s = 3.415$ (use silicon as substrate, n = 3.415 at λc = 9.264 µm), we can simplify the reflectance as $R_N = \left[\frac{1 - \left(\frac{n_0}{n_s}\right)\left(\frac{n_2}{n_1}\right)^{2N}}{1 + \left(\frac{n_0}{n_s}\right)\left(\frac{n_2}{n_1}\right)^{2N}}\right]^2$. With this simplified equation for R_N and the index contrast of 4.00/2.21 = 1.81, we found R_N = 94% for when N = 4 and 98% with

N = 5. Therefore, we determined that five stacks of Ge/ZnS double layers are necessary for greater than 95% reflectance of the DBR. The bandwidth of the DBR can be found with equation 2.35 ($\frac{\Delta\lambda}{\lambda} = \frac{4}{\pi} sin^{-1} \frac{n_H - n_L}{n_H + n_L} = \frac{4}{\pi} sin^{-1} \frac{\frac{n_H}{n_L} - 1}{\frac{n_H}{n_L} + 1}$). With $\frac{n_H}{n_L} = 1.81$, we have $\Delta\lambda = \lambda \frac{4}{\pi} sin^{-1} \frac{\frac{n_H}{n_L} - 1}{\frac{n_H}{n_L} + 1} = 9.264 \cdot \frac{4}{\pi} \cdot sin^{-1} \frac{0.81}{2.81} = 3.448\ \mu m$. Therefore, the DBR maintains high reflectance from 7.540 to 10.988 μm, a range very close to the required operation spectrum of λ = 8-11 μm.

In this section, we identified zinc sulfide (ZnS) as low index material and germanium (Ge) as high index material for the DBR components, with n = 2.21 and 4.00 at the mirror design wavelength λ_C = 9.264 μm, respectively. At the same time, given the index contrast of 4.00/2.21 = 1.81, we decided to use five stacks of Ge/ZnS double layers to ensure the DBR mirror reflectance of better than 95% at the DBR mirror design frequency. This index contrast provides an adequate bandwidth of Δλ = 3.448 μm that covers the required operation spectrum of λ = 8-11 μm well.

CHAPTER 4. THE SIMULATION OF THE FPI FILTER

A computer-aided simulation study of any kind of device before actual fabrication is financially prudent and therefore well-established practice in many engineering disciplines. With the design parameters we determined in the previous chapter, the expected performances of three subsystems of the FPI filter are studied with computer-aided simulation. They are:

1. The performance of the DBR reflectance in the 8-11 μm wavelength range,
2. The tuning performance of the FPI filter using an electrostatic actuation, and
3. The desired filtering performance of the FPI filter while the passing wavelength is tuned with applied DC bias.

The results of these simulation studies are presented in the following three sections.

4.1 The Reflectance of the DBR Mirror

In the previous chapter, we identified zinc sulfide (ZnS) as low index material and germanium (Ge) as high index material with n = 2.21 and 4.00 at the DBR mirror design frequency $\lambda_C = 9.264$ μm, respectively. At the same time, given the index contrast of 4.00/2.21 = 1.81, we decided to use five stacks of Ge/ZnS double layers to ensure the DBR mirror reflectance of better than 95% at the DBR mirror design frequency.

We used the optical transfer matrix formalism reviewed in chapter 2 to find the reflectance of the DBR mirror in the 8-11 μm wavelength range. In this formalism, the electric and magnetic field on each layer of thin film is represented by

2x2 matrix $m_i = \begin{bmatrix} cosk_0h & \frac{isink_0h}{Y_i} \\ Y_iisink_0h & cosk_0h \end{bmatrix}$, where $k_0h = k_0n_idcos\theta_{iI} = \frac{2\pi}{\lambda}n_idcos\theta_{iI}$,

$Y_i = \sqrt{\frac{\varepsilon_0}{\mu_0}}n_icos\theta_{iII}$ for TE or s-wave, and $Y_i = \sqrt{\frac{\varepsilon_0}{\mu_0}}\frac{n_i}{cos\theta_{iII}}$ for TM or p-wave. Here λ is the wavelength of the incident light, n_i the index of refraction of the thin film layer material, and θ_{iI} and θ_{iII} the angle of incident at the first and second boundary of the layer, respectively. See figure 2.2 for a detailed depiction and description of these optical parameters. A single stack of hi and low index material is represented by the product of two layer-matrices m_H and m_L, $m_{stack} = m_Hm_L =$

$\begin{bmatrix} cosk_0h & \frac{isink_0h}{Y_H} \\ Y_Hisink_0h & cosk_0h \end{bmatrix}\begin{bmatrix} cosk_0h & \frac{isink_0h}{Y_L} \\ Y_Lisink_0h & cosk_0h \end{bmatrix}$, and finally the DBR mirror with n number of stacks is written as a product of itself, $m_{DBR} = {m_{stack}}^N$. Once we find the m_{DBR}, we can use the expression for the reflectivity from chapter 2 ($r = \frac{Y_0m_{11}+Y_0Y_{n+1}m_{12}-m_{21}-Y_{n+1}m_{22}}{Y_0m_{11}+Y_0Y_{n+1}m_{12}+m_{21}+Y_{n+1}m_{22}}$, equation 2.27) to calculate the reflectance of the DBR. Here m_{ij}'s are the i,j-components of the DBR matrix, and Y_0 and Y_{n+1} are Y_i for the incident and substrate material or the DBR, respectively. The reflectance of TE and TM waves are calculated separately, and the average is taken and presented as a single reflectance value for a specific simulation condition.

The optical parameters in the expression for the reflectance are the index of reflection for each material, the incident angle on each boundary, the thickness of each layer, and the wavelength of incident EM-wave. Among them, the wavelength is the variable in the simulation, since we wish to obtain the reflectance of the DBR mirror with respect to the wavelength of the incident light. The choice of germanium

(Ge) and zinc sulfide (ZnS) as high and low index layer materials fixes the thickness of each layer. More specifically, the layer thickness is the quarter wave length in the material. They are then $\frac{1}{4}\frac{9.264}{4.00} = 0.579\mu m$ for germanium and $\frac{1}{4}\frac{9.264}{2.21} = 1.048\mu m$ for zinc sulfide. To simplify the calculation, normal incident of light is assumed throughout the simulation ($\theta_i = 0$ for all boundaries). Some consideration must be taken for the index of refraction n. As indicated in previous chapter, the index of refraction is also a function of wavelength. Even though their variation in value is relatively small ($< 0.1\%$ and $< 2\%$ for Ge and ZnS, respectively), we decided to change the value of the refractive index n in the reflectance calculation as we sweep the wavelength of the incident light in our simulation.

To observe the expected improvement of the reflectance as we increase the number of stacks of the DBR, five simulation is done with the number of stacks increased from one to five. At first, we used the air as incident medium and the substrate medium. The graph of simulated performance of the DBR is given in figure 4.1. As expected, the clear improvement of the reflectance of the DBR mirror is indicated. Also observed is above 95% reflectance in 8-11 μm wavelength range as discussed in the previous chapter.

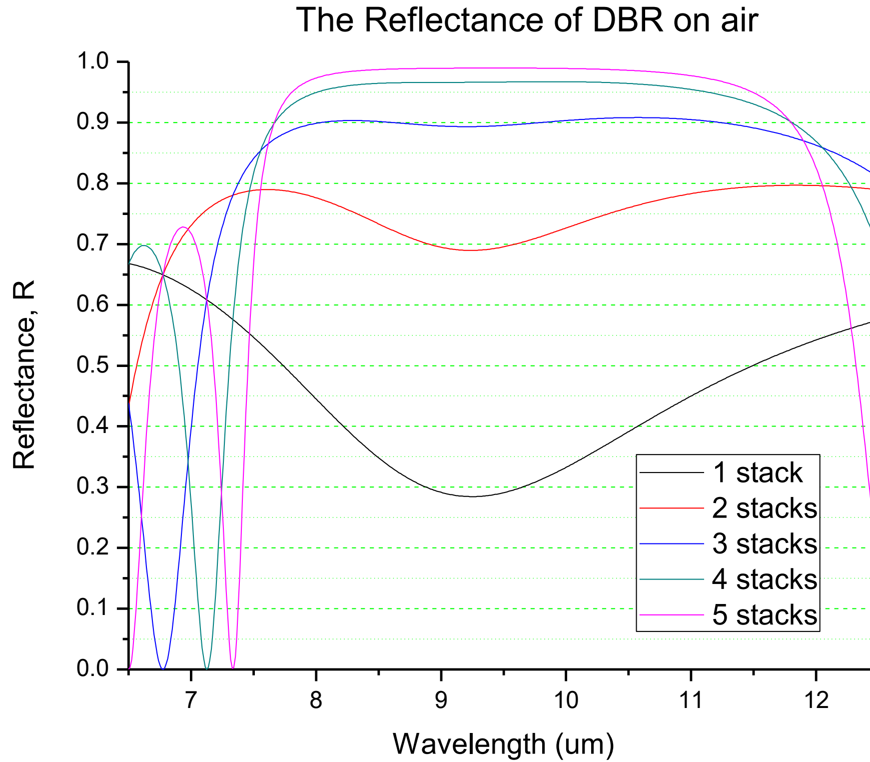

Fig. 4.1 The Reflectance of the Ge/ZnS DBR on air substrate for 1-5 stacks of double layer.

Two more simulations are performed. As described in the previous chapter, the DBR mirror will be deposited on a silicon substrate. The expression for the reflectivity (equation 2.27) contains terms with the index of refraction of the substrate material. Clearly, the substrate affects the reflectance of the DBR. Therefore, the same simulation procedure is repeated with the silicon (Si), instead of air, as the substrate on which the DBR is deposited. The result is shown in figure 4.2. The silicon substrate seems to introduce a shift in overall oscillatory behavior of the reflectance. As a result, a peak instead of a trough of oscillation is shown in the middle of the operational wavelength range. This shift enhances the reflectance in 8-

11 µm range, and the second simulation indicates that even four stacks of Ge/ZnS layer can provide our design goal of greater than 95% reflectance throughout the operational spectrum.

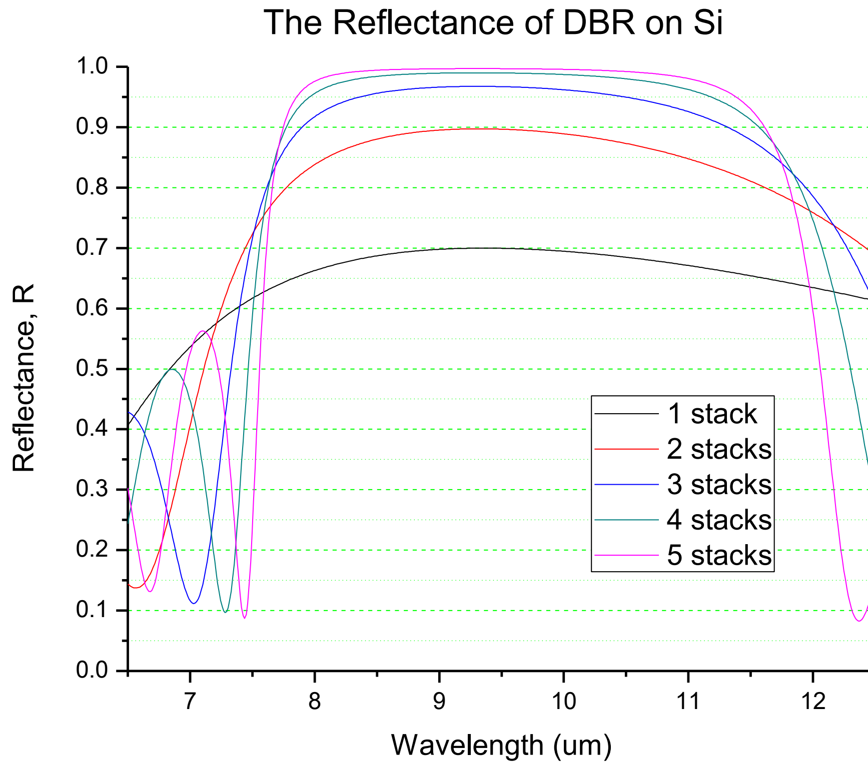

Fig. 4.2 The Reflectance of the Ge/ZnS DBR on Si substrate for 1-5 stacks of double layer.

After the simulation with Si substrate, a discussion about the role of substrate in the simulation was followed. Usually, the substrate is assumed to be thick enough so that once the light transmits into the substrate, it will lose the coherence and further optical interference can be safely ignored. The DBR in our FPI will be deposited on a very thin, 25 µm thick Si membrane. The thickness of the membrane (25µm) is only about 2~3 times thicker than the design wavelength of $\lambda c = 9.264$ µm. Therefore,

whether 25 μm thick Si membrane can be treated as a substrate made a very contentious subject of discussion. To answer this question, we decided to simulate the model with the DBR with 5 stacks of Ge/ZnS layers on top of 25 μm Si membrane. Under the Si layer, we put air as a substrate, which mimics the reality of our DBR most faithfully. The result is shown in figure 4.3. The signature interference pattern from the thin silicon layer is seen clearly as it convoluted with the reflectance of the DBR with Si substrate in figure 4.2. The periodic drops in the reflectance below 95% in the 8-11 μm spectral range was alarming, and we decided further consideration to mitigate the effect from the 25 μm Si membrane was necessary.

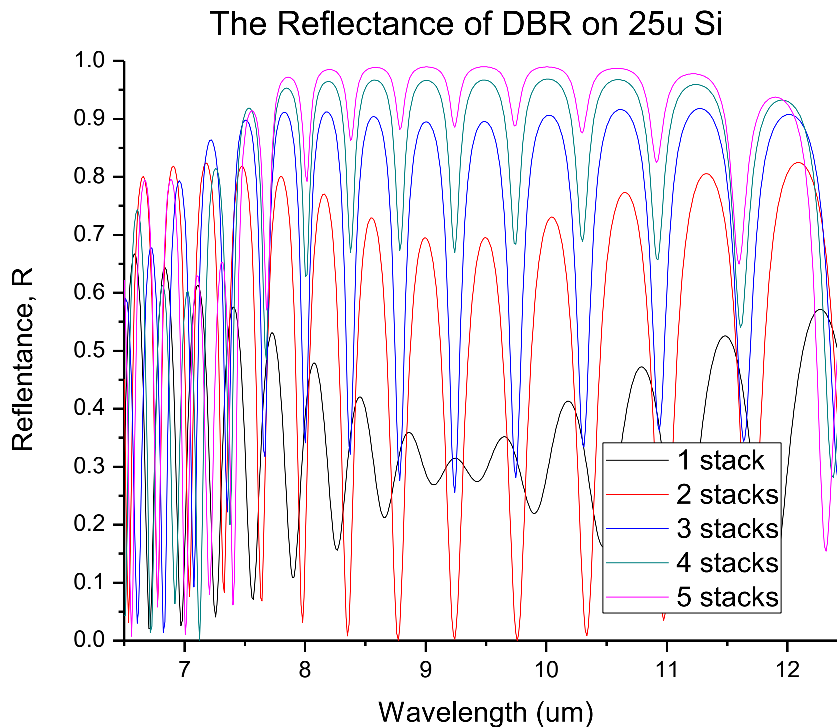

Fig. 4.3 The Reflectance of the Ge/ZnS DBR on 25 um Si membrane for 1-5 stacks of double layer.

Two possible processes are proposed to counteract the interference pattern from the thin Si membrane. Both methods are variations of an application of the anti-reflection (AR) film used in many optical devices. Most prominent example is the AR coating on lenses used in photographic cameras, or on eye glasses. To minimize the reflection from the lens surface, thin layer of film is deposited on the lens. The material and thickness of the film are chosen so that the lights reflected from the front and back surface of the film cancel each other [28].

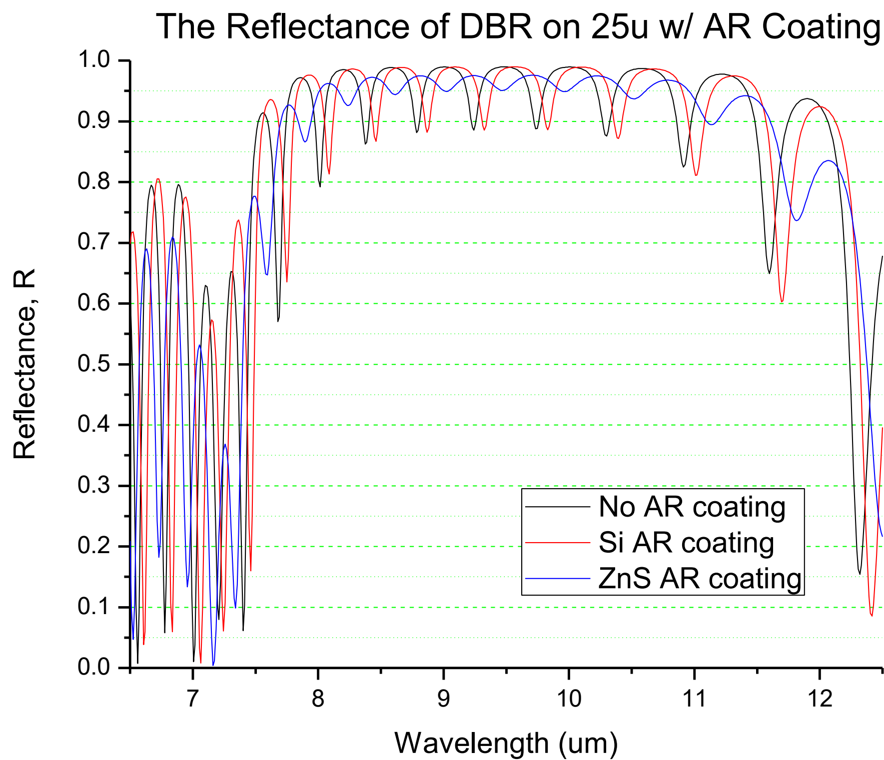

Fig. 4.4 The Reflectance of the 5 stacks Ge/ZnS DBR on 25 um Si membrane with different AR coating.

First, we considered using the Si membrane itself as the AR coating. By changing the thickness of the Si, we can make two light beams reflected from front

and back surfaces of Si interfere destructively. This scheme can be implemented by depositing more Si either on front side of the membrane before the DBR deposition or on the back side of membrane at suitable time along the fabrication process. Increasing the number of PECVD evaporants can be problematic. To maintain two evaporants of Ge and ZnS, using ZnS as AR layer is considered. By depositing a quarter wavelength of ZnS on the membrane, we can achieve the same effect as the Si AR coating. Since AR coating works only on a specific design wavelength, how it will behave in the entire operational spectrum of 8-11 μm as simulated. The reflectance of 5 stacks of Ge/ZnS layer DBR deposited on top of 25 μm Si membrane with both Si and ZnS AR coatings are simulated. The AR coating is placed on the backside of the Si membrane in the simulation. The result is given in figure 4.4. The effect of AR coating is seen to diminish as we move away from the design wavelength $\lambda c = 9.264$ μm. As a result, the periodic decrease in the reflectance persists. However, the degradation of the reflectance from the destructive interference caused by the silicon membrane is weaker with ZnS AR coating. Therefore, ZnS AR coating will be considered as a mean to improve the reflectance of the DBR mirror.

4.2 Electrostatic Actuation of the FPI with an X-beam Structure

The solution for deflection of the top plate from the initial gap distance between two plates of the parallel plate actuator in our FPI design is solved analytically and numerically. This theoretical expectation will be compared with the measurement from the fabricated device in later chapter.

4.2.1 The Analytic Solution of the FPI Actuation

The theoretical background of the electrostatic actuation of the parallel plate capacitor is reviewed in section 2.3. There, we found that the actuation of the FPI is achieved through the balancing act of the electrostatic attraction between the opposite charges accumulated on each plate ($F_e = \varepsilon \frac{A}{2} \frac{V^2}{(g_0 - z)^2}$) and the mechanical, restorative force exerted by four bar springs in a shape of X-beam ($F_k = -kz$). Here A is the overlapping area of the capacitor plates, g_0 the initial gap distance between two plates, V the applied bias voltage, z the deflection distance when the bias voltage V is applied, and ε the permittivity for the medium filling the gap. It is a product of ε_r and ε_0, where ε_r is dielectric constant or relative electrical permittivity of the medium, and $\varepsilon_0 = 8.85 \times 10^{-14}$ (F/V) the permittivity of free space. The beam spring in our design satisfies a 'fixed-guided' boundary condition, where far end of the beam is held fixed so that its displacement and the slope cannot be changed by any applied force ('fixed'). The other end where the beam is attached to the membrane in the middle at its corner is free to move, but the slope is fixed to match that of the membrane ('guided'). In section 2.3, we found the spring constant k for the fixed-guided beam spring as $k = \frac{Ewt^3}{l^3}$, (equation 2. 41), where w, t, and l are the width, thickness, and length of the beam, respectively. E is the Young's modulus, a quantity that indicates how stiff the material is. The X-beam structure is analogous to the membrane with four springs attached in parallel. The spring constants add up

when the springs are attached in parallel. The total spring constant for the entire structure is, therefore, $4k = \frac{4Ewt^3}{l^3}$.

When the beams spring is forced to deflect more than half of their thickness, the stretching restoring force F_{ms} has to be taken into account, along with the stretching effect component of the spring constant k_s, where $F_{ms} = k_s z^3$, and $k_s = \frac{\pi^4 EWt^3}{4l^3}$ [34]. With these equations, the total mechanical, restorative force is modified to $F_m = kz + k_s z^3$. However, this modification is not applied in the analytic solution to simplify the derivation of the solution. Moreover, the numerical method presented in the next section uses much more sophisticated model of the X-beam structure to find the actuation solution. Therefore, working with simpler first order approximation in analytic solution is justified.

Substituting the expression for k into F_k and solve the equation $F_e = F_k$, or $\frac{A}{2}\frac{V^2}{(g_0-z)^2} = \frac{4Ewt^3}{l^3} z$ for the deflection distance z, we find a polynomial in z of degree three. Instead of using cubic formula[1], the equation $F_k = F_e$ is solved to find the deflection distance as a function of applied bias voltage using the Matlab software. The values for each parameter found in the previous chapter are used in the simulated solution: The area of the plate A = 4 (mm^2); The permittivity of the gap medium $\varepsilon = \varepsilon_0 = 8.85 \times 10^{-14}$ (F/V) for air; The initial gap distance g_0 = 25 (μm); The dimension of the beam spring, l = 2.12 (mm), w = 0.15 (mm), and t = 25 (μm), for

[1] The solution of $ax^3 + bx^2 + cx + d = 0$ is given by $x = \{q + [q^2 + (r - p^2)^3]^{\frac{1}{2}}\}^{\frac{1}{3}} + \{q - [q^2 + (r - p^2)^3]^{\frac{1}{2}}\}^{\frac{1}{3}} + p$, where $p = -\frac{b}{3a}, q = p^3 + \frac{(bc-3ad)}{6a^2}, r = \frac{c}{3a}$.

length, width, and thickness, respectively; The Young's modulus E = 130 (GPa) for Si in the direction 45 degree to the wafer flat. The bias voltage V is increased from 0 to 130V in an increment of 10V. The graph of the result is given in figure 4.5.

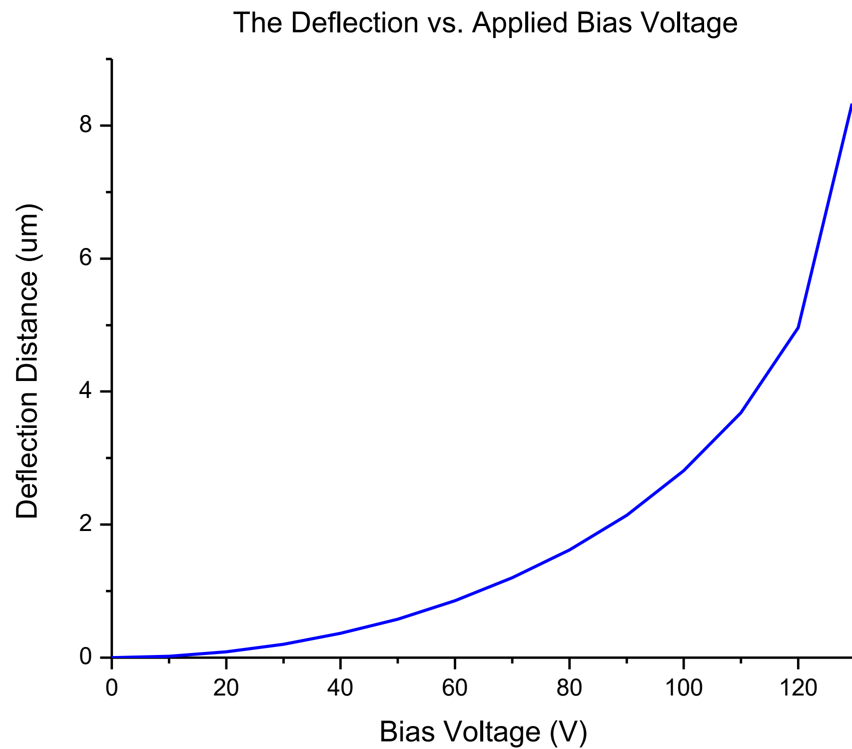

Fig. 4.5 The graph of Deflection vs. Applied Bias Voltage. The deflection distances are found analytically with various bias voltage values. A cubic relation between the deflection and the bias voltage, as well as onset of the pull-in around 130V, is demonstrated.

The graphs of the mechanical restorative force F_k and the series of attractive electrostatic force F_e with several bias voltage values are produced with the Matlab and given in figure 4.6. The same device parameter values are used to demonstrate the pull-in phenomenon discussed in the chapter 2. At lower values of bias voltage V,

the graphs of F_k and F_e gives two solutions for the gap distance as two different intersection points. The larger of these two gap distances obtained at the intersections is discarded as physically impossible solution since it is greater than the pull-in distance. The values of intersections on the graph matches well with the values obtained above by solving an equation $F_k = F_e$. As the bias voltage V increases, the graphs of F_k and F_e intersect at a single point. This is an onset of pull-in or snap-in phenomenon. This critical voltage at which the pull-in sets in is called the pull-in voltage or V_p. With bias voltage larger than V_p, there is no common intersection of F_k and F_e. Thus, no equilibrium gap distance can be obtained. In section 2.3 we found that at the onset of pull-in, the function and the first derivative the graphs of F_k and F_e intersects at a single point. With the air gap, from $F_k = F_e$ and $\frac{dF_k}{dz} = \frac{dF_e}{dz}$, we have $kz = \varepsilon_0 \frac{A}{2} \frac{V^2}{(g_0 - z)^2}$ and $k = \varepsilon_0 A \frac{V^2}{(g_0 - z)^3}$. Canceling k and solving for z, we get $= \frac{g_0}{3}$. Therefore, when a parallel plate actuator with the initial gap distance of g_0 used, the maximum actuation distance achievable is $\frac{g_0}{3}$, and any further increase of bias voltage results the pull-in and two plates snap together. For the pull-in voltage V_p, we substitute $z = \frac{g_0}{3}$ into any one of equations above and solve it for V_p. The result is $V_P = \sqrt{\frac{8kg_0{}^3}{27\varepsilon_0 A}}$. This is the maximum bias voltage we need to deflect the top membrane to the maximum actuation distance of $\frac{g_0}{3}$. With the values of parameters in our design, we have the maximum deflection distance of 8.33 μm at the pull-in voltage, V_p = 129.38 V. The maximum deflection distance and the pull-in voltage we

found here will be used as a rough guideline in fabrication and characterization process, since it is obtained through first order approximation of the electrostatic actuation system, and we don't know the exact mechanism of pull-in phenomenon.

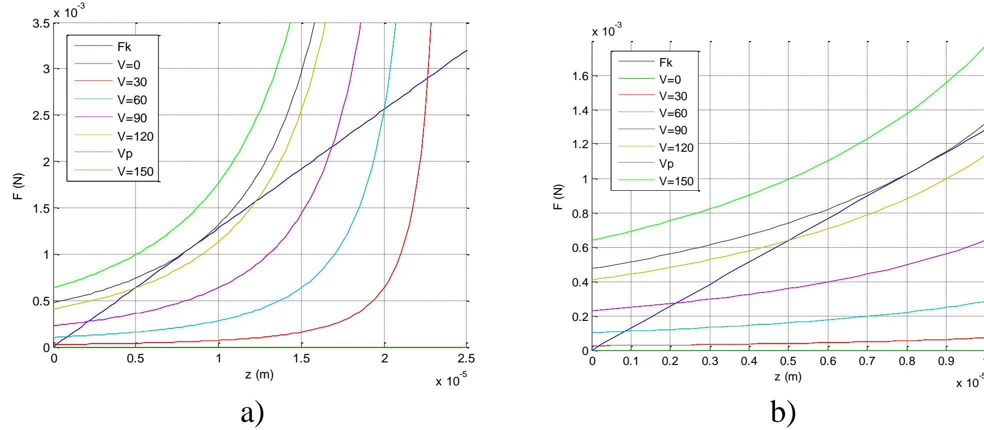

Fig. 4.6 The graphical Solution of $F_k = F_e$. a) The bias voltage V lower than V_p, two solutions are found as two intersections. The larger one is discarded on physical ground. At $V = V_p$, we have $F_k = F_e$ and $\frac{dF_k}{dz} = \frac{dF_e}{dz}$. Solving those two equations, we found z = 8.33 μm at V_p = 129.38 V for maximum deflection at the pull-in. b) Zoomed-in view of the graph. The solutions at various bias voltage (the smaller x-value of the intersection of the graphs of F_k and F_e) are found to match well with the values obtained above by analytically solving an equation $F_k = F_e$.

4.2.2 The Numerical Solution of the FPI Actuation

For numerical solution of the deflection of the X-beam, a software package 'IntelliSuite' was used. As an inception to tape-out MEMS device development package from 'IntelliSense', 'IntelliSuite' offers several different packages for the mask layout, 2D and 3D model design, and a finite element analysis and simulation of the MEMS device. Among the packages available in 'IntelliSuite', we used 'IntelliMask', '3D Builder', and 'Thermo-Electro-Mechanical Analysis' for the

device structure layouts, 3-dimensional MEMS device structure simulations, and analysis, respectively.

IntelliMask

Before building a 3-dimensional X-beam structure model, the masks for different layers of the structure need to be built in 'IntelliMask'. 'IntelliMask' is specifically designed for constructing and editing MEMS device level masks, which will later to be imported into 'IntelliSuite' '3D Builder' package. '3D Builder' can import mask files in DXF and GDSII formats, both are industry standards file format to layout the mask for microfabrication lithography, including MEMS device. In this project, mask file was constructed in DXF format.

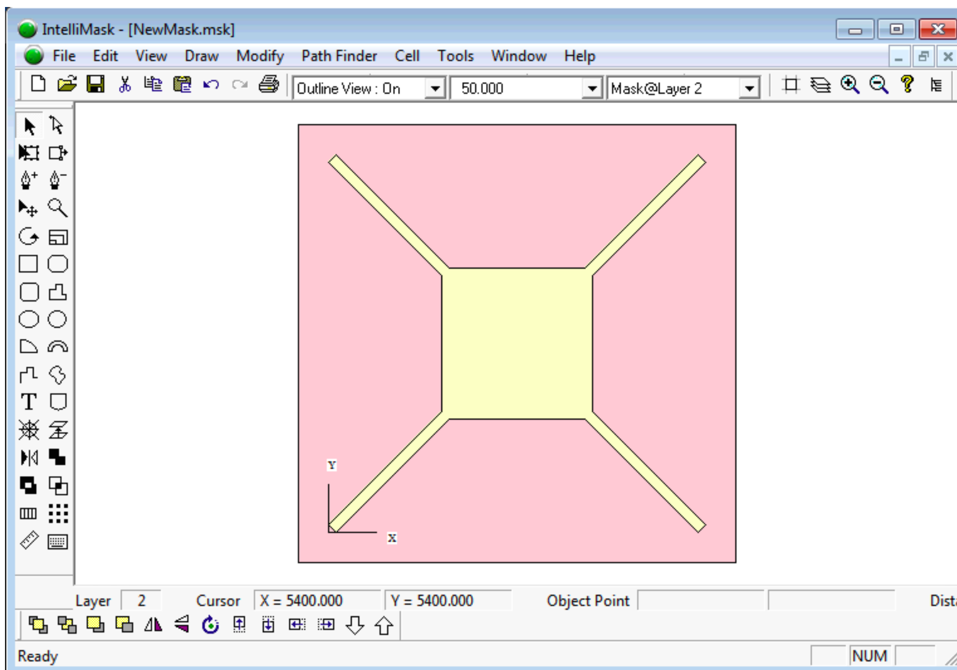

Fig. 4.7 The Layout of the X-beam Structure. The 'IntelliMask' is used to lay out the three mask layers of the X-beam structure. The DXF file is generated from the mask layout and fed into the 3D Builder for further analysis.

Three mask layers are the required to model the 3-dimensionl X-beam structure. The first layer, Layer 0, is a square shape mask that simulates the silicon substrate. The second layer, layer 2, is used to simulate the gap between the top and bottom plates of the X-beam structure. As such, it is left empty as an air gap so the top membrane X-beam structure can actuate. Lastly, the X-beam structure is constructed on the third mask layer. Once all three masks are laid out in the 'IntelliMask', the file will be saved as a single multi-layer DXF file. Each layer is saved in the DXF file with its name, layout geometry, and other description of the layer.

3D Builder

In '3D Builder', 'IntelliSuite' 'DXF file converter' converts the multi-layer DXF file into a multi-layer MSK file. The mask file is imported by selecting 'Mesh' option, then 'Automesh from mask layout' option, and finally the mask file that was saved from 'IntelliMask'. Once the mask file is successfully imported, '3D Builder' presents the configured finite elements meshes that is constructed based on the mask file.

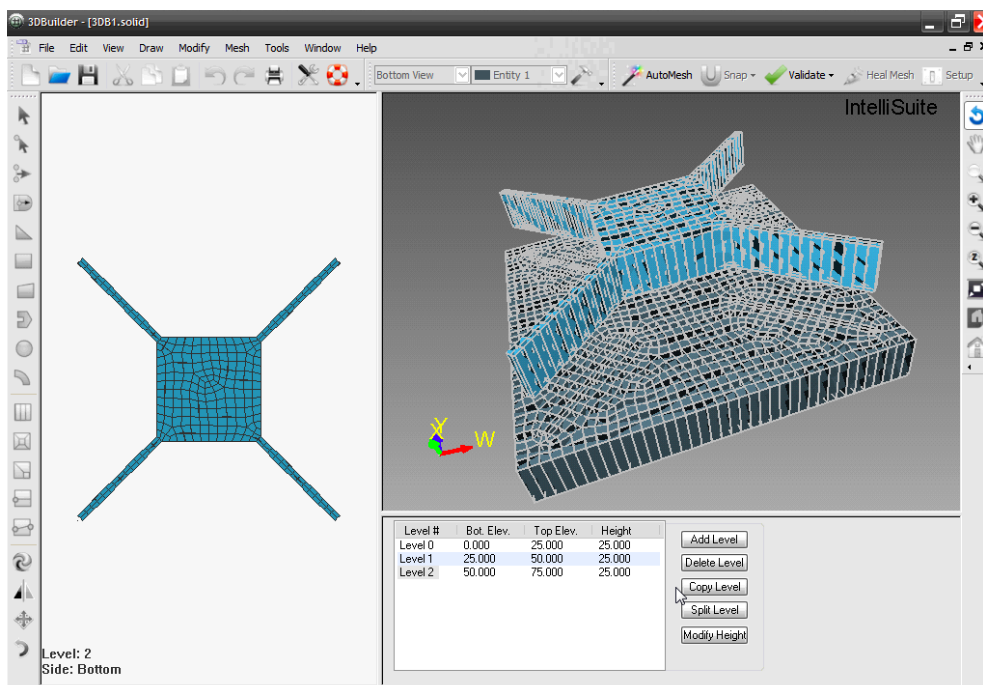

Fig. 4.8 The 3-dimensional Model of the X-beam Structure is constructed in 3D Builder. The mesh generated for the finite element analysis is shown on the screen shot. The vertical dimension is exaggerated to visualize the meshes clearly.

In order to differentiate X-beam and substrate as different entities, substrate is assigned as Entity 1 and X-beam is assigned as Entity 2. In the lower right-hand corner of '3D Builder' window, a list of all current element levels can be found. Heights of Level 0 and Level 2 are both modified to 25 µm to match the thickness of the X-beam and substrate. Level 1 is the air gap between two membranes for electrostatic actuation and its height is set to be 25 µm, which matches the initial gap distance, g_0.

To ensure no overlapped elements or illegal elements are found within the configured element mesh, two validations, 'Validate Mesh Connectivity' and 'Validate Mesh Conformity' under 'Mesh' option, need to be performed. During this

process, all overlapping or illegal elements will be automatically selected and highlighted in white. Any overlapped or illegal element must be corrected before exporting the file to Analysis Module.

Thermo-Electro-Mechanical Analysis (Device analysis and simulation)

'IntelliSuite' provides three different analysis modules: 'Thermo-Electro-Mechanical', 'MicroFluidic', and 'ElectroMagnetic'. Since our device has both electrical (parallel plate capacitor) and mechanical components (the X-beam springs), our parallel plate actuator with the X-beam structure is analyzed with 'Thermo-Electro-Mechanical Analysis' module.

The analysis type is set to be 'Thermo-Electro-Mechanical Relaxation' under 'Simulation Setting' with iteration number of 3 and iteration accuracy of 0.001 for all the simulation analysis done on the 3-dimensional X-beam model. Silicon material is chosen for both the X-beam (Entity 2) and the substrate (Entity 1). All the material properties of the silicon are set to the default values, except the Young's modulus. Since the substrate is fabricated from the single crystal silicon wafer, the Young's modulus of 169 GPa is used, instead of the default value of 160 GPa, an approximate value for polysilicon. For the X-beam, since the beam spring is aligned with 45 degree from the wafer flat, the Young's modulus is changed to 130 GPa.

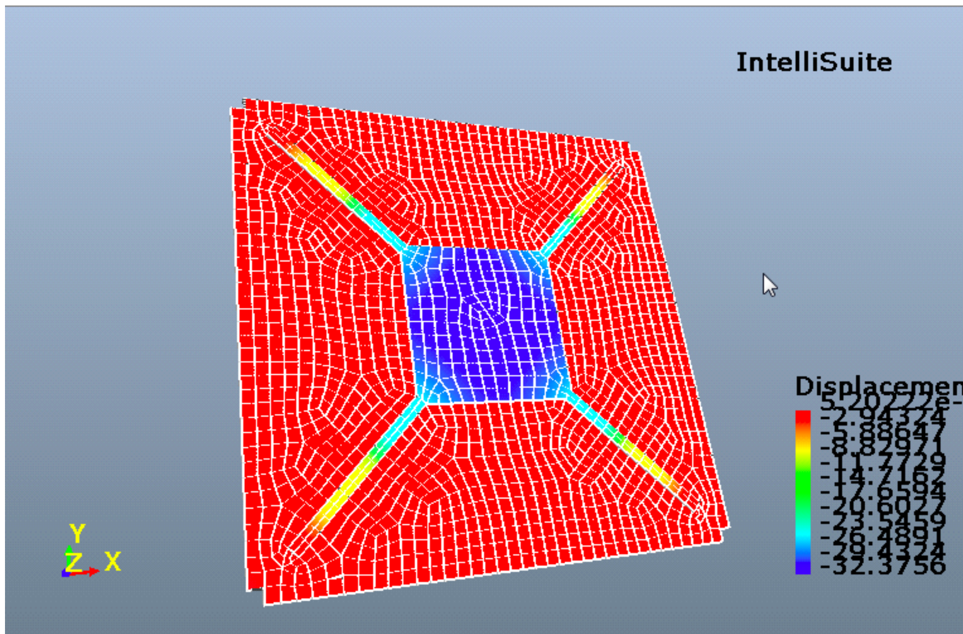

Fig. 4.9 The Graphical Solution of the FPI Electrostatic Actuation on Thermo-Electro-Mechanical Analysis Module. A simulation with 150 V bias voltage is performed. At this voltage, the pull-in already sets in, and physically impossible deflection of 32.3756 μm is shown (the initial gap is only 25 μm).

Once the model parameters are set, the substrate (Entity 1) is applied with voltage range of 0 V to 150 V with increment of 10 V, and the X-beam structure (Entity 2) is held at 0 V. In the Thermo-Electro-Mechanical Analysis, the bottom plane of the substrate as well as the lateral faces of the x-beam are fixed as the boundary condition. Finally, ‘Start Static Analysis’ under ‘Analysis’ option is chosen to start the simulation analysis.

The result of the ‘IntelliSuite’ simulation is given in figure 4.10 with the graph of the electrostatic actuation obtained with the analytical calculation in subsection 4.2.1. The numerical solution turned out to be more responsive to the applied bias voltage. It indicates more deflect distance at given bias value. To tune the FPI to

cover the specified operational spectral range of 8-11 μm, the gap between two plates need to change from 4 to 5.5 μm, and a total of 1.5 μm deflection distance necessary. It is demonstrated, in both analytical and numerical solution of the electrostatic actuation of the X-beam structure that required X-beam deflection can be achieved under a bias voltage of 80 V.

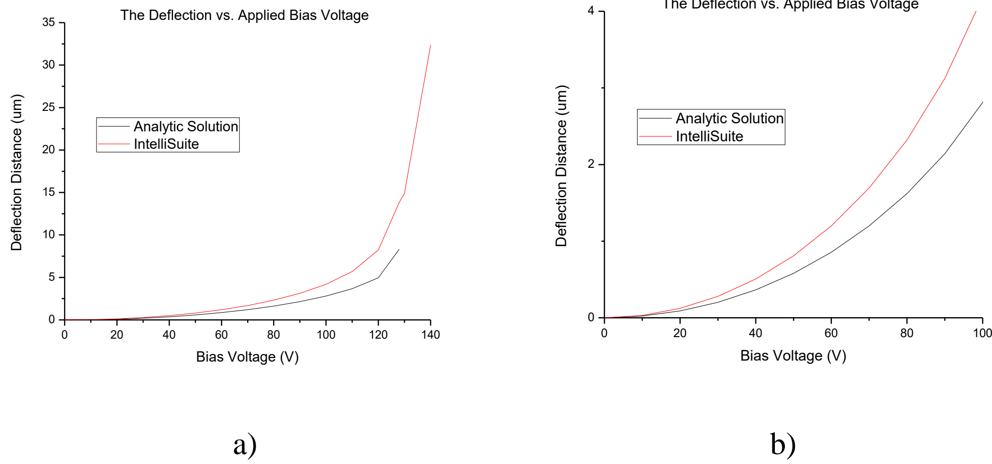

a) b)

Fig. 4.10 The Electrostatic Actuation of the FPI. a) A numerically simulated graph of deflection distance of the FPI vs. bias voltage is presented (red), with the values calculated analytically (black). Both graphs show cubic behavior with the pull-in around 130 V. b) Zoomed-in view of the first graph. The necessary deflection of 1.5 μm is achieved under bias voltage of 80V in both solutions.

4.3 The filtering performance of the FPI in λ = 8-11 μm

The filtering and tuning performance of the FPI in the 8-11 μm spectral region is simulated with the expression for the transmittance of the FPI, $T_{FP} = \frac{(1-R)^2}{(1-R)^2+4Rsin^2\varphi}$ (equation 2.10). This expression is found by squaring the transmission coefficient t, that we obtain by adding all the transmitted lights using the

geometric series ($t = t_{12}t_{23}e^{-i\varphi}\left(1 + r_{23}r_{21}e^{-2i\varphi} + \left(r_{23}r_{21}e^{-2i\varphi}\right)^2 + \cdots\right)$ = $\frac{t_{12}t_{23}e^{-i\varphi}}{1-r_{21}r_{23}e^{-2i\varphi}} = \frac{t_{12}t_{23}e^{-i\varphi}}{1+r_{12}r_{23}e^{-2i\varphi}}$, equation 2.5). Here t_{ij} and r_{ij} are the transmission and reflection coefficient at the ij-boundary when the light incident from medium i and emerges into medium j, and the phase factor ϕ accounts for the phase change the light acquires between two successive reflection or transmission. See section 2.1 for more detailed discussion.

In the simulation, the value of the phase factor $\varphi = \frac{2\pi d}{\lambda} n_2 cos\theta_2$(equation 2.6) in T_{FP} is varied as the wavelength λ of the incident EM-wave is swept from 6.5 to 12.5 μm. The normal incident angle is assumed, so we have $\theta_2 = 0$. The air is the medium between two mirrors ($n_2 = 1$). The simulation is done with the value of the gap distance d varied from 4.0 to 5.5 μm, in a step of 0.25 μm, covering the desired operational spectrum range of λ = 8-11 μm. Two simulations are performed. For the first simulation, R = 0.95 is assumed throughout the 6.5 to 12.5 μm spectral range we simulated. The result is shown in figure 4.11. With a constant DBR reflectance of 0.95, sharp transmission peaks at the expected wavelengths are observed. It demonstrates the expected filtering and tuning performance of our FPI filter.

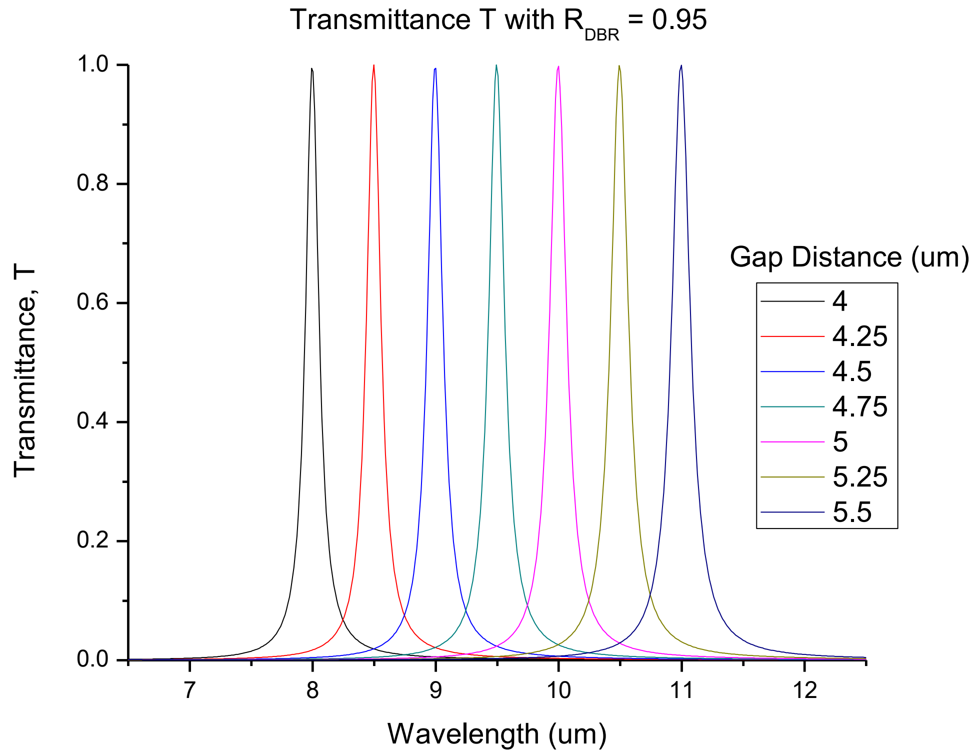

Fig. 4.11 The Transmission Spectrum of the FPI Filter with Constant DBR Reflectance R of 0.95. Narrow transmission peak is observed at the expected wavelength ($\lambda = 2d$). It demonstrates the filtering and tuning performance of the FPI filter.

As discussed in section 2.2 and demonstrated in section 4.1, the reflectance R of the DBR does not maintain a constant value throughout the entire operational spectral range of 8-11 μm. Therefore, it is meaningful exercise to simulate the FPI filtering and tuning performance by calculating the transmittance T of the FPI at various gap distance with the calculated reflectance R of the DBR that varies along the wavelength of the incident EM wave. The reflectance R of the DBR with 25 μm silicon membrane and zinc sulfide AR coating on the back side of the membrane is used in the calculation. Previously, we use the constant value of the DBR reflectance

(R = 0.95) to calculate the transmittance T of the FPI with $T_{FP} = \frac{(1-R)^2}{(1-R)^2+4Rsin^2\varphi}$ (equation 2.10) and $\varphi = \frac{2\pi d}{\lambda} n_2 cos\theta_2$(equation 2.6) as the wavelength of EM wave is swept from 6.5 to 12.5 μm. The simulation proceeded similarly, except that instead of constant reflectance of R = 0.95, a simulated wavelength dependent reflectance R of the DBR is used in the calculation.

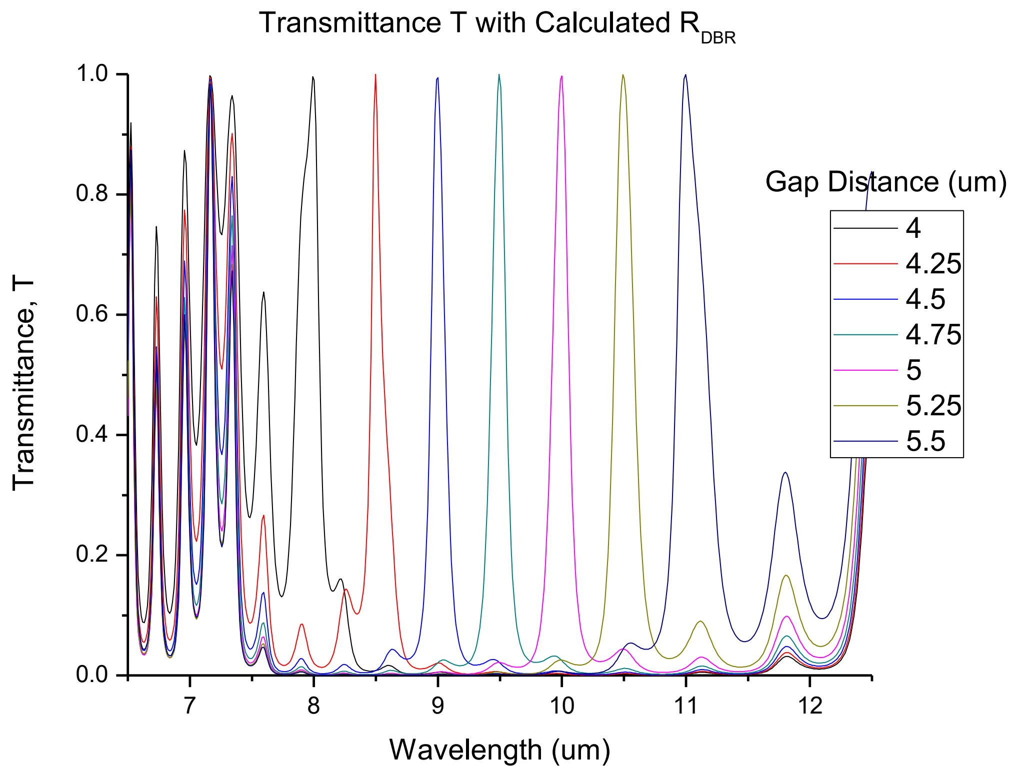

Fig. 4.12 The Transmission Spectrum of the FPI Filter with Wavelength Dependent DBR Reflectance R. Increased FWHM indicates a degradation of the filtering performance. A periodic interference pattern from thin Si membrane is also observed.

The result is shown in figure 4.12. The degradation of the transmission peak is observed, as well as periodic interference pattern caused by thin Si membrane. The

distortion is worse in the shorter wavelength region of the spectrum. However, different gap distance produce transmission peak at the expected wavelength, and each transmission peak is clearly discernable even with the degradation from the variable DBR reflectance. Thus, we conclude that the expected filtering and tuning performance of our FPI filter will meet the design specification with our design parameters.

The expected FWHM of above two FPI simulations are given in table 4.1, in comparison with the theoretical value from $\Delta\lambda_{\frac{1}{2}} = \frac{\lambda}{m}\frac{1-R}{\pi\sqrt{R}}$ (equation 2.14) with m =1, for each transmission peak. Both constant and wavelength dependent reflectance produce compatible FWHM values. It strengthens the validity of the simulated performance.

Wavelength (μm)	FWHM (μm) with Constant R of 0.95		FWHM (μm) with Wavelength dependent R		
	Calculation	Simulation	R	Calculation	Simulation
8	0.131	0.127	0.947	0.139	0.197
8.5	0.139	0.144	0.966	0.094	0.114
9	0.147	0.152	0.950	0.147	0.120
9.5	0.155	0.156	0.954	0.142	0.128
10	0.163	0.157	0.953	0.153	0.139
10.5	0.171	0.168	0.937	0.218	0.176
11	0.180	0.168	0.938	0.224	0.258

Table 4.1 The Simulated FWHM of the FPI. A constant R of 0.95 and wavelength dependent variable R are used in the calculation. In variable R case, the reflectance value is shown as well. Both cases, the calculated and simulated FWHM agree well within 10% with each other.

CHAPTER 5. THE FABRICATION OF THE FPI FILTER

The fabrication of the FPI filter is performed in three separate stages in order; 1. fabrication of top and bottom membranes for physical base structure for the FPI, 2. deposition of the DBR mirror on the membranes, and 3. assembly of two membranes with mirrors into the FPI filter. In this chapter, the detailed process used to perform the fabrication of the FPI filter is described. The entire fabrication process was performed at the Stanford Nanofabrication Facility (SNF). Located at the Stanford University campus, the SNF provides a full suite of equipment to supports electronics-based device fabrications in micro- and nano-scale. The 10,000 sq. ft. main class 100 clean room and four satellite labs in the SNF are open to academic, industrial, and governmental researchers across the U.S. and around the globe. The equipment in the SNF used in this project is described and followed by the details of the fabrication process of each membrane. More detailed description of the fabrication equipment can be found at the SNF wiki page (https://snf.stanford.edu/).

5.1. The Fabrication Equipment in the SNF

5.1.1 The Optical Photolithography Tools

The optical photolithography consists of photoresist spin, exposure, develop, and many bake steps along the process. For the bake, numerous ovens are available at various pre-set temperatures in the lithography area at the SNF. The descriptions of the spin coater, manual exposure tool, and automatic developer are followed by a typical optical photolithography process sequence.

5.1.1.1 The SVGCOAT and SVGCOAT2

The SVG (Silicon Valley Group) coater is an automated single-wafer track system for dispensing photoresist on 4-inch silicon, glass, or quartz wafers. It can dispense three different positive photoresists and one image reversal resist (Shipley 3612 for 1 or 1.6 µm, SPR220 for 3, 4, 7, or 10 µm, SPR955 for 0.7 or 0.9 µm to 1 µm, and AZ5214IR for 1.26, 1.4, 1.6, or 2.0 µm Image Reversal). In addition to these photoresists, user specific photoresist can be used on track 1 upon approval of the SNF staffs. The svgcoat system includes two stations: a prime oven which bakes the wafer and dispenses the adhesion promoter hexamethyldisilazane (HMDS) and a combination spinner, which dispenses photoresist, and pre-bake oven which cures the resist. HMDS is only available at track 2. The uniformity of spun photoresists is typically +/- 100 Å. At each station, user can select from many pre-written standard recipes consists of different combinations of pre-programed spin cycle, bake oven sequence and the edge bead removal (EBR) size.

Fig. 5.1 The SVGCOAT tracks

In our project, all the wafer-based resist coat is done on the svgcoat system. The detailed recipe is given in section 5.2, where we describe the fabrication process.

5.1.1.2 The Karlsuss and Karlsuss2

The Karlsuss MA-6/BA-6 contact aligner system is a 1:1 contact alignment/exposure tool. It can perform precision mask-to-wafer front- or back-side alignment and near-UV photoresist exposure in hard- and soft- contact, as well as high and low vacuum contact; proximity contact is not available. The SNF has two MA-6 aligners (karlsuss and karlsuss2). Currently they are configured to accommodate 3-, 4- and 6-inch wafers and pieces. Because the alignment is done manually on a wafer-to-wafer basis, the Karlsuss aligner is less suitable for high through-put IC production and more designed for applications in R&D projects and a small-scale production. In the Karlsuss system the resolution is maintained by exposing the wafer in contact with the mask. Since it is a 1:1 exposure system, the resolution of the exposed patterns on the wafer is basically determined by the

resolution of the mask used. Sub-micron masks are expensive to produce. Therefore, it is recommended to use a reduction lithography system such as the ASML for those projects. Although the light available for exposure is the DUV (240nm) and the I-line (365nm) as in the ASML, the system is limited to a minimum of 1um (vacuum contact) in resolution compared to 0.45um or less on the ASML. This higher resolution on ASML is achieved through diffraction-limited precision reduction optics. In terms of alignment, it is limited to about +/-0.5um (+/-1.0um in practice) in alignment accuracy for the front-side and +/-1.0um (larger in practice) for the back-side.

The resolution and alignment accuracies of the Karlsuss system are more than enough for our project requirements (~10 um). On top of that, it is a better tool to use since we have large fields on our mask (~10 mm). In the FPI project, therefore, all the photoresist exposures are performed with the Karlsuss2. The detailed parameters used are given in section 5.2.

Additionally, we used the Karlsuss system in the packaging stage to harden the liquid UV glue to put top and bottom membranes together into the final FPI assembly. The detailed procedure is described in section 5.4, where we discuss the assembly of the FPI filter.

Fig. 5.2 The Karlsuss System

5.1.1.3 The SVGDEV and SVGDEV2

The SVG (Silicon Valley Group) developer is an automated system with two independent tracks (svgdev and svgdev2) for developing and post-baking exposed photoresist coated on a 4-inch wafers. Each track system includes two stations: a spin station which dispenses and rinses away developer and an oven station for post-bake. It uses developer MF-26A (2% TMAH, base). User can select from pre-programmed recipes with different development and post-bake time settings at the developer and the bake stations individually.

All the wafer-based resist developments are performed on the svgdev system in our fabrication process. The detailed recipe is given in section 5.2.

Fig. 5.3 The SVGDEV and SVGDEV2

5.1.1.4 A Photolithography Process Sequence

The typical photolithography process consists of the following seven steps with variation in step parameters. Notes are added at the end of each step description when a special consideration is given for our FPI filter fabrication process.

1. Singe and Prime: The wafer is singe baked to drive off moisture on the surface of the substrate which will interfere with the Prime step. Singe bake is followed by prime. "Prime" is a vapor deposition coating of the substrate surface by hexamethyldisilazane (HMDS). Surfaces that are normally hydrophilic (such as silicon with native oxide, silicon dioxides and nitrides) become hydrophobic when coated with HMDS, which allows for better resist coverage and adhesion. Wafers are singed and primed in every lithography step during our FPI filter fabrication process.

2. Spin Coat: A photoresist, in viscous liquid form, is dispensed onto a spinning substrate. By controlling PR dispense and spin speeds, resist spreads across the wafer in a uniform coat of desired thickness. Additionally, solvent may be dispensed on the

wafer backside, in order to ensure the wafer backside is clear of resist, and on the front side wafer edge, to remove resist on the edge ("Edge Bead Removal" or "EBR"). Residual resist on the wafer backside and edges can result in processing problems in the downstream process, particularly during expose. EBR is especially helpful in eliminating resist particulates (by removing "threads" of resist which form by spinning off at the wafer edge) and prevents sticky resist problems in equipment with automatic wafer handling. There are many formulations of resist available at the SNF, depending on the application and patterning need. A complete list of available photoresists with their thickness options can be found in subsection 5.1.1.1. The detailed information on the PR spin and bake parameters used in our fabrication is described in section 5.2.

3. Pre-Bake: This step drives off excess solvent and turns the resist from a liquid into a film. Before pre-bake, wafers are considered to contain hazardous chemicals and may be handled only under exhausted areas of the lab. Once wafers undergo pre-bake, they may be handled in the open. Singe and prime, spin coat, and the pre-bake (steps 1, 2, 3) are performed on the SVGCOAT, an automated track PR coating system.

4. Expose/Align: Optical resists are patterned by exposure to UV illumination. Exposure is performed through a "mask", which is a transparent plate custom-patterned with UV-opaque features. Most common mask materials are chrome pattern on a quartz substrate. In many cases, this process is followed by alignment and further exposure, since patterning of resist on a substrate already

containing another pattern requires alignment of the mask to the existing pattern. UV exposure tools generally fall into two classes: "contact aligners" in which the mask material is brought into direct physical contact with the resist-coated substrate; and "reducing steppers" in which the mask image is optically reduced and projected onto the resist-coated substrate. For the FPI fabrication, the Karlsuss MA-6/BA-6 1:1 contact alignment/exposure tool is used. To reduce fabrication cost, a pattern printed on mylar film is used as photolithography mask. As described in figure 3.2, only four masks are used for entire fabrication process. No front side alignment was necessary since we had only one pattern on each side of the wafer. However, the patterns on the device layer and the handle wafer need to be aligned with each other. Consequently, backside alignment, where the pattern on the front side of a wafer is aligned with the one on the backside of the wafer, is performed on both top and bottom membrane fabrication.

5. Post-Expose Bake: This optional step is used to “set” chemically-amplified resists, so that finer features and smoother vertical-wall profiles can be achieved. It is recommended for desired resolutions of less than 2 microns. Even though the feature size in our device is much larger (> 10 μm) than that necessitate the post-expose bake, it is included throughout the fabrication process to ensure the sharp corner of the X-beam structure.

6. Develop: To removes resist in UV-exposed areas (positive resists) or in UV-protected areas (negative resists) to produce a desired PR pattern on the surface of the substrate, a resist specific developer chemical is poured on the UV exposed

photoresist. Generally, this step is less critical to the quality of the lithography process than other steps. At the SNF, MF-26A (2% TMAH, base) is the standard PR developer.

7. Post-Develop Bake: This optional step drives off moisture, harden the resist or reflow sharp resist profile corners. Since most of the photolithography patterns are used as etch masks, every PR development is followed by the post-develop bake in our process. The post-expose bake, develop, and the post-develop bake (steps 5, 6, 7) are performed on the SVGDEV, an automated PR develop track system.

5.1.2 The Deposition Tools

There are two material deposition needs in the FPI fabrication process. First, we need to deposit a silicon dioxide (SiO2), an oxide for short, on the wafer as an etch mask for a number of process steps during the top and bottom membranes fabrication. More importantly, once each membrane is fabricated the DBR mirror needs to be deposited on the designated area on them. For the oxide deposition, we used the CCP-Dep. The Innotec is used in the DBR mirror deposition. The descriptions of these tools are followed.

5.1.2.1 The CCP-Dep

The CCP-Dep is a PlasmaTherm Shuttlelock model SLR-730-PECVD system configured for a Plasma Enhanced Chemical Vapor Deposition (PECVD). At the SNF, this tool is primarily used for the deposition of low-stress silicon nitrides (Si_3N_4), silicon oxides (SiO_2), amorphous silicon (a-Si) and silicon carbides (SiC) on a variety of substrates. A PECVD system reacts precursor gases in a RF plasma to deposit materials. The plasma allows the deposition to occur at a lower temperature

than a pure thermal process does. The CCP-Dep operates at 13.6MHz, has a load lock and one deposition chamber. The system is configured in what is called a CCP (Capacitive Couple Plasma) configuration, also known as a parallel plate configuration. In this tool the wafers sit on the grounded plate/electrode and RF power is supplied to the top plate/electrode where the gas is introduced through holes in this electrode. This configuration is useful for depositions in low density plasmas where ion bombardment is less damaging. The CCP-Dep system is dedicated for working with 4-inch wafers using a holder with four 4-inch wafer slot which moves between the load lock and the deposition chamber. After the holder is moved into the deposition position, the electrode move up and holds the wafers above the holder. The electrode fully contacts the back of the wafers during the deposition, so their temperature is uniform and there is no deposition to the wafer backsides.

The CCP-Dep is used to deposit the oxide to be used as an etch mask for a variety of patterns with silicon dry etch during the membrane fabrication process. The parameters used in the deposition is given later in section 5.2.

Fig. 5.4 The CCP-Dep

5.1.2.2 The Innotec

The Innotec ES26C E-beam Evaporator is an Electron Beam Physical Vapor Deposition (EBPVD) system, capable of depositing either single or multiple metallic thin films. In general evaporation systems heat a source to induce a vapor pressure greater than the pressure to which the deposition chamber has been pumped down. Typically, this means creating a vapor of at least a few mTorr. Different evaporation systems used different techniques to heat the source sample. In EBPVD system, such as the Innotec, the source material is heated very locally with a beam of high energy electrons. Because the beam can focus so much energy into such a small volume (<1 mm^3) temperatures higher than 3000°C can be achieved. The evaporated material is

deposited on the substrate (and the rest of the chamber) at a rate dependent on the distance from the source, so typically wafers are arranged in a hemisphere to aid in wafer to wafer uniformity. The deposition of the desired film is essentially a vapor condensation process as the evaporated source particles stick to cooler surfaces in the chamber or on the substrate. The metal atoms stick as soon as they arrive at the surface, not allowing for much movement that can help with step coverage or limiting stress. The substrate temperature has a great influence on the film stress by controlling the degree the source metal particles stuck together when they hit the substrate. Hotter the substrates lesser the stress on the deposited film. A rule of thumb is that the higher the melting temperature of a metal, the higher the stress of the film. In Innotec, like many other typical EBPVD systems, metal films evaporated onto unheated Si substrates. In such case, the resulting stress will be tensile. Deposition through evaporation is a directional process and hence very good for lift-off applications. The Innotec can achieve precisely controlled film thickness less than 1 A in resolution using crystal monitoring. The available sources for film deposition in the Innotec are: Ag, Al, Au, Co, Cr, Cu, Fe, Ge, In, Mo, Ni, Pd, Pt, Si, Sn, Ti, Ta, and W. In addition, Er, Hf, Ir, Ru, Tb, and Y are allowed, but not provided at the SNF. In general, evaporated films have worse adhesion to the substrate than sputtered films. Adhesion depends on the film material, the substrate material, and the stress in the film. Certain applications require films such as gold (Au) and silver (Ag) may need a thin “adhesion layer” to be added first. Chrome (Cr) is the most commonly used adhesion layer for Au and Ag for Si and quartz substrates.

In our project, the DBR mirror consist of alternating layers of Zinc Sulfide (ZnS) and Germanium (Ge). Germanium is one of the deposition sources available in the Innotec at the SNF. Zinc sulfide needed a special permission from the SNF to be used in the Innotec. The parameters used in the deposition is given in section 5.3, where DBR mirror fabrication is described.

Fig. 5.5 The INNOTEC

5.1.3 The Etch Tools

Two etch tools are used in the fabrication process to etch two different materials; the AMTETCHER for the oxide, and the STSETCH for both surface and bulk micromachining of silicon. They are described next.

5.1.3.1 The AMTETCHER

The AMTETCHER is Applied Materials Technologies 8100 Hexode plasma etcher. It is a Reactive Ion Etcher (RIE) that uses fluorine-based chemistry to etch

Oxides or Nitrides. It also can be used for Si trench etching. It can etch twenty four 4-inch wafers at a time, and is considered one of the most popular machine for low power RIE oxide, nitride and Si etching. The AMT 8100 etcher has been in constant use since it was installed in the lab in 1986 at the SNF.

Fig. 5.6 The AMTETCHER

In the FPI filter project, it is mainly used for the oxide etch to produce the oxide masks that subsequently used in the silicon etch with STSETCH. The nominal etch selectivity of AMTETCHER between the oxide and the photoresist (PR) is 3:1, with etch rate of 350 nm/min and 111 nm/min, for oxide and the PR, respectively.

5.1.3.2 The STSETCH

The STSETCH is STS Deep RIE etcher. It is an IPC (Inductive Charged Plasma) Deep Reactive Ion etcher from Surface Technology Systems. The platform is single-chamber, manual load lock system. The etch process is based on the patented Laermer and Schlip process, commonly referred to as the Bosch Process. With the Bosch process, a high aspect ratio Si etch can be performed regardless of crystal orientation. The etch process alternates between the passivating C4F8 plasma and the silicon etching SF6 plasma.

The nominal selectivity between the silicon and the photoresist and the silicon and the oxide in the STSETCH are 105:1 and 100:1, respectively, depending on structures being etched. Photoresist etches at about 250-600 A/min, depending on post-exposure treatment. Silicon etch rate is about 1.8-4 μm/min. In our project, the STSETCH is used both for the surface micromachining of the X-beam structure on the device layer of the top membrane and the bulk micromachining of the deep trench on the handle wafer for both top and bottom membranes.

Fig. 5.7 The STSETCH

5.2. The Fabrication of top and bottom membranes

Two membranes that are eventually assembled into the FPI filter are fabricated from the SOI wafers from the UltraSil Corporation. Three parameters are considered when we specify the SOI wafers to be used: 1. the thickness of the device layer, 2. the sheet resistance of the device layer, and 3. the thickness of the buried oxide (BOX) layer. The thickness of the device layer becomes the thickness of the beam spring of the X-beam structure, which influences the magnitude of the bias voltage needed to obtain the desired actuation of the DBR mirror on the top membrane. As analyzed earlier, the thinner the beam spring, the smaller the bias voltage required to achieve the necessary actuation range. Two of the shelf SOI wafer device layer thickness of 10 μm and 25 μm were investigated in the earlier stages of the project. Though advantageous in terms of low bias voltage required, the 10 μm device layer thickness was found to produce deformed membrane after the X-

beam fabrication [22, 23]. The DBR mirror were to be deposited on this membrane surface. As described later in chapter 6, the degree of how flat the DBR mirror is one of three parameters that determines the degree of degradation in the FPI filter performance. Therefore, despite the need of the higher bias voltage, we decided to use 25 μm thick device layer SOI wafer. The sheet resistance of the device layer also has two conflicting requirements. First, more free charge carriers the device layer has, more absorption of EM radiation it produces [6, 9, 19]. Since we want as small an absorption as possible for our filter, the high sheet resistance is desired. However, to actuate the FPI filter electrostatically we need a relatively good conductivity on both top and bottom membrane, so that the charging and discharging of them can be done within a reason amount of time. The sheet resistance of less than 0.005 Ω/cm^2 is chosen to accommodate both requirements. Finally, the BOX layer was to be used as an etch stopper for both the surface micromachining of the device layer and the bulk micromachining of the handle wafer. 2 μm of BOX layer thickness is chosen for our SOI wafer. Since we are getting the SOI wafers from the available inventory stocks in the market, no attempt was made to optimize the relevant device parameters. The complete description of the SOI wafer used, including the parameters discussed above, is given below in table 5.1.

Size	100 mm in diameter
Type (dopant)	Device layer: N (As), Handle wafer: N (P)
Orientation	DL: (100), HW: (100)
Thickness (μm)	DL: 25 +/- .5, HW: 400 +/- 15, BOX: 2 +/- 5%
Sheet Resistance (Ω/cm^2)	DL: < 0.005, HW: 1-30

Table 5.1 The description of the SOI wafer used in fabrication

Except the moveable X-beam structure on top membrane, two membranes were undergone a similar fabrication process; the patterning and etching of the device layer (surface micromachining), followed by the patterning and etching of the handle wafer (bulk micromachining).

5.2.1. The fabrication of the top membrane

The top membrane has the X-beam structure to tune the FPI filter within the spectrum of interest (λ = 8-11 μm) using an electrostatic actuation. Oxide etch mask for the X-beam structure is patterned on the device layer of the top membrane first and followed by dry etching process to fabricate the structure (surface micromachining). An X shape deep trench is then patterned and fabricated with dry etch process using bulk micromachining from the back side of the wafer to expose the X-beam so that it can move freely. For dry etching of both the device layer and the handle wafer, the 2 μm thick box oxide layer of the SOI wafer works as etch stopper. Once the X-beam structure is completed, the BOX is removed with wet etching before we proceed to the DBR mirror deposition to release the X-beam structure. The fabrication process steps are described individually.

Step 1: Using the CCP-Dep, a silicon dioxide (SiO2) is deposited on the device layer (DL) and the handle wafer (HW) of the SOI wafer with thickness of 1μm and 6 μm, respectively. Since the CCP-Dep can make deposition on only one side of the wafer, this deposition process is performed in two separate runs. The oxide deposition is done at 350° C. They are to be used as masks for subsequent silicon dry etch step.

Step 2: An optical photolithography is performed on top of the 1 μm oxide layer deposited in the previous step to pattern the X-beam structure on the device layer. This photoresist pattern is used as an etch mask for the 1 μm oxide dry etch in step 3.

Step 3: The oxide mask for the X-beam structure is etched on 1 μm oxide layer deposited in step 1 in the AMTETCHER. With 350 nm/min nominal oxide etch rate, 3 minutes of etch time is found to be adequate. The silicon under the oxide is to be etched out in the next step, and small amount of over-etch can be tolerated without any process complication. To prevent burnt PR during the Si dry-etch process, any remaining PR mask is removed with 20 min. Piranha treatment.

Step 4: The X-beam structure is etched on the DL of the SOI wafer. 25 μm thick silicon DL is patterned with dry etch in the STSETCH. The X-beam structure is successfully fabricated everywhere on the wafer surface in 8 min. 30 sec. etch time with nominal etch rate of 3 μm/min. The BOX as etch stopper no precise etch time control is necessary. The remaining oxide mask is removed in 30 sec. 2% HF deep. With these 4 steps, the process on the front side of the top membrane is completed. The front side of the wafer after steps 1-4 is shown in figure 5.8.

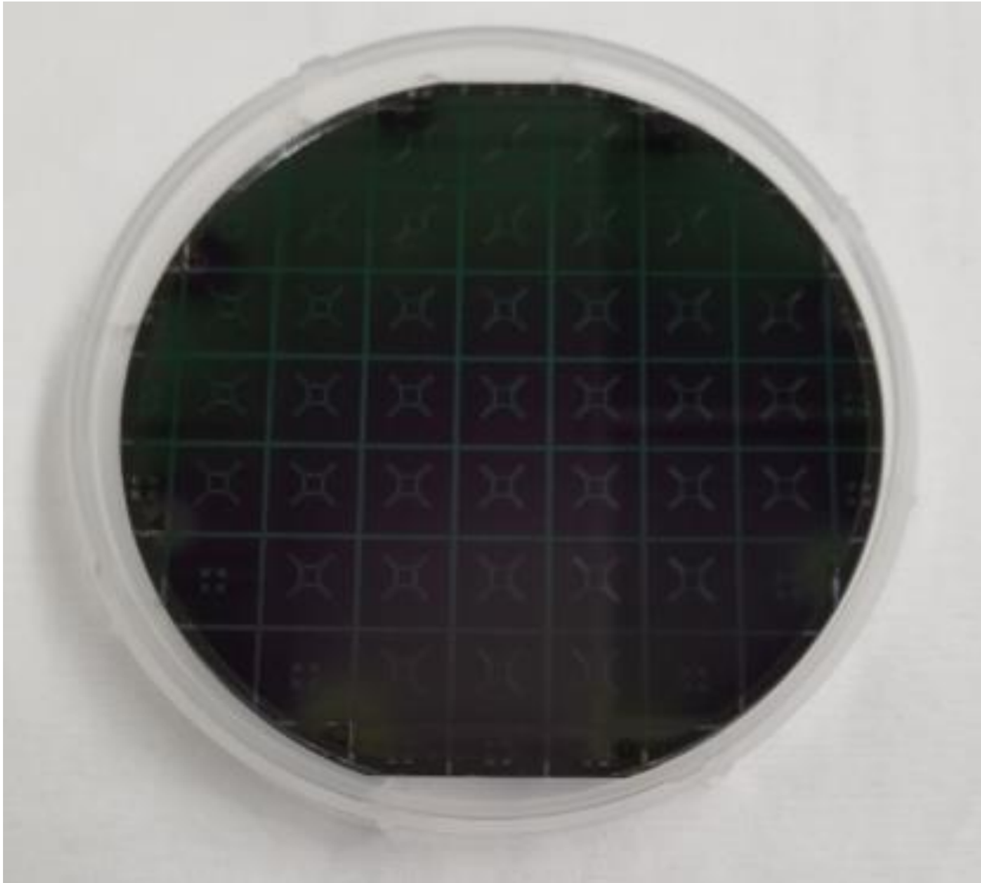

Fig. 5.8 The front side of top membrane wafer. The X-beam structures are patterned and etched. A total of 37 membrane chips are fabricated on a single 4-inch wafer.

Step 5: 1 μm oxide layer deposited with CCP-Dep on the DL to protect the X-beam structure while the HW side (backside of the SOI wafer) is being processed. The deposition condition is the same as in step 1. Once the top membrane fabrication is completed, this protective oxide layer will be etched with BOX in the release step using 2% HF wet etch.

Step 6: An optical photolithography is performed on the 6 μm oxide layer deposited on the DW in step 1 to pattern the X-shape trench. This trench is there to accommodate the electrostatic actuation of the X-beam. Entire 400 μm Si in the

handle wafer is through etched in the bulk micromachining. The PR pattern is used as an etch mask for the 6 µm oxide dry etch in step 7.

Step 7: The oxide mask for the X-shape trench is etched on 6 µm oxide layer deposited in step 1 in the AMTETCHER. With 350 nm/min nominal oxide etch rate, 18 minutes of etch time is found to be adequate. The silicon under the oxide is to be etched out in the next step, and small amount of over-etch can be tolerated without any process complication. To prevent burnt PR during the Si dry-etch process, any remaining PR mask is removed with 20 min. of Piranha treatment.

Step 8: The X-shape trench is etched on the HW of the SOI wafer. 400 µm thick silicon HW layer is removed with dry etch in the STSETCH. Though wafer etch to fabricate the X-shape trench takes 12 hr. and 30 min. To minimize the formation of the black silicon, and the etch rate changes due to increase in substrate temperature during the long etch, the trench etch is divided into three 4 hr. and 10 min. etch with 30 min. cool down in between. The BOX as etch stopper no precise etch time control is necessary.

The back side of top membrane wafer after steps 1-8 is shown in figure 5.9.

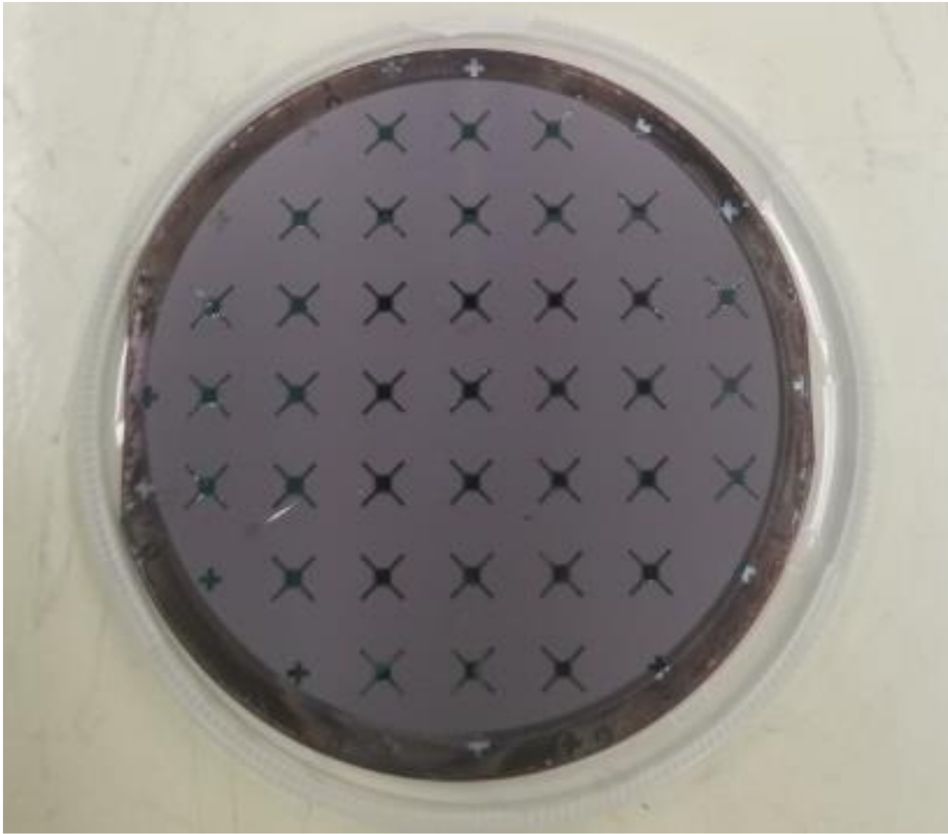

Fig. 5.9 The back side of top membrane wafer. The X-shape trenches are patterned and etched. The BOX layer used as the etch stopper can be seen in the X-shape trenches.

Step 9: The fabrication of top membrane with the X-beam structure is completed by last step to release the X-beam in the HF wet etch. 2 μm BOX layer and any remaining oxide mask are removed in 2 min. 6:1 BOE deep.

The front and back side of top membrane wafers after completing the fabrication is shown in figure 5.10, followed by the fabrication process flow of the top membrane in figure 5.11.

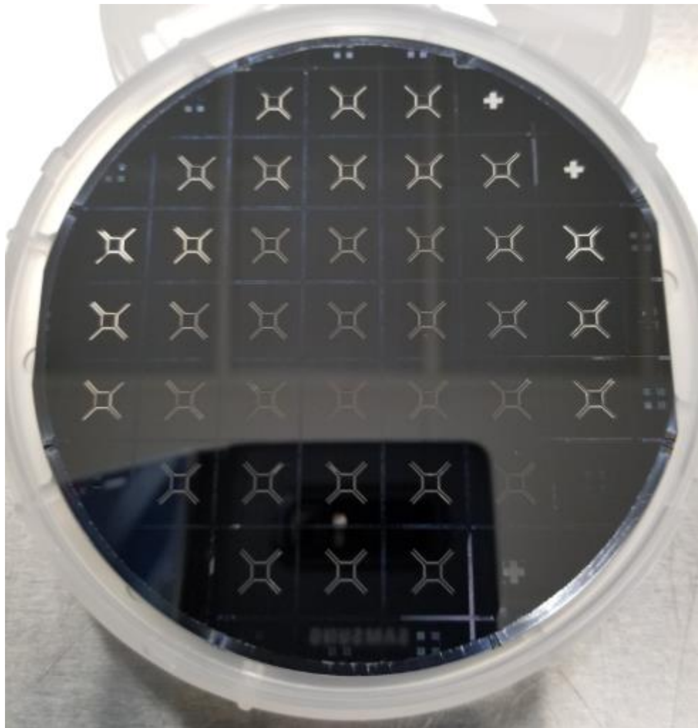

a) Completed front side of the top membrane

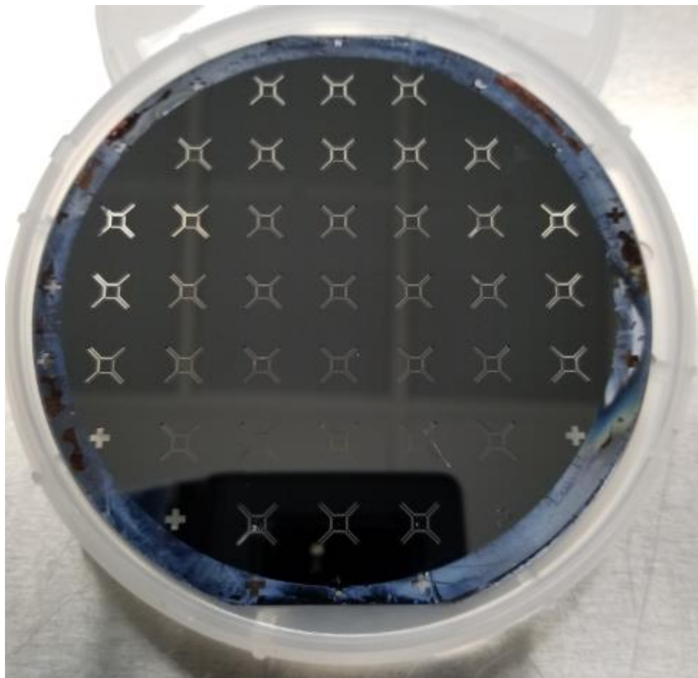

b) Completed back side of the top membrane

Fig. 5.10 Top Membrane with the X-beam structure after the Fabrication.

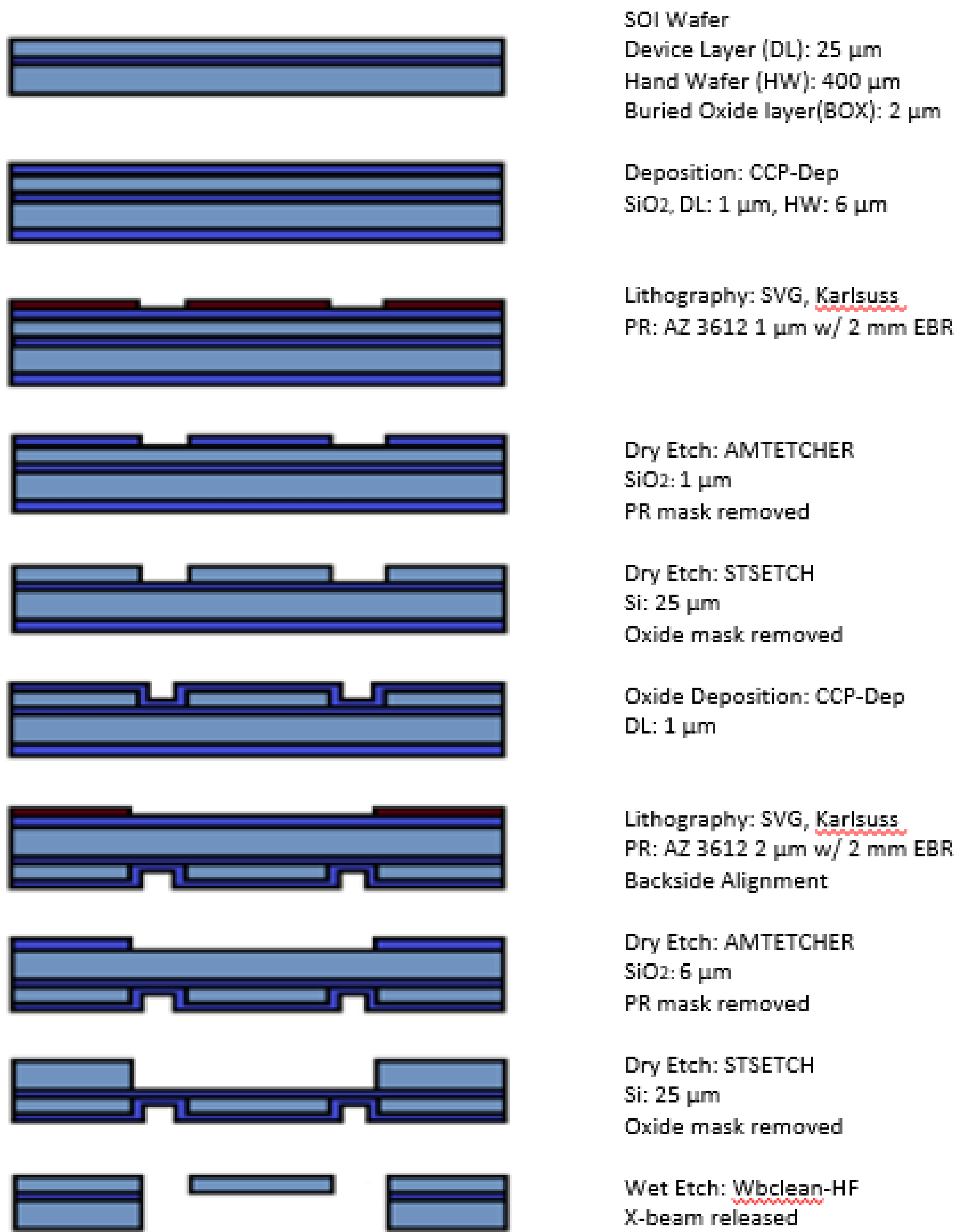

Fig. 5.11 The Fabrication Process Flow of the Top Membrane

5.2.2. The fabrication of the bottom membrane

The bottom membrane doesn't have any pattern on the device layer side. However, the four insulating pillars that were to be used in assembly step to define the gap distance between two membranes need to be prepared while the bottom membrane is fabricated. After the gap pillars are placed in the DL of the bottom membrane, 2 mm x 2 mm square membrane is exposed in the middle of the chip by through wafer etch similarly to the X-shape trench in the top membrane fabrication. Individual process step is described.

Step 1: 25 µm thick silicon dioxide ($SiO2$) is deposited on the device layer (DL) and the handle wafer (HW) of the SOI wafer with CCP-Dep. Since the CCP-Dep can make deposition on only one side of the wafer, this deposition process is performed in two separate runs. The oxide deposition is done at 350° C. As described in the design of the FPI filter, the necessary gap distance of the FPI filter is 25µm. This complicates the fabrication process significantly. The oxide on the device layer is to be the gap pillars after lithography and etch downstream. The oxide on the handle wafer is for the etch mask in the bulk micromachining. For this purpose, 6 µm of oxide thickness is enough. However, we found that asymmetric deposition of such a thick oxide only on one side of the wafer developed high surface stress that resulted in a curved wafer unsuitable for further process. In short, spin coater no longer maintains the vacuum between the wafer and the chuck necessary to spin it. To release the stress, we decided to deposit the same thickness of oxide on both sides.

Step 2: An optical photolithography is performed on top of the 25 µm oxide layer deposited in the previous step to pattern the gap pillars on the device layer. Thick 7 µm photoresist is used to pattern an etch mask for the 25 µm oxide dry etch in step 3.
Step 3: Four rectangular gap pillars are etched on 25 µm oxide layer deposited in step 1 in the AMTETCHER. With 350 nm/min nominal oxide etch rate, 75 minutes of etch time is necessary to fabricate the pillars. To prevent burnt PR during the Si dry-etch process, any remaining PR mask is removed with 20 min. of Piranha treatment.
With these 3 steps, the gap pillar fabrication process on the DL of the bottom membrane is completed. The back side of the wafer after steps 1-3 is shown in figure 5.12.

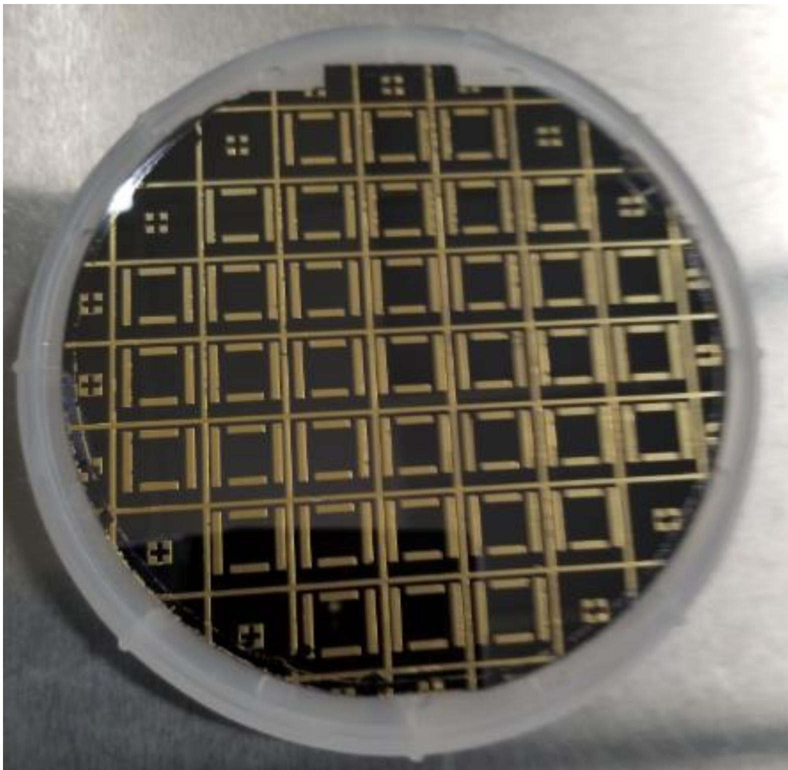

Fig. 5.12 The front side of bottom membrane wafer. Four gap pillars are patterned and etched on 25 µm oxide film. Also shown in the figure is the gold deposited on the pattern to accommodate eutectic wafer bonding attempt.

Step 4: 1 μm PR layer is spin coated with SVGCOAT on the DL to protect the gap pillars and the polished surface while the bulk micromachining is performed on the HW of the bottom membrane. The reason we used the PR for this protective layer is that when we etch the BOX layer in 2% HF wet etch at the last step of the process, the oxide gap pillars have to be protected as well. This PR layer will be removed in 20 min. Piranha bath.

Step 5: An optical photolithography is performed on the 25 μm oxide layer deposited on the DW in step 1 to pattern 2 mm x 2 mm square well. This well exposes 25 μm DL from the backside of the SOI wafer and produces a thin membrane where the DBR mirror is deposited. Entire 400 μm Si in the handle wafer is through etched in the bulk micromachining. The PR pattern is used as an etch mask for the 25 μm oxide dry etch in step 6.

Step 6: The oxide mask for square well is etched on 25 μm oxide layer deposited in step 1 in the AMTETCHER. 75 minutes of etch time is used. The silicon under the oxide is to be etched out in the next step, and small amount of over-etch can be tolerated without any process complication.

Step 7: A 2 mm x 2 mm square well is etched on the HW of the SOI wafer. 400 μm thick silicon HW layer is removed with dry etch in the STSETCH. Though wafer etch for the square well takes 12 hr. and 30 min. To minimize the formation of the black silicon, and the etch rate changes due to increase in substrate temperature during the long etch, the trench etch is divided into three 4 hr. and 10 min. etch with

30 min. cool down in between. The BOX as etch stopper no precise etch time control is necessary.

The back side of bottom membrane wafer after steps 1-7 is shown in figure 5.13.

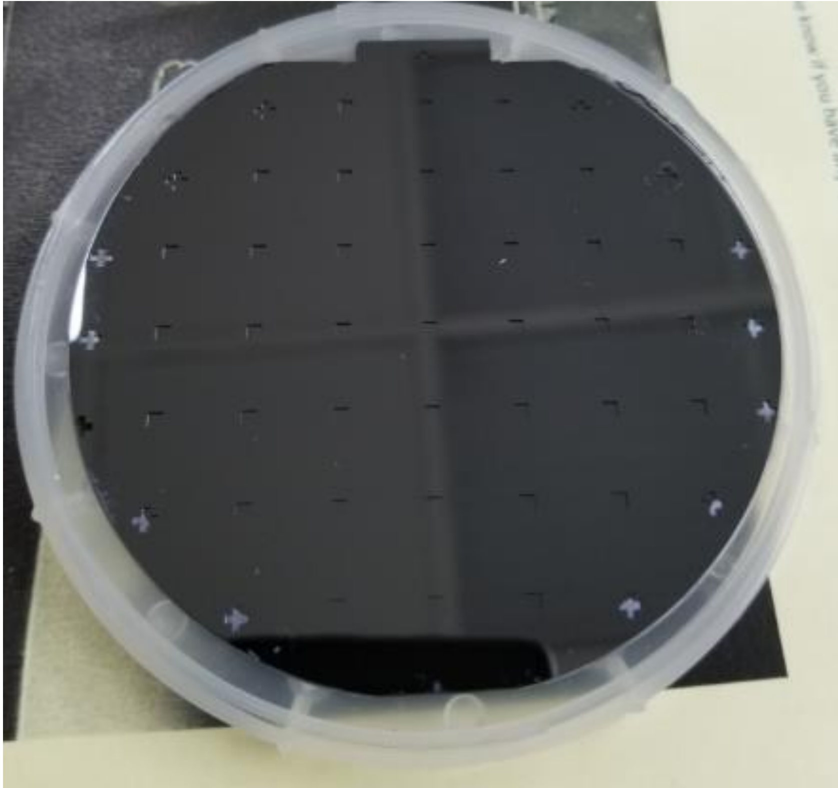

Fig. 5.13 The back side of bottom membrane wafer. 2 mm x 2 mm square wells are patterned and etched through the handle wafer exposing 25 µm DL membrane.

Step 8: The fabrication of bottom membrane with the gap pillars is completed by last step to remove the BOX layer and the protective PR film. 2 µm BOX layer is removed in 2 min. 6:1 BOE deep, followed by the removal of 1 µm PR using 20 min. of Piranha bath.

The fabrication process flow for the bottom membrane is given in figure 5.14.

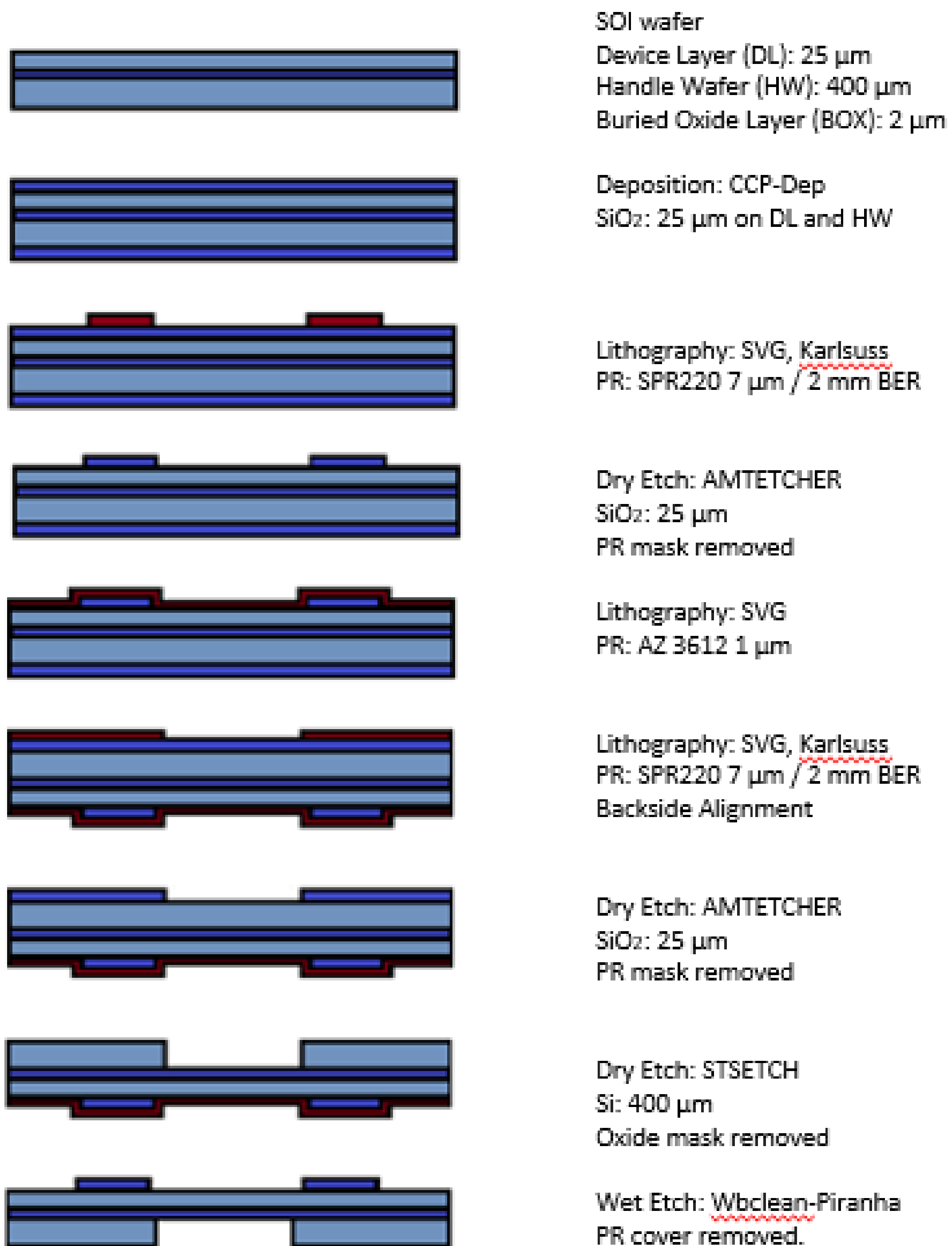

Fig. 5.14 The Fabrication Process Flow of the Bottom Membrane

5.3. The Deposition of the DBR mirror

In section 3.2, many different possibilities of source materials are considered, and the specification for our DBR mirror identified. To recapitulate, zinc sulfide (ZnS) and germanium (Ge) are chosen as low and high index material for the DBR, with n = 2.21 and 4.00 at the mirror design wavelength λ_C = 9.264 µm, respectively. With these parameters, thickness of each layer, are 2.316/4.00 = 0.579 µm and 2.316/2.21 = 1.048 µm for germanium and zinc sulfide quarter wave layer, respectively. The single stack of high and low index double layers is then 0.579 + 1.048 = 1.627 µm. At the same time, given the index contrast of 4.00/2.21 = 1.81, we calculated that five stacks of Ge/ZnS double layers is necessary to ensure the DBR mirror reflectance of better than 95% at the DBR mirror design frequency. This index contrast provides an adequate bandwidth of $\Delta\lambda$ = 3.448 µm that covers the entire operation spectrum.

The deposition method for the DBR mirror deposition is considered at the same time, and we found the electron beam physical vapor deposition (EBPVD) is adequate for our purpose. The Innotec, an E-beam chamber at the SNF, is used for the DBR mirror deposition. In subsection 5.1.2.2, the Innotec deposition is described as a line of flight process, where the vaporized target atoms/molecules travel in straight line from the source to the substrate in vacuum. This can be interpreted into two conflicting deposition conditions. To produce good quality film layer, the chamber vacuum needs to be as low as possible. On the other hand, low vacuum level means slow target evaporation and long deposition time. To balance the film

quality and the deposition time, we maintained < 10^{-5} mTorr throughout the DBR deposition. This consideration resulted in 40 min. and 120 min. of a single quarter wavelength layer deposition time for Ge and ZnS, respectively, and total of 14 hours of deposition for all five stacks. In addition, there is about 2 hr. of chamber pumping time after venting the chamber to load the sample and evaporant targets.

In spite of long chamber pumping time, we decided to remove some of the samples after the deposition of each stack of Ge/ZnS double layers to measure the improvement of the DBR reflectance as a function of the number of Ge/ZnS stacks. This added another 10 hours to the total deposition time. Breaking vacuum to remove the sample after the deposition of each stack gave a chance to replenish the deposition source at the same time. This was necessary for each deposition took a long time and the depletion of the evaporant target was significant. Due to extremely long deposition time, the DBR mirror deposition is performed in a period of 5 days.

The deposition is performed on a diced top and bottom membrane chips. A deposition shadow mask is prepared by through wafer etch using the bottom membrane HW lithography mask on a regular silicon wafer. The diced chips are attached to the shadow mask with 2 mm x 2 mm optically active area on the top and bottom membranes aligned with the square opening on the shadow mask. A kapton tape is used to minimize the outgassing in the vacuum chamber. Four top and bottom membrane chips are loaded with ten bottom membrane chips. After the deposition of each Ge/ZnS stack, two of ten bottom membrane chips are covered with mylar film to produce two samples of different stack number DBR mirrors (1-5 stacks). While two

samples are covered, the target materials are added as well. The chamber closed, and the pumping continued until the vacuum pressure inside the chamber reaches the desired level of 10^{-5} mTorr. This procedure was repeated until the 5 stack DBR is produce. The SEM picture of cross section of the 5 stack DBR is presented in figure 5.15.

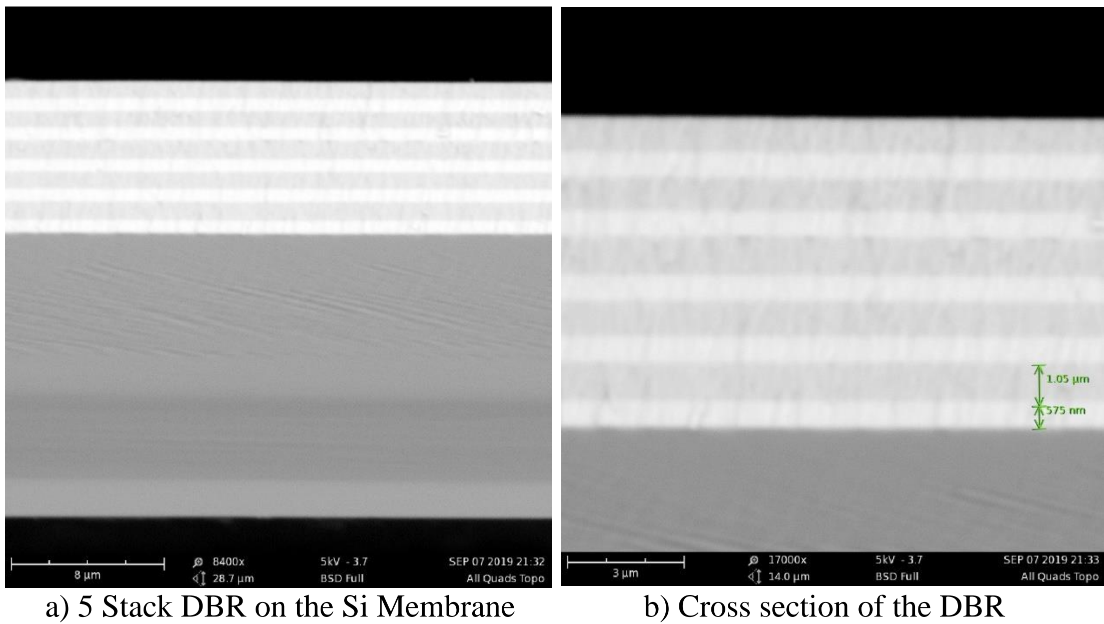

a) 5 Stack DBR on the Si Membrane b) Cross section of the DBR

Fig. 5.15 SEM Pictures of 5 Stack DBR. a) 5 stacks DBR on the Si membrane. b) Cross section of the DBR in detail. Five stacks of alternating layers of 0.575 µm of Ge and 1.05 µm of ZnS is clearly seen.

5.4. The assembly of the FPI

Assembling the FPI involves two important fabrication concerns. First, of course, is putting two membranes together as one unit. Even more important is ensuring the gap distance between two membranes as well as the parallelism between them. The gap distance because it is what determines the passing frequency of the FPI filter, and parallelism because it is one of the three main causes of the FPI

performance degradation as described in section 7.1. To satisfy this requirement in assembly step, we planned to use the SU-8 photoresist for assembly process initially. The SU-8 is a chemically amplified, epoxy-based negative resists that can be patterned with I-line (365nm) near UV radiation. Once cured after post-develop bake step, microstructures patterned on SU-8 films become very resistant to solvents, acids and bases and have excellent thermal and mechanical stability. Thus, they can be used in fabricating permanent structures such as pixel walls, fluidic channels and nozzles, micro arrays and spacers. With +/- 100Å uniformity from the SVGCOAT and 25 μm target height of the gap pillars, we can achieve +/- 0.4% gap distance tolerance. The SU-8 can be used to put top and bottom membranes together. There is a well-developed method extensively used in microfluidic channel fabrication, where the channel wells are patterned with SU-8 on two wafers or chips, then developed usually. The patterns are put on top of each other and cured in high temperature and pressure. During curing, two SU-8 patterns are fused and permanently locked together forming a side wall of the fluidic channel [41]. For our FPI filter, similar process can be used to form gap pillars to define the well-defined distance between two mirrors as well as assembling them together.

Unfortunately, budgetary restriction prevented us from using SU-8 during the FPI fabrication process. To circumvent this problem, we had to come up with an alternative fabrication method to process the gap pillar with very limited amount of time near the end of allocated fabrication period. The following process step is devised and used in the fabrication of the FPI filter:

1. A 25 μm thick oxide film is deposited on the devise layer side of the bottom membrane.

2. Four gap pillars are patterned on top of the oxide with 1 μm AZ 3612.

3. The oxide film is etched in the AMTETCHER and the gap pillars are exposed.

4. UV glue is applied on the side of the gap pillar maintaining the gap distance.

A cross section view of the assembled FPI using a UV glue is shown in figure 5.16.

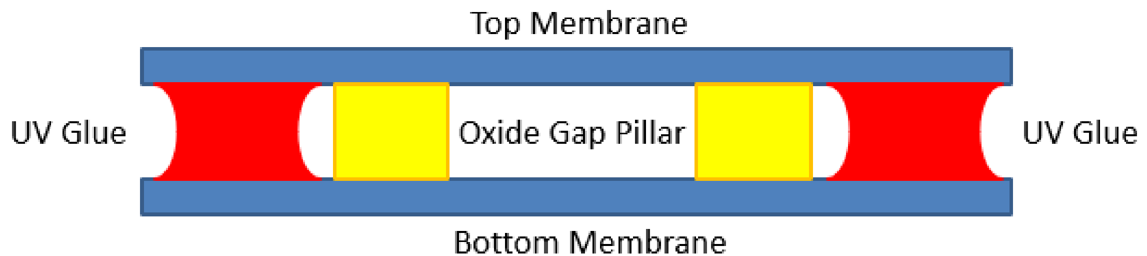

Fig. 5.16 Top and Bottom Membranes assembled with a UV glue. Four oxide pillars define the gap distance and the UV glue puts two membranes together to form the FPI filter.

Pictures of fabricated top and bottom membranes before assembly are given in figure 5.17. The DBR is seen in the middle of the chips. A small aluminum pad deposited at the bottom part of each chip is for wire bond to connect the DC bias for electrostatic actuation. A picture of completed FPI filter is given in figure 5.18 with two wires for electrostatic actuation attached to each membrane. Kapton tape holding the FPI together is also seen on the picture.

a) Top Membrane b) Bottom Membrane

Fig. 5.17 Pictures of finished Top and Bottom Membranes. Deposited DBR is seen in the middle of each chip. Also shown are four silicon dioxide gap pillars around the DBR. Aluminum pad is deposited at the lower side of the chip for wire bonding of bias to electrostatic actuation of the FPI.

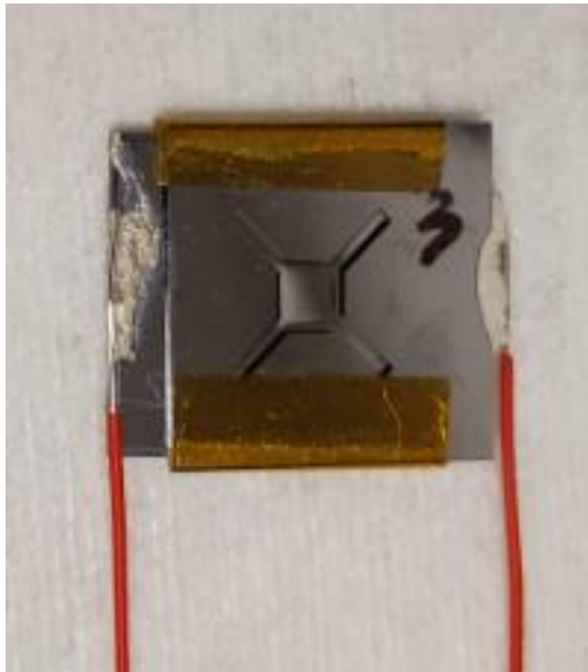

Fig. 5.18 Picture of completed FIP filter. Kapton tape is used to assemble two membranes, and two wires are glued to Al bond pad for electrostatic actuation.

CHAPTER 6. CHARACTERIZATION OF THE FPI FILTER

Three aspects of the FPI filter need to be characterized along the fabrication process. These are the reflectance of the DBR after the deposition step, the deflection of the top membrane through the electrostatic actuation and the transmission spectrum of the assembled FPI filter after the completion of the FPI filter. The theoretical expressions to characterize the DBR and FPI filter, including the electrostatic actuation and the spectroscopic behavior, are described in the chapter 2, and the simulated performance presented in chapter 4. The details of the fabrication process of the DBR and FPI in described in the previous chapter with the result of fabrication. In this chapter, we first describe the equipment used in the characterization, followed by the characteristics of the DBR and the FPI filter from the measurement made after the thin film deposition and the final device assembly, respectively. Simulation results from chapter 4 is reproduced for comparison as well.

6.1 Measurement Equipment used for the Characterization

Two measurement equipment are used to characterize the DBR and the FPI filter; the Fourier Transform InfraRed (FTIR) spectrometer and the optical profilometer. The FTIR spectroscopy is used twice for the measurement of both the reflectance spectrum of the DBR and the transmittance spectrum of the FPI filter. The optical profilometer is used to characterize the deflection of the top membrane from the electrostatic actuation of the FPI filter. Both FTIR spectrometer and optical profilometer are based on the principle of the interference of the light. However, while the optical profilometer uses the interferogram resulting from the interference

directly to measure the vertical features or z-profile of the sample, in the FTIR spectroscopy an additional Fourier transform step is carried out to produce the IR spectrum of the sample. Therefore, we describe the optical profilometer first.

6.1.1 The Optical Profilometer

The optical profilometer [5] is called many different names; an optical surface profiler, 3D optical microscope, or 3D interference microscope. As the name implies, this measurement equipment can measure the height of a sample using interference principle and produce the profile of the surface of sample in Z direction when the sample is placed in X-Y plane. There are other kinds of surface profilers, most notably an Atomic Force Microscope (AFM), where a sensitive cantilever is dragged across the sample surface and produce the surface profile from the movement of the cantilever. With this surface profiling method, the tip at the end of cantilever needs to touch the surface of the sample under measurement. Therefore, this method is not suitable for measuring the profile of a fragile sample surface. Unlike this contact-type surface profiler, optical profilometer utilizes fringe pattern or interferogram produced by interference between two coherent beams of light to measure the height of the sample and uses it to generate the surface profile of the sample. So is yet one more name for the optical profilometer, a non-contact surface profiler.

Interference is well known phenomenon in nature. Contrary to particles, which can only collide upon encountering each other, when waves meet at a point in space they interfere. Depending on the phase difference, the amplitude can be added (constructive interference), completely cancelled (destructive interference), or

partially cancelled. Optical profiler uses the interference to compare the optical path difference (OPD) between a test surface and the reference surface. Inside an optical interference profiler, a light beam is split at the plate beam splitter (BS), reflecting half the beam from a test material, and the other half of the split beam is reflected from the reference mirror. When the distance from the BS to the reference mirror is the same as the distance between the BS and the test surface and the split beams are recombined, constructive and destructive interference occurs in the combined beam depending on the OPD. This creates the light and dark bands known as interference fringes. Since the reference mirror is of a known flatness – that is, it is as close to perfect flatness as possible – the OPD is due to height variances in the test surface. This interference beam is focused into a digital camera, which sees the constructive interference areas as lighter, and the destructive interference areas as darker. In the interference image, called an interferogram, each transition from light to dark fringe represents one-half a wavelength of difference between the reference path and the test path. If the wavelength is known, it is possible to calculate height differences across a surface, in fractions of a wavelength. From these height differences, a 3-dimensional surface map can be generated. Figure 6.1 provides a diagram of the operation of the optical profiler.

To characterize an electrostatic actuation of the X-beam actuation, the Veeco WYKO NT1100 white-light interferometer is used. WYKO NT1000 is an optical profiler, capable of high-resolution 3-dimensional surface measurements using two measuring operation modes: Vertical Shift Interference (VSI) mode and Phase Shift

Interference (PSI) mode. PSI mode is for roughness measurements leveraging optical phase shifting. The VSI mode is a newer technique than PSI developed at Veeco. In the VSI mode, the device measurement is performed with white-light vertical scanning interferometry and the measurement up to a maximum of 1mm topography is possible whereas the PSI mode only allows up to 160nm measurement. Thus, the VSI measurement mode would be used for the X-beam characterization.

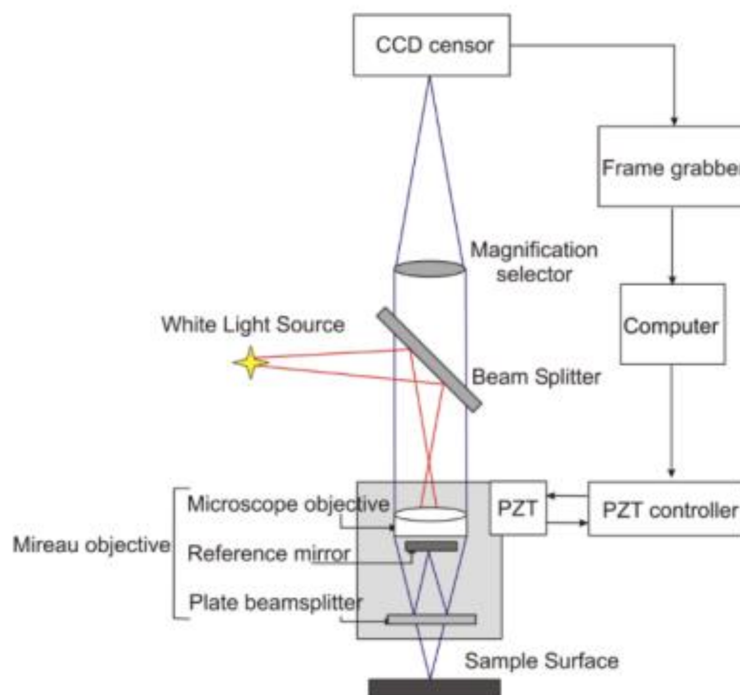

Fig. 6.1 Operational principle of an Optical Profiler. The light splits at the plate beam splitter. A half of the beam is reflected an the sample surface, the other half reflected on the reference mirror. When they combined at the microscope objective, they produce a fringe pattern depending on the optical path difference between two beams. The height of the sample surface can be calculated from the interferogram, a image of light and dark bands resulting from the interference. Figure is taken from [5].

Analogous to the PSI mode, the interferometer beam splitter will reflect half of the incident beam to the reference surface within the interferometer and form

interference fringes as it recombines with the beam reflected from the surface of the test object. However, with VSI mode, the interferometer will filter a white-light beam as it passes through and reflects off the surface of the test object. Instead of measuring the phase of the interference fringes with single wavelength light source (the PSI mode), the white-light source is filtered with a neutral density filter that will preserve the short coherence length of the white light for the device to measure the fringe modulation degree. By adjusting the displacement angle of the test object, dark contrast fringes will occur at the best focus. The surface topology is calculated from the fringe modulation, i.e. the degree of shade in the fringe pattern corresponds to the height of the sample.

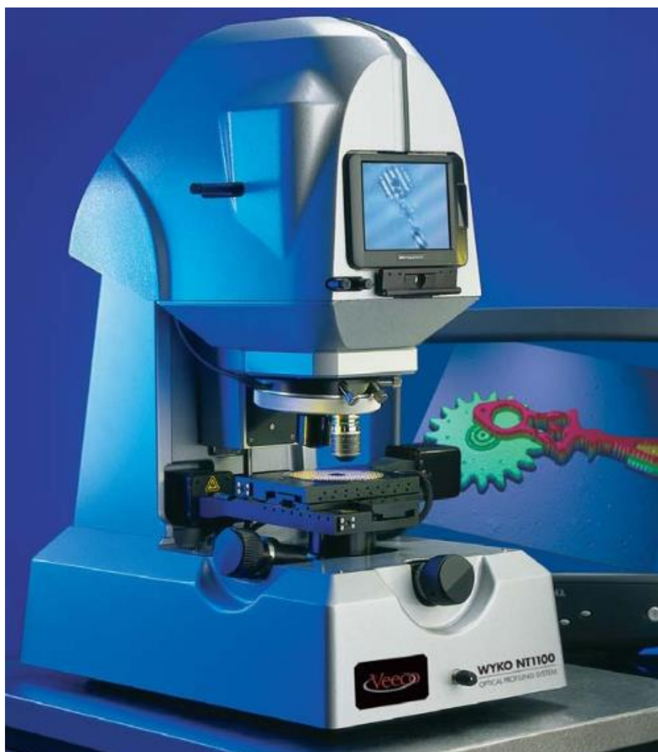

Fig. 6.2 Veeco WYKO NT1100.

6.1.2 The FTIR Spectrometer

An FTIR spectrometer [17] is an instrument which acquires broadband Near InfraRed (NIR) to Far InfraRed (FIR) spectra. FTIR Spectrometers are often simply referred to as FTIR's. To be precise, an FTIR is a method of obtaining infrared spectra by first collecting an interferogram of a sample signal using an interferometer, and then performing a Fourier Transform (FT) on the interferogram to obtain the spectrum. An FTIR spectrometer collects and digitizes the interferogram, performs the FT function, and displays the spectrum.

The operation of an FTIR is typically based on the interferometer setup used in the Michelson-Morley experiment. Figure 6.3 provides with the diagram of the Michelson-Morley interferometer. The interferometer consists of a beam splitter, a fixed mirror, and a mirror that translates back and forth, very precisely. The beam splitter (BS) is made of a special material that transmits half of the light incident on it and reflects the other half. The EM wave from the source strikes the BS and separates into two beams. One beam is transmitted through the BS to the fixed mirror and the second is reflected off the BS to the moving mirror. The fixed and moving mirrors reflect the EM wave back to the BS. Again, a half of this reflected light transmits at and the other half reflected by the BS, resulting in one beam passing to the detector and the second back to the source.

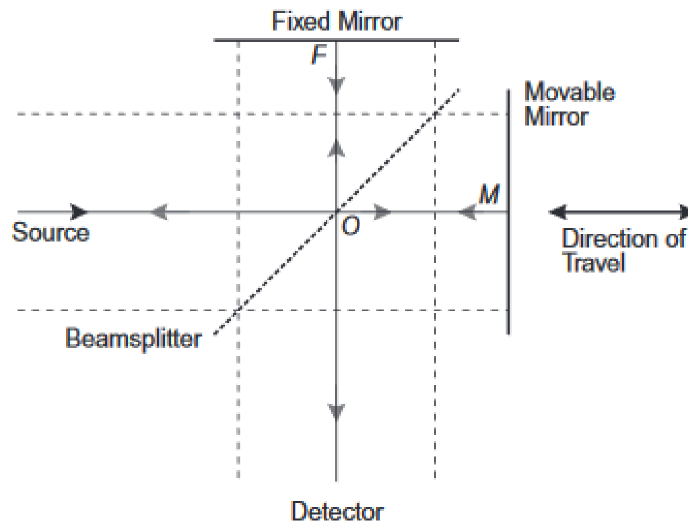

Fig. 6.3. The Michelson-Morley Inteferometer. The interferometer consists of a beam splitter, a fixed mirror, and a mirror that translates back and forth, very precisely.

In the Michelson-Morley interferometer, the Optical Path Difference (OPD) is caused by the difference in distance between the two beams travelling through the two arms of an interferometer. As discussed in chapter 3, the OPD is equal to the product of the physical distance travelled by the moving mirror and n, the index of refraction of the medium filling the interferometer arms. FTIR has a natural reference point when the moving and fixed mirrors are at the same distance from the beam splitter. This condition is called the zero path difference or ZPD. The moving mirror displacement, Δ, is measured from the ZPD. The beam reflected from the moving mirror travels 2Δ further than the beam reflected from the fixed mirror. The relationship between the OPD and Δ is OPD = $2\Delta n$. Interferogram is the name of the signal format acquired by an FTIR spectrometer. It is usually significantly more complex than a single sinusoid, which would be expected if only a single wavelength

of light was present. Figure 6.4 shows the interferogram from a single wavelength source with different OPD.

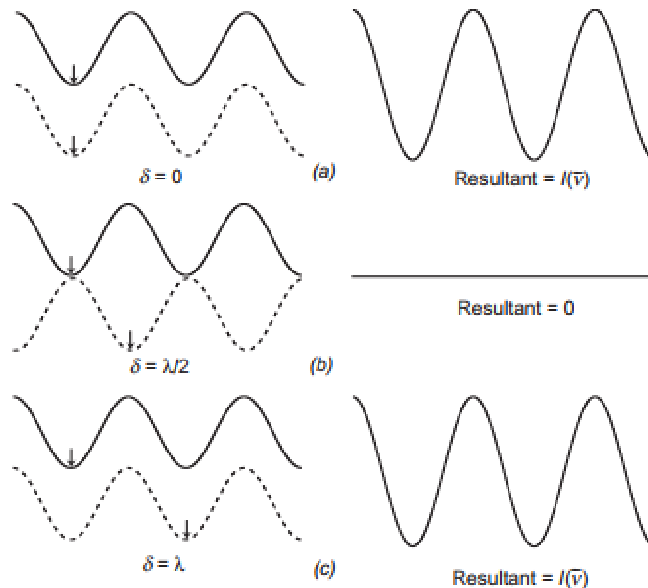

Fig. 6.4 The inteferogram from a monochromatic light source with different OPD's. a) For OPD = 0, two beams interfere constructively. b) With OPD = λ/2, destructive inteference is observed. c) Constructive inteference is recovered when OPD = λ.

Given in figure 6.5 is the interferogram of a broadband light source. The centerburst, the big spike in the center of figure 6.5 is a telltale signature of a broadband source. Its origin lies in the fact that all wavelengths are in-phase at the ZPD. Therefore, their contributions are all at maximum and a very strong signal is produced by the system's detector. As the OPD is increased, different wavelengths produce peak readings at different positions, and for a broadband signal, they never again reach their peaks at the same time. Thus, as we move away from the centerburst, the interferogram becomes a complex oscillatory signal with decreasing amplitude. The X-axis of the interferogram represents the optical path difference.

Each individual spectral component contributes a single sinusoid with a frequency inversely proportional to its wavelength to this signal. This leads us to the definition of the unit of spectral measurement: the wavenumber (cm^{-1}), denoted as n (not to be confused the index of refraction). A wavenumber represents the number of full waves of particular wavelength per cm of length (typically in vacuum, where the index of refraction n = 1). The advantage of defining the spectrum in wavenumbers is that they are directly related to energy levels. A spectral feature at 4,000 cm^{-1} spectral location represents a transition between two molecular levels separated by twice the energy of a transition with spectral signature at 2,000 cm^{-1}.

Fig. 6.5 Typical interferogram of the broadband light source in the region of the centerburst.

Once an interferogram is collected, it needs to be translated into a spectrum (emission, absorption, transmission, etc.). The process of conversion is through the Fast Fourier Transform algorithm. The discovery of this method by J.W. Cooley and J.W. Tukey in 1965, followed by an explosive growth of computational power at

affordable prices, has been the driving force behind widespread adaptation of the FTIR spectroscopy.

Unlike a dispersive instrument, i.e. a grating monochromator or spectrograph, FTIR spectrometers collect all wavelengths simultaneously. This feature is called the Multiplex or Felgett Advantage. When spectra are collected under identical conditions (spectra collected in the same measurement time, at the same resolution, and with the same source, detector, optical throughput, and optical efficiency) on dispersive and FTIR spectrometers, the signal-to-noise ratio of the FTIR spectrum will be greater than that of the dispersive IR spectrum by a factor of $\sqrt{M}$, where $\sqrt{M}$ is the number of resolution elements. Spectral resolution is a measure of how well a spectrometer can distinguish closely spaced spectral features. An FTIR is capable of high resolution because the resolution limit is simply an inverse of the achievable OPD. The FTIR instruments do not require slits (in the traditional sense) to achieve resolution. Therefore, much higher throughput with an FTIR can be achieved than with a dispersive instrument. This is called the Jacquinot Advantage.

Nicolet iS50 FTIR spectrometer made by Thermo Fisher Scientific is used with the FTIR microscope for the FTIR measurement at the Stanford Nano Shared Facilities (SNSF, https://snsf.stanford.edu).

Fig. 6.6 Nicolet iS50 FTIR Spectrometer with the FTIR Microscope

6.2 The Characterization of the DBR

As described in the chapter 2, the most important characteristics that determines the performance of the DBR is its reflectance throughout the spectral range of interest, i.e. λ = 8-11 μm. The reflectance of the DBR improves as the number of deposited stacks increases. The stack consists of two thin films layers with high index contrast. Germanium (Ge: n = 4.00 at λc = 9.264 μm) and zinc sulfide (ZnS: n = 2.21 at λc = 9.264 μm) are used for high and low refractive index materials, respectively. You can find the design details in chapter 3, and the deposition is described in chapter 5. To verify the expectation that more the number of deposited stacks higher the reflectance of the DBR, the reflectance of the DBR is measured after the deposition of each stack until all five stacks are deposited.

Nicolet iS50 FTIR spectrometer is used with the FTIR microscope to measure the reflectance of the DBR mirror. An ambient background is measured first. The reflectance of gold (Au) is measured and used to normalize the reflectance of the DBR's. Greater than 100% reflectance shown in the figure below is an artifact of this

normalization process. The reflectance of the DBR with 1-5 stacks of Ge/ZnS double layers is measured with the FTIR microscope. The result of the reflectance measurement is given in figure 6.7. Figure 4.3, the graph of simulated reflectance of the DBR on 25 um Si membrane is reproduced for a comparison in figure 6.7 as well. As expected in theory and simulation, we observed the improvement of the DBR reflectance as the number of Ge/ZnS stacks increases. Moreover, we observed that in actual deposition, the oscillatory behavior from the 25 μm Si membrane significantly decrease after the fourth stacks, and completely disappeared at the fifth DBR stacks. Therefore, we decide to forego the deposition of the AR layer.

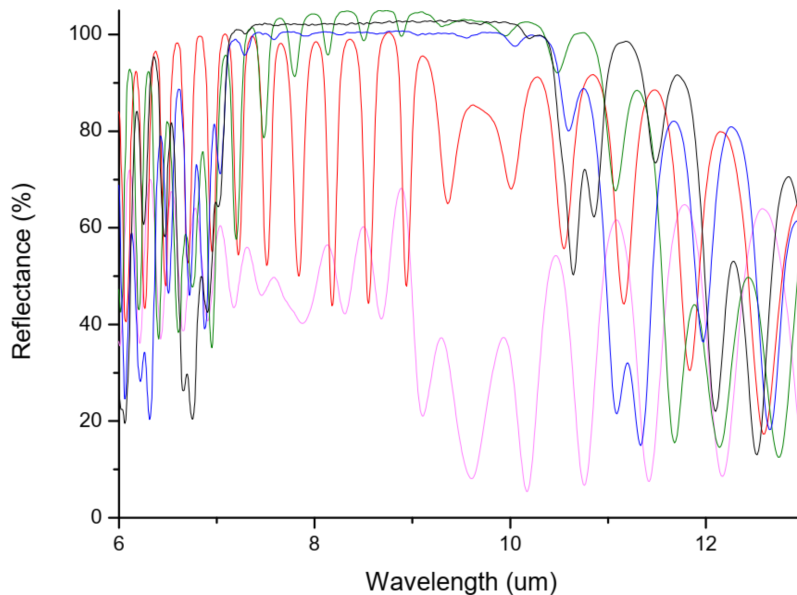

a) Measured reflectance of the DBR with 1-5 Ge/ZnS stacks on the bottom membrane.

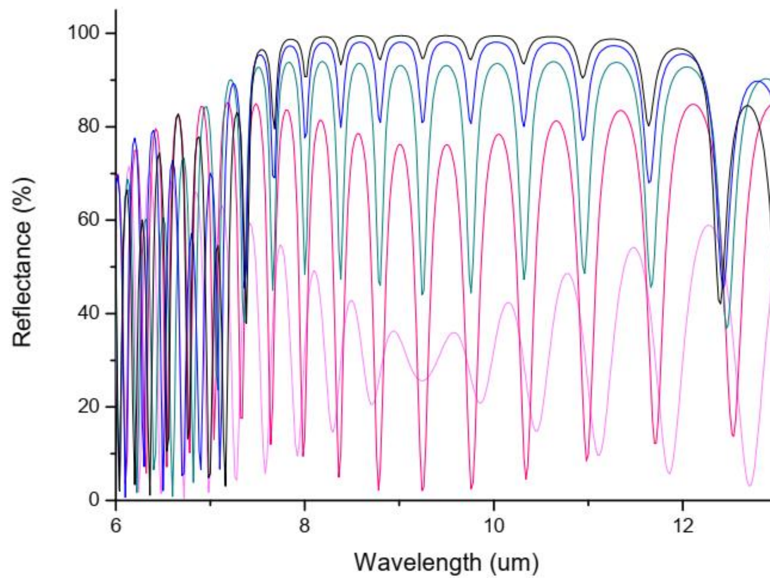

b) Simulated reflectanec of the DBR with 1-5 Ge/ZnS stacks on 25 μm Si membrane.

Fig. 6.7 The reflectance of the DBR mirrors. Pink, red, green, blue, and black graphs are for 1, 2, 3, 4, 5 stack DBR, respectively.

6.3 The Characterization of the FPI filter

To characterize the performance of the FPI filter, we need to associate the gap distance between the top and the bottom DBR's deposited on each membrane with the transmittance spectrum of the FPI filter. As described in chapter 2, the passing wavelength λ of the FPI filter is determined by the gap distance d between two membranes. More precisely, we have $\lambda = 2d$. However, with the measurement equipment available to us, we couldn't concoct the procedure that would directly measure the gap distance while the transmittance spectrum is measured concurrently. Therefore, two separate measurement processes are used to characterize the FPI filter. First, the deflection of the top membrane from the electrostatic actuation is

characterized with the optical profilometer. More specifically, the gap distance between the top and the bottom DBR deposited on each membrane are measured as the bias voltage applied to the FPI filter is varied. Once the gap distance is determined as a function of the bias voltage, we proceed to measure the transmittance spectrum to verify the filtering effect of the assembled FPI filter. This measurement is done while we sweep the bias voltage in the same range as that measured in the previous electrostatic actuation characterization step. Then the performance characteristics, i.e. the tunable filtering effect of the FPI filter, shown through the transmittance spectrum as a function of the applied bias voltage is inferred by combining the results of two previously described measurement processes.

6.3.1 The characterization of the Electrostatic Actuation of the FPI filter

To characterize the deflection of top membrane with applied bias, we first looked for a direct way to measure it, observing the change in the gap distance from the side of the FPI. Because the membranes are located at the middle of the chip, the depth of view is too large to be accommodated with optical microscope. Instead, we decided to use an optical profiler to characterize the electrostatic actuation. As described in section 6.1.1, the optical profiler measures the 3-dimensional surface profile of a sample. Therefore, we devised an indirect way to measure the gap distance with an optical profiler. The top membrane with the X-beam structure has an X-shape through wafer trench from the back side to accommodate the movement of the X-beam as it is actuated with a bias voltage. This X-shape trench is wider than the X-beam, and there are opening around the X-beam that is void of any obstruction.

We decided to use this opening to measure the gap distance. Here is the procedure we concocted: 1. The surface profile of the top side of the FPI filter is obtained with the optical profiler. 2. The height variation of the surface profile is measured along two lines, horizontal and vertical lines that go through the center of the chip. These lines fell on the back of handle wafer of the top membrane, the top surface of device layer of the bottom membrane, the back side of 2 mm x 2 mm optically active area in the middle of the X-beam structure. 3. Knowing that the thickness of the DL of top membrane is 25 µm, the distance between the top and bottom membranes can be obtained by subtracting 25 from the distance between the bottom membrane to the back of the X-beam structure. This procedure is done on all four sides of 2 mm x 2 mm square, and the average of these four values is used as the gap distance.

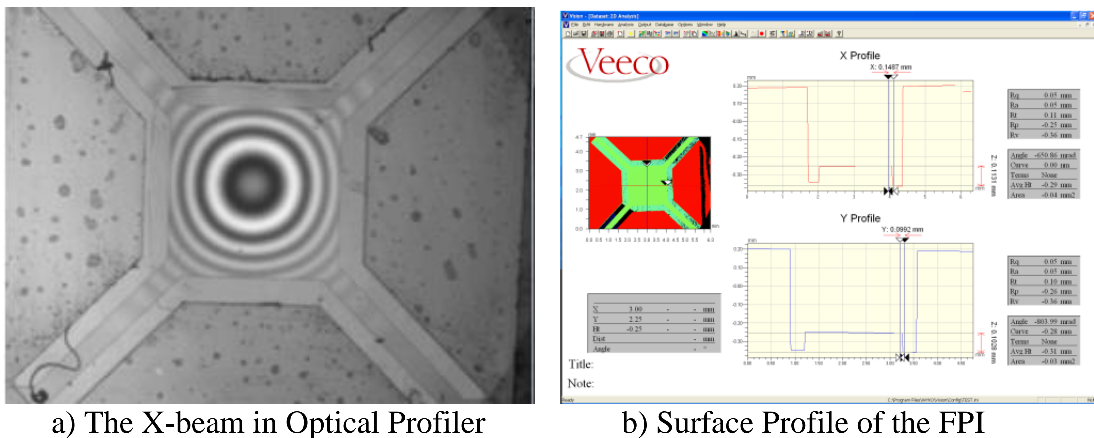

a) The X-beam in Optical Profiler b) Surface Profile of the FPI

Fig. 6.8 The Gap Distance Measurement. The height from the back side of the X-beam and the bottom membrane is measured with the optical profiler. Knowing the membrane thickness of 25 µm, the gap distance can be found by subtracting the membrane thickness from the measured height between the back of the X-beam and the bottom membrane.

Four measurements are made with the same FPI sample. The data are presented in table 6.1 and in figure 6.9, where they are shown with the graph obtained through analytic and numerical solution of the electrostatic actuation (figure 4.10). The missing values from table 6.1 is a result of high voltage breakdown where the wire is glued to the chip with a conducting epoxy. The measured deflections due to the electrostatic actuation are less than both the analytic solution and the numerical simulation of IntelliSuite. This is a result of smaller than originally planned initial gap distance. See next section for detailed explanation. However, even with the smaller initial gap distance, we were able to get the necessary top membrane actuation of 1.5 μm with about 80 V of bias voltage.

Bias Voltage (V)	Run 1 (μm)	Run 2 (μm)	Run 3 (μm)	Run 4 (μm)	Average (μm)	Standard Deviation (μm)
0	0	0	0	0	0	0
10	0.22	0.04	0.07	0.03	0.09	0.09
20	0.42	0.11	0.16	0.11	0.20	0.15
30	0.49	0.19	0.29	0.24	0.31	0.13
40	0.66	0.34	0.53	0.43	0.49	0.14
50	0.87	0.54	0.80	0.68	0.73	0.14
60	1.07	0.77	1.26	0.93	1.01	0.21
70	-	1.07	1.80	1.24	1.37	0.39
80	-	1.41	1.95	1.64	1.67	0.27
90	-	2.15	2.40	2.14	2.23	0.15
100	-	-	-	2.64	2.64	-

Table 6.1 Electrostatic Actuation of the FPI. Missing values are due to electrostatic discharge between the membrane and the conducting epoxy used to glue the wire.

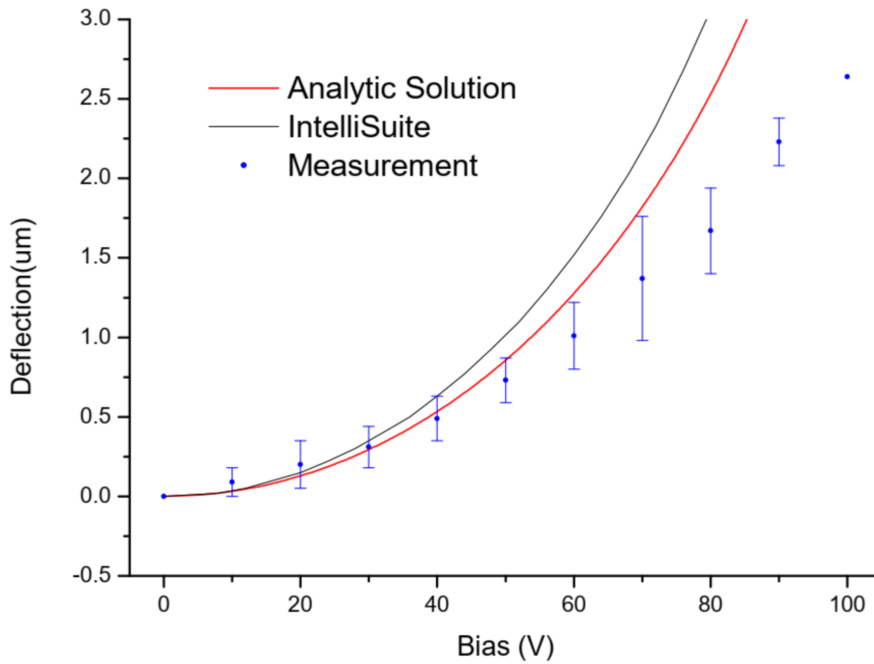

Fig. 6.9 The graph of measured electrostatic actuation of the FPI as a function of applied bias voltage, shown with the graphs from the analytic and numerical solution from chapter 4. Four actuation measurements are performed. Average is used as deflection value, and the SD as errar bar.

6.3.2 The characterization of the Transmittance Spectrum of the FPI filter

Lastly, the transmittance of the FPI filter is measured with Nicolet iS50 FTIR spectrometer with the FTIR microscope. The bias on the FPI filter was varied from 0 to 80 V with an increment of 10 V. The result is given in figure 6.10 for λ = 6-13 μm. Figure 4.12, an expected FPI transmittance is reproduced as figure 6.11 for comparison. A couple of quantitative observation are made. First of all, the tuning of the passing wavelength of the FPI filter was implemented by varying applied bias voltage. The detailed description of the passing wavelength tuning is presented in the next subsection. The erratic oscillatory behavior below 7.5 μm and above 12.5 μm

due to the DBR reflectance degradation outside the mirror bandwidth and the overall oscillatory behavior from 25 μm Si substrate agree quite well between the measurement and the simulation. However, two important discrepancies, that results in the FPI filter performance degradation, were also noticed. First, we observed that the measured transmittance (about 30%) was significantly less than expected value of 100%. The FWHM of measured transmittance spectrum is far greater than expected one (2 μm vs. 0.15 μm). Cause of these degradation as well as means to improve the performance is discussed in the next chapter.

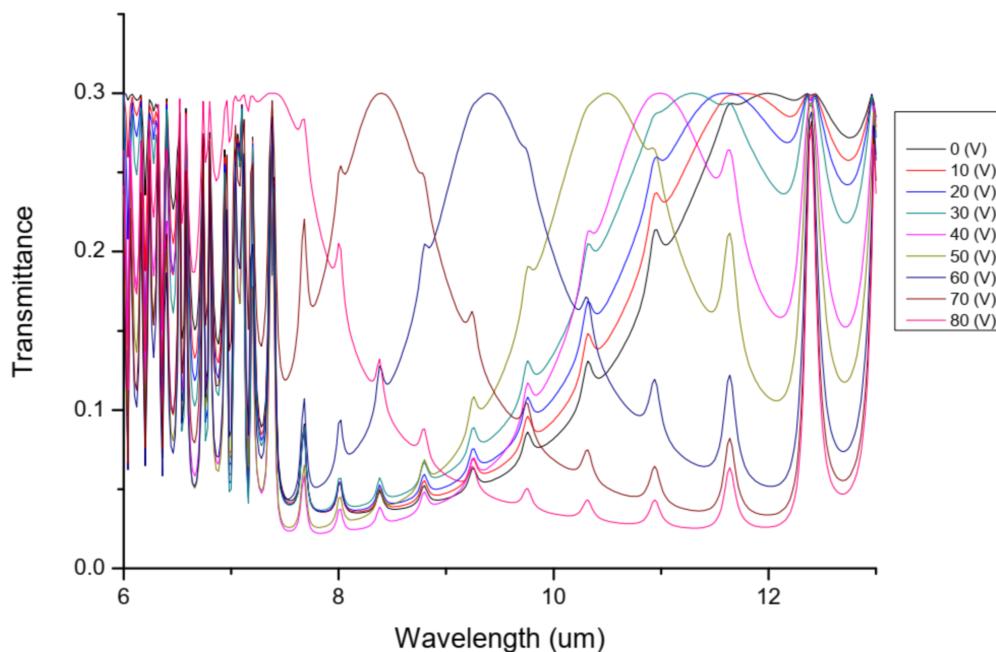

Fig. 6.10 The Transmittance of the FPI Filter for λ = 6-13 μm. The bias voltage is varied from 0 to 80 V in an increment of 10 V.

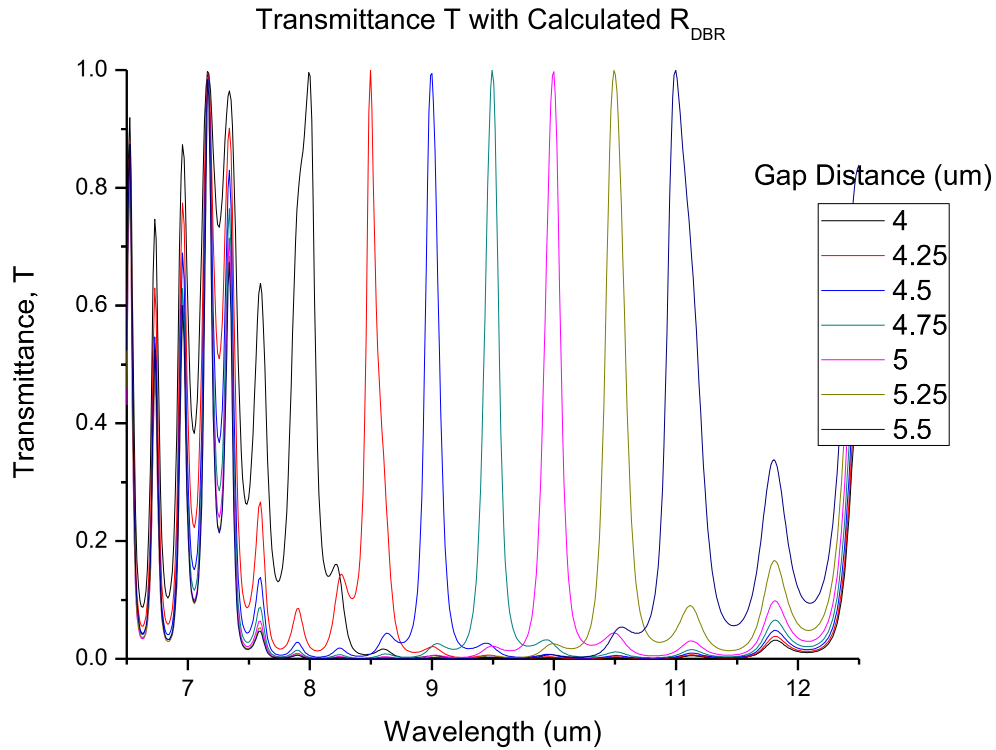

Fig. 6.11 Simulated Transmittance of the FPI Filter for λ = 6.5-12.5 μm. This graph is a reproduction of figure 4.12.

6.3.3 The characterization of the tunable filtering of the FPI filter

A discussion regarding the gap distance is necessary to interpret the measurement result in subsection 6.3.2 correctly. Initial gap distance of 25 μm was assumed in the design, simulation, and fabrication process planning stages to give a room to adjust the gap distance along the way. However, once the DBR deposition was completed, and the thickness of five stacks of Ge/ZnS DBR measured to be 8.135 μm, we needed to tighten the gap distance to improve the electrostatic actuation performance. Longer the actuation distance, higher the bias voltage. Therefore, by tightening the gap distance we can achieve preferred lower bias voltage for the necessary actuation.

In the end, 22 μm thick initial gap pillars are fabricated (8.135 μm top DBR + 8.135 μm bottom DBR + 5.5 μm initial distance between the mirrors = 21.77 μm initial gap distance required). Consequently, with no applied bias, two mirrors are separated 0.23 μm more than the necessary initial gap distance of 5.5 μm. From table 6.1, we found that this distance corresponds to about 25 V of applied bias. Moreover, taking this extra actuation distance into account, we produce table 6.2 to relate the bias voltage and the gap distance. The measurement and the expected passing wavelength agree within 5% most of the time. The measured transmittance for λ = 7-12 μm is given in figure 6.12 to observe detailed actuation behavior of the FPI filter in the required operational spectrum of 8-11 μm.

Bias Voltage (V)	Actuation Distance (μm)	Gap Distance (μm)	Expected Passing Wavelength (μm)	Measured Passing Wavelength (μm)	Error (%)
40	0.49	0.24	10.52	11	4.4
50	0.73	0.48	10.04	10.6	5.3
60	1.01	0.76	9.48	9.5	0.5
70	1.37	1.12	8.76	8.4	4.3

Table 6.2 The expected and measured passing wavelength of the FPI as a function of the applied bias voltage. They agree well within 5% of errors.

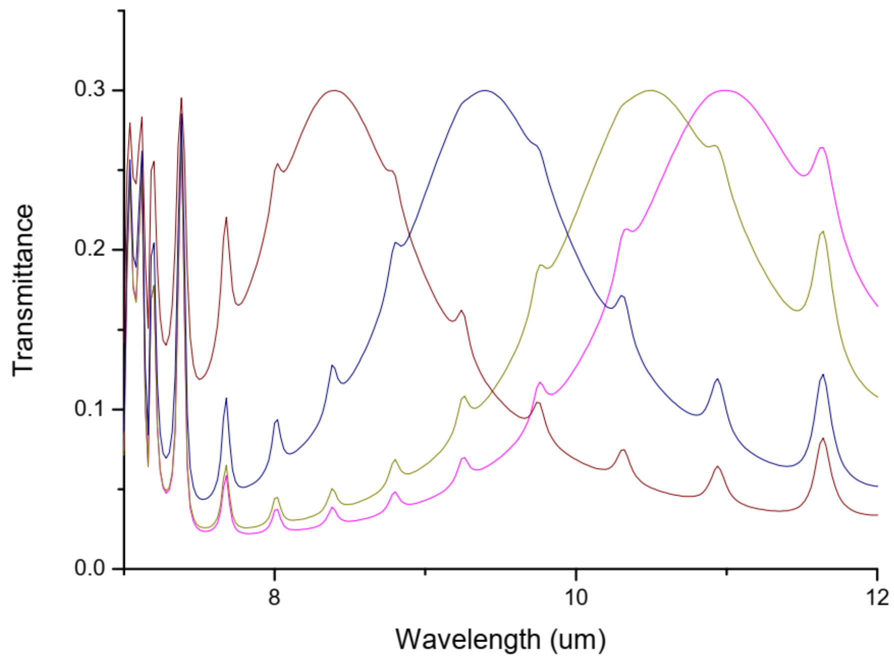

Fig. 6.12 The Transmittance Spectrum of the FPI in λ = 7-12 μm for applied bias voltage from 40 to 70 V in an increment of 10 V. The locations of the transmission peak are 11, 10.6, 9.5, and 8.4 μm for the bias voltage of 40, 50, 60, and 70 V, respectively.

CHAPTER 7. DISCUSSION AND CONCLUSION

7.1 Discussion

The performance of fabricated FPI filter presented in the previous chapter (figure 6.12) provides a proof of principle of our device design and fabrication process flow. However, it also indicates much room for improvement in the device characteristics. Two aspects of the figure 6.12 drew our attention immediately. First is the low transmittance peak at around 30%. Two factors contribute to this low transmittance; the absorption and reflection of incident EM-wave. Even if the DBR with dielectric material layers presents negligible absorption, our device still has two 25 μm, highly doped Si membranes with high free charge concentration. Therefore, we expected some free charge absorption in the Si membrane. With the value of absorption coefficient of $\alpha = 150\ cm^{-1}$ [6, 9, 19] and the Si membrane thickness of 25 μm, we get about 28 % of absorption. Equally significant contribution to the observed loss of transmittance is from the reflection of the incident radiation from the backside of the X-beam structure on top membrane. This is an interface between air and silicon. With the Fresnel equation for reflectance, $R = (\frac{n_1 - n_2}{n_1 + n_2})^2 = (\frac{1-3.42}{1+3.42})^2 = 0.30$. They account for the loss of transmittance within reasonable margin of error. Anti-reflective (AR) coating on the backside of the X-beam structure is proposed to achieve an immediate improvement of the transmittance of the FPI filter by getting rid of the reflection at the air-silicon boundary.

The second performance degradation observed in figure 6.12 is the broadening of the transmission peak. In table 4.1, the expected FWHM of

transmission peak is found to be about 0.2 μm. In the last chapter in figure 6.10, we estimated the measured FWHM to be around 2 μm, an order of magnitude bigger than expected. Atherton [4] identified two attributes that cause the performance degradation of the FPI filter, the plate defects and the effect of finite aperture. He further quantified their effect on the passband broadening as a defect finesse. Since the finesse F is defined as a ratio of the FSR over the FWHM, the broadening of transmission peak results in decrease in the finesse. The effective finesse F_E is approximately given by $\frac{1}{F_E} = \left(\frac{1}{F_R^2} + \frac{1}{F_D^2} + \frac{1}{F_A^2}\right)^{\frac{1}{2}}$, where F_R, F_D, and F_A are for reflection finesse from chapter 2, plate defeat finesse, and finite aperture finesse, respectively. The plate defects can be further divided into three distinct types. The first plate defect type is due to imperfect parallelism. The parallelism defeat finesse $F_{DP} = \frac{\lambda}{\sqrt{3}\delta\mathrm{p}}$ is ascribed if two mirrors deviate from parallel by δp. Spherical deviation δs from bowing of mirror gives rise to the spherical defect finesses F_{DS} defined by $F_{DS} = \frac{\lambda}{2\delta\mathrm{s}}$. Finally, the surface roughness from the micro-defect of mirror coating is the third type of defect that contributes to the defect finesse. Assuming the Gaussian distribution of the surface defects, the surface roughness defect finesse F_{Drms} is given by $F_{Drms} = \frac{\lambda}{4.7\delta\mathrm{rms}}$, with the root-mean-square deviation of the surface defect δrms. Figure 7.1 shows three defect types with their specification parameters. The total defect finesse F_D is given by $\frac{1}{F_D} = \left(\frac{1}{F_{DP}^2} + \frac{1}{F_{DS}^2} + \frac{1}{F_{Drms}^2}\right)^{\frac{1}{2}}$. The aperture finesse F_A is

defined by $F_A = \frac{2\pi}{m\Omega}$, where m is the order of interference, Ω the solid angle of the cone of rays passing through the FPI filter.

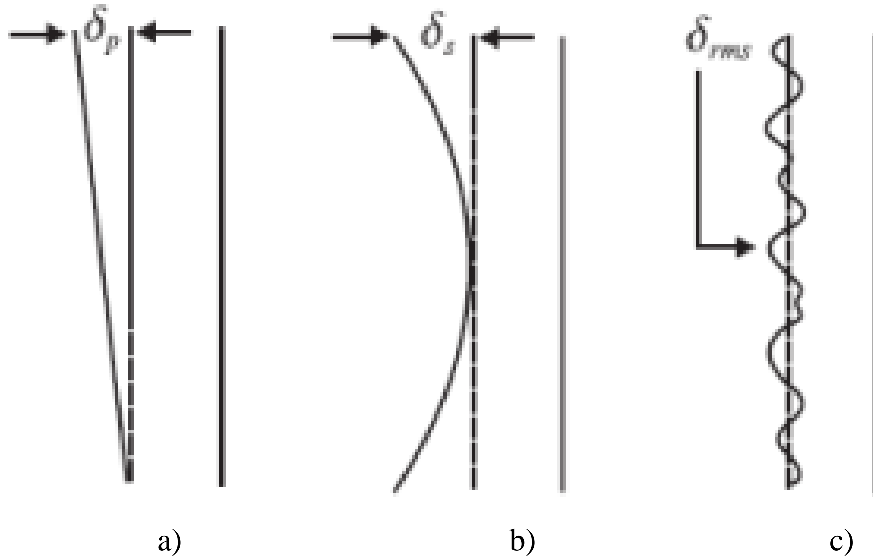

Fig. 7.1 The Plate Defects. a) departure from parallelism, b) spherical bowing, and c) surface roughness from micro-defects.

Our device suffers from all the aforementioned defects as well as the effect from the finite aperture size. The surface roughness cannot be measured with available equipment. Therefore, we estimate the surface roughness with the Innotec nominal uniformity of 5% and the total DBR thickness of 8.135 µm, which gives δrms = 0.41µm. The parallelism deviation of δp = 3.3 µm and the spherical deviation of δs = 2.4 µm are measured with the optical profiler. With these values, the defect finesse is found to be $F_D = 1.2$. The effective finesse F_E from figure 6.12 is about 2.3. It follows that the estimated FWHM of 3.86 µm due to the passband broadening from the plate defect is already greater than the measured FWHM of about 2 µm.

To mitigate the fabrication defects that cause performance degradation, the DBR mirror deposition and the gap pillar deposition process needs to be reviewed. New chip bonding process with better gap control needs to be identified to minimize δp, and consequently the parallelism defect finesse contribution. The spherical deviation from bowing of membrane is due to the stress build-up during the deposition process. This stress is caused by the mirror material thermal expansion coefficient mismatch, and thus unavoidable. However, lowering the E-beam energy used in the deposition can possibly decrease the stress from the thermal expansion by keeping the temperature increase during an evaprant condensation. This, in turn, will lower the spherical defect δs from the bowing of membrane. Using lower E-beam energy during the EBPVD can improve the quality of deposited film, and thus result in lowering the surface roughness defect δrms as well.

7.2 Conclusion

A MEMS-based tunable optical filter is designed, simulated, fabricated and characterized in this dissertation. Fabry-Perot interferometer (FPI) is used as a structural basis for the filter. FPI consists of two partially transmitting mirrors facing each other in parallel. The distance between two mirrors determines the passing wavelength of the filter. More specifically, only the EM waves with wavelength that is integer multiple of twice the mirror gap pass through the FPI (equation 2.1, $d = m\frac{\lambda_m}{2}, m = 1, 2, 3 \ldots$). With the target wavelength range in the long wavelength IR (LWIR) region, from 8 to 11 μm, a distributed Bragg reflector (DBR) with germanium (Ge) and zinc sulfide (ZnS) is used to implement the mirror that covers

the entire spectrum. The DBR consists of stacks of double layers of high and low index materials that are a quarter of wavelength thick each. One of the mirrors is fabricated with four beam springs in an X-shape to tune the passing wavelength of the FPI filter by adjusting the gap distance between two membranes using electrostatic attraction.

Designed device is simulated to confirm it meeting the required device specification. Taking advantage of SOI wafer, the FPI filter is fabricated with simple fabrication process with only four lithography masks, one deposition, and three etch steps. The scaffold structure is fabricated with both surface micromachining and bulk micromachining process. The DBR mirror is deposited using EBPVD on two membranes, and then assembled into the FPI filter. The entire fabrication process is performed at the Stanford Nanofabrication Facility (SNF). Fabricated device is characterized at the UCSC and the SNF. Completed FPI filter demonstrated the necessary filtering and tuning behavior with needs for performance improvement. The cause of performance degradation is identified, and the direction of further study is indicated.

Bibliography

1. Antila, J., Miranto, A., Mäkynen, J., Laamanen, M., Rissanen, A., Blomberg, M., Saari, H., and Malinen, J., "MEMS and piezo actuator-based Fabry-Perot interferometer technologies and applications at VTT," in *Proc. SPIE 7680, Next-Generation Spectroscopic Technologies III*, 76800U 1–12 (2010).
2. Antoszewski, J., Dell, J. M., Shivakumar, T., Martyniuk, M., Winchester, K., Wehner, J., Musca, C. A., and Faraone, L., "Towards MEMS-based infrared tunable microspectrometers," in *Proc. SPIE 4935, Smart Structures, Devices, and Systems*, 148–155 (2002).
3. Antoszewski, J., Winchester, K. J., Nguyen, T., Keating, A. J., Silva, D., Musca, C. A., Dell, J. M., Faraone, L., Silva, K. K. M. B. D., and Musca, C. A., "Materials and processes for MEMS-based infrared microspectrometer integrated on HgCdTe detector," *IEEE Journal of selected topics in quantum electronics* **14** (4), 1031–1041 (2008).
4. Atherton, P. D., Reay, N. K., Ring, J. and Hicks, T. R., "Tunable Fabry-Perot filters", Optical Engineering **20**, 806-814 (1981).
5. Barron, A., Kurganskaya, I., and Luttge, A., *Physical Methods in Chemistry and Nano Science*, Connexions (2009).
6. Bishop, P. J., and Gibson, A. F., "Absorption Coefficient of Germanium at 10.6 μ," *Appl. Opt.* **12**, 2549-2550 (1973).

7. Blomberg, M., Kattelus, H., and Miranto, A., “Electrically tunable surface micromachined Fabry–Perot interferometer for visible light,” *Sensors and Actuators A: Physical* **162**(2), 184–188 (2010).
8. Born, M, and Wolf, E, *Principles of Optics*, Cambridge University Press, 7th ed., (1999).
9. Capron, E, and Brill, O. L., “Absorption Coefficient as a Function of Resistance for Optical Germanium at 10.6 μm,” *Appl. Opt.* **12**, 569-572 (1973)
10. Crocombe, R. A., “Miniature optical spectrometers: There’s plenty of room at the bottom, Part I: Background and mid-infrared spectrometers,” *Spectroscopy* **23**(1), 38–56 (2008).
11. Crocombe, R. A., “Miniature optical spectrometers: Follow the money, Part II: The telecommunications boom,” *Spectroscopy* **23**(2), 56–69 (2008).
12. Crocombe, R. A., “Miniature optical spectrometers, Part III: Conventional and laboratory near-infrared spectrometers,” *Spectroscopy* **35**(5), 40–50 (2008).
13. Crocombe, R. A., “Miniature optical spectrometers: The art of the possible, Part IV: New near-infrared technologies and spectrometers,” *Spectroscopy* **23**(6), 26–37 (2009).
14. Debenham, M. “Refractive indices of zinc sulfide in the 0.405-13-μm wavelength range”, *Appl. Opt.* **23**, 2238-2239 (1984).
15. Dell, J. M., Keating, A. J., Milne, J., Antoszewski, J., Musca, C. A., Faraone, L., Murphy, D., and Samardzic, O., “Micro-electromechanical systems-based

microspectrometers covering wavelengths from 1500nm to 5000nm," in *Proc. SPIE 6765, Next-Generation Spectroscopic Technologies*, 67650L 1–9 (2007).

16. Fabry, C. and Perot, A., "Sur les franges des lames minces argentées et leur application à la mesure de petites épaisseurs d'air," *Ann. Chim. Phys* **12**, 459–501 (1897).
17. Griffiths, P., de Hasseth, J.A., *Fourier Transform Infrared Spectrometry*, Wiley-Blackwell, 2nd ed., (2007).
18. Hecht, E., *Optics*, Addison-Wesley, 4th ed., (2001).
19. Hutchinson, C. J., Lewis, C., Savage, J. A., and Pitt, A., "Surface and bulk absorption in germanium at 10.6 μm," *Appl. Opt.* **21**, 1490-1495 (1982)
20. Li, H. H., "Refractive index of silicon and germanium and its wavelength and temperature derivatives", *J. Phys. Chem. Ref. Data* **9**, 561-658 (1993)
21. Kasap, S. O., *Optoelectronics and Photonics: Principles and Practices*, Pearson, 2nd ed., (2012)
22. Kozak, D. A., Fernandez, B., Morley, M. L., Velicu, S., Kubby, J., "Fabrication and testing of MEMS-based optical filter combined with a HgCdTe detector," *Proc. SPIE 7930, MOEMS and Miniaturized Systems X*, 79300L (2011)
23. Kozak, D. A., Fernandez, B., Velicu, S., Kubby, J., "Prototyping of MWIR MEMS-based optical filter combined with HgCdTe detector," *Proc. SPIE 7594, MOEMS and Miniaturized Systems IX*, 75940W (2010)
24. Keränen, K., Blomberg, M., Tenhunen, J., and Karioja, P., "Analytic and raytrace modeling of a miniaturized infrared spectrometer module," in *Technical*

Proceedings of the 2000 International Conference on Modeling and Simulation of Microsystems, 660–663 (2000).

25. Keränen, K., Karioja, P., Rusanen, O., Tenhunen, J., Blomberg, M., and Lehto, H., "Electrically tunable nir spectrometer," in *Proc. SPIE 3099, Micro-optical Technologies for Measurement, Sensors, and Microsystems II and Optical Fiber Sensor Technologies and Applications*, 181–184 (1997).
26. Klein, C. A., "Room-temperature dispersion equations for cubic zinc sulfide", *Appl. Opt.* **25**, 1873-1875 (1986)
27. Kubby, J. A., *A Guide to Hands-on MEMS Design and Prototyping*, Cambridge University Press, (2011).
28. MacLeod, H. A., *Thin-film Optical Filters*, CRC Press, 4th ed. (2010).
29. Milne, J. S., Dell, J. M., Keating, A. J., and Faraone, L., "Widely tunable MEMS-based Fabry–Perot filter," *Journal of Microelectromechanical Systems* **18**(4), 905–913 (2009).
30. Milne, J., Dell, J., Keating, A., Schuler, L., and Faraone, L., "Widely tunable Fabry-Perot optical filter using fixed-fixed beam actuators," in *2008 IEEE/LEOS International Conference on Optical MEMs and Nanophotonics*] 66–67 (2008).
31. Neumann, N., Heinze, M., Stegbauer, H. J., Hiller, K., and Kurth, S., "Ein mikromechanisches, durchstimmbares Fabry-Perot-Filter für die nichtdispersive Gasanalytik im Spektralbereich 3...5 µm," in *Dresdner Sensor Symposium*, (2003).

32. Neumann, N., Hiller, K., and Kurth, S., "Micromachined mid-infrared tunable Fabry-Perot filter," in *13th Intern. Conf. on Solid-State Sensors, Actuators and Microsystems TRANSDUCERS'05*, 1010–1013 (2005).

33. Neumann, N., Ebermann, M., Kurth, S., and Hiller, K., "Tunable infrared detector with integrated micromachined Fabry-Perot filter," *Journal of Micro/Nanolithography, MEMS and MOEMS* **7**(2), 021004 1–9 (2008).

34. Rebeiz, G. M., *RF MEMS: Theory, Design, and Technology*, Wiley & Sons, (2003).

35. Rissanen, A., Akujärvi, A., Antila, J., Blomberg, M., and Saari, H., "MOEMS miniature spectrometers using tuneable Fabry-Perot interferometers," *Journal of Micro/Nanolithography, MEMS, and MOEMS* **11**(2), 023003–1 (2012).

36. Rissanen, A., Mannila, R., and Antila, J., "Bragg reflectors for large optical aperture MEMS Fabry-Perot interferometers," in *Proc. SPIE 8373, Micro- and Nanotechnology Sensors, Systems, and Applications IV*, 83732R 1–8 (2012).

37. Rissanen, A., Kantojärvi, U., Blomberg, M., Antila, J., and Eränen, S., "Monolithically integrated microspectrometer-on-chip based on tunable visible light MEMS FPI," *Sensors and Actuators A: Physical* **182**, 130–135 (2012).

38. Rissanen, A., Mannila, R., Tuohiniemi, M., Akujärvi, A., and Antila, J., "Tunable MOEMS Fabry-Perot interferometer for miniaturized spectral sensing in near-infrared," in *Proc. SPIE 8977, MOEMS and Miniaturized Systems XIII*, 89770X (2014).

39. Tuohiniemi, M., and Blomberg, M., “Surface-micromachined silicon air-gap Bragg reflector for thermal infrared,” *Journal of Micromechanics and Microengineering* **21**(7), 075014 1–7 (2011).

40. Tuohiniemi, M., Blomberg, M., Akujärvi, A., Antila, J., and Saari, H., “Optical transmission performance of a surface-micromachined Fabry–Pérot interferometer for thermal infrared,” *Journal of Micromechanics and Microengineering* **22**(11), 115004 1–7 (2012).

41. Tuomikoski, S. and Franssila, S., “Free-standing SU-8 microfluidic chips by adhesive bonding and release etching,” *Sensor and Actuators* **A**(120), 408-415 (2005).

42. Yeh, P., *Optical Waves in Layered Media*, Wiley-Interscience, Hoboken, New Jersey, (2005).